2014

Early prediction of fracture in bodies bounded by random rough surfaces

Hector Medina
Virginia Commonwealth University

EARLY PREDICTION OF FRACTURE IN BODIES BOUNDED BY RANDOM ROUGH SURFACES

A Dissertation submitted in partial fulfillment of the requirements for the degree of Doctor of Philosophy at Virginia Commonwealth University.

by

HECTOR EDUARDO MEDINA

Masters of Science in Mechanical and Nuclear Engineering

Virginia Commonwealth University, 2012

Director: Gary Tepper,

Professor and Department's Chair, Department of Mechanical and Nuclear Engineering

Virginia Commonwealth University

Richmond, Virginia

May, 2014

Acknowledgements

First of all, I give thanks to God for His faithful help throughout this work. With my hands lifted up I say: ”God, to You be the glory!”. Additionally, there are numerous persons who have contributed in different ways. First of all, I would like to thank Dr. Karla Mossi for believing in me when I came to the Department of Mechanical and Nuclear Engineering for the first time. Similarly, I thank Dr. Brian Hinderliter for his time invested, advice and long (sometimes heated) discussions. My many discussions with Dr. Gary Tepper served perfectly to refine my work, and to him I am also thankful for his continuous financial support. Undoubtedly, my entire doctoral committee played a key role on polishing my study, in one way or another. Being sometimes extrovert gave me the opportunity to establish fruitful conversations with several other faculty such as Dr. Hooman Trafeshi, Dr. James McLeskey, Dr. Ramana Pidaparti, Dr. Sama Bilbao y Leon, and Dr. Mohamed Gad-el-Hak.

Additionally, I must not overlook the other kind of contribution given by family and friends. Their patience, moral support, company and love were indisputably crucial in my accomplishments. My acknowledgment goes to my daughters Nazareth and Hecdalis, my Mom Victoria, my friends Tom and Shari Roberts, Veronica, Rubi Ho, David Singh, Sharon Wood, and many others.

THANK YOU ALL!

TABLE OF CONTENTS

Chapter Page

LIST OF TABLES

LIST OF FIGURES

Abstract

EARLY PREDICTION OF FRACTURE IN BODIES BOUNDED BY RANDOM ROUGH SURFACES

By Hector Eduardo Medina

A Dissertation submitted in partial fulfillment of the requirements for the degree of Doctor of Philosophy at Virginia Commonwealth University.

Virginia Commonwealth University, 2014.

Director: Gary Tepper,
Professor and Department's Chair, Department of Mechanical and Nuclear Engineering

Under certain loading conditions, surfaces topography coupled with materials degree of brittleness can significantly compromise the mechanical performance of structures. The foregoing remains valid even if roughness is intentionally introduced for engineering reasons. In either case, stress can concentrate. The case of the stress concentration in surfaces having randomly distributed pits is a problem that, although being very practical, yet it remains unsolved. The complexity of a random configuration renders difficult the problem of analytically finding relationships between surface parameters and markers indicative of mechanical failure. Another difficulty is the reproducibility of replicates of specimens possessing random rough surfaces, for destructive testing followed by statistical analysis.
An experimental technique to produce highly controlled replicates of random rough surfaces (including modeling of degradation growth) was developed. This method was used

to experimentally and statistically study the effects on fracture of early randomly degraded surfaces of poly methyl methacrylate (PMMA) versus topographical parameters. Growth of degradation was assumed to go from an engineering surface to one whose heights are normally distributed. (Early stage of degradation is meant to be that level of roughness which is in the neighborhood of the critical flaw size for a given material). Among other findings, it was found that neither stress nor strain alone can be used to predict fracture at this early stage of degradation. However, fracture location was found to be strongly correlated to the ratio of root-mean-square roughness (RMS) to auto correlation length (ACL), above some RMS threshold. This correlation decreases as the material becomes less brittle (i.e., decrease of Young's modulus or increase of percent of elongation). Simultaneously, a boundary-value problem involving traction-free random rough surfaces was solved using a perturbation method, assuming elastic and isotropic conditions. For small RMS/ACL ratio, the solution for the RMS stress concentration factor, k_t^{RMS} was found to be: $k_t^{RMS} = 1 + 2\sqrt{2}(RMS/ACL)$, which agrees very well with the experimental work. Finally, a generalization of stress concentration factor formulas for several geometrical configurations and loading conditions into the *Modified Inglis Formula* was proposed. Finite element analysis was carried out and comparison was made with both experimental and analytical results.

Applications of these results are broad. In surface engineering, for example, our analytical solution can be coupled with Fick's Law to find critical conditions under which a film could become unstable to random roughness. Additionally, in design and maintenance of surfaces in service, it can be used to preliminarily assess how stress concentrates in surfaces where well defined notches can not be used as an approximation.

CHAPTER 1

INTRODUCTION

1.1 Executive Summary

The following are accomplishments of the present work:

i. *Development and realization of a technique* to produce replicates of random rough surfaces at early stage of degradation, including simulation of degradation growth.

ii. *Experimental and statistical study* of the effects on mechanical failure of early randomly degraded specimens of Poly Methyl Methacrylate (PMMA). Correlation between stress, strain and energy at fracture, as well as fracture location density (FLD) was sought versus several topographical parameters. Strong correlation was found between FLD and the ratio RMS/ACL, under quasi-brittle conditions. For less brittle conditions this correlation disappears; and values of Young's modulus and percent of elongation at which this occurs are reported.

iii. *Set up of the boundary-value problem* involving traction-free random rough surfaces using first principles of generalized elasticity for a homogeneous, isotropic material. Using the foregoing setup, *derivation of an analytical solution* of the stress concentration factor in 2-dimensions due to the presence of multiple random pits, via an analytical method that includes a perturbation method, Parseval's theorem, and an energy conservation principle.

iv. Generalization of stress concentration factor formulas for several geometrical configurations and loading conditions, into a proposed *Modified Inglis Formula*(MIF). Table

of parameters are provided.

v. *Finite element analysis* of the aforementioned experimental and analytical studies.

1.2 Overview

Regardless of the considerable advancement on our understanding of material fracture, still structures are over-designed as to assure reliability, thus increasing their cost[1]. It has been reported that a significant portion—as much as one–third—of the cost of fracture and deformation could be eliminated over time through research and development: by acquiring new knowledge of mechanical behavior of materials and applying this knowledge[1]. Also, advancing and changing technology aggregates new challenges to the engineer designer, demanding more efficient use of materials. With the advent of nanotechnology and its distinct governing principles, deeper understanding of the implications of surface roughness is needed. Furthermore, with the repeating finding that introduced roughness produces positive engineering outcomes in various surface systems, the engineer is faced with the question: "How much can this introduced roughness compromise structural integrity?

With just a few exceptions, in the field of fracture mechanics most of the research has been advanced since after World War II, as a consequence of the catastrophic failures of the Liberty ships [2]. Although a significant amount of work has been accomplished to understand deformation and fracture due to discontinuities on materials, yet most of it involves well-defined geometrical holes and notches[3]. However, many natural degrading processes generate surface roughness characterized by having irregular shapes. For example, natural weathering of structural materials in service nearly always generate random roughness conditions on surfaces. Similarly, roughness is often intentionally introduced on surfaces for engineering reasons. There remains the need, therefore, to further understand brittle and ductile failure of materials possessing surfaces with degradation that more

closely emulate what occurs in realistic service conditions.

1.3 Economic Motivation

A single scratch on a new article—e.g., paint of an automobile, or the screen of an expensive smartphone—often causes depreciation in its final financial value that is much greater than the cost of the real mechanical damage. Even though from the consumer's point of view, priority is commonly given to the subjective worth of surface material degradation, one of the duties of the engineer is to characterize the mechanical implications of the problem, to the point of providing predicting models of failure and to help to increase lifetime of materials in service. Scribe is an intentional scratch through the coating for testing; but for coatings in service, fracture (surface cracking, channeling, delamination, or spalling) can occur due to weathering combined with high stresses, or cyclic strain as occurs on bridges, for example. Unfortunately, at times, the implications of surface degradation surpass mere aesthetic and lead to mechanical failures that could involve both human life and material loss.

Despite the fact that catastrophic failure offers profits to attorneys and consulting engineers, such events are damaging to the economy as a whole. Undoubtedly, the economic cost of fracture and its prevention is quite large[1, 4]. One important aspect that increases the costs is that related with overdesign of structures, as to assure reliability [5]. A study by the Department of Commerce completed in past years showed that the annual cost of fracture (not including the effects of wear or corrosion) of materials in the United States represented about 4% of the Gross National Product (GNP), which infers a rather significant use of resources and manpower[4]. According to similar studies, if wear and corrosion effects were added to that noteworthy figure, costs would elevate to about 10% of the GNP [1]. Europe has reported comparable percentages [6]. Therefore, it is quite reasonable to assume that similar to higher values are likely to apply to all developed countries [1], and

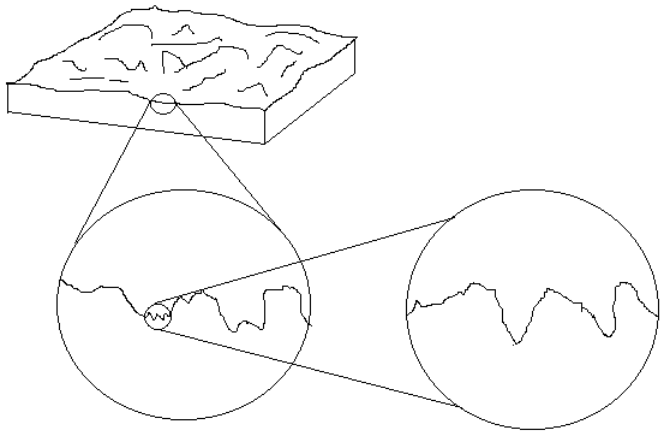

Fig. 1. At some scale all solid surfaces are rough.

perhaps strictly higher in underdeveloped regions.

1.4 Roughness on Surfaces

Roughness is one of the main factors that influence wear and crack initiation and propagation [7]. Under some proper loading, valleys of rough surfaces can be thought of as surface–crack initiators [8]. By surface, it is meant the geometrical boundary between a solid and the environment. Now, random roughness has been defined as the standard error of individual elevations after oriented roughness has been removed [9]. Or analogically stated, random roughness can be described as the standard deviation of elevation from a plane across a tilled surface, once oriented roughness is accounted for. The influence of random roughness on surfaces is very important as it is a phenomenon that continuously takes place in nature and on engineering surfaces [10]. It can reasonably be stated that ultimately, under some fine-scale spatial resolution, random roughness is present almost everywhere [11, 12], see figure 1. For instance, textures of most engineering surfaces, which are a function of both its production process and the nature of the parent material, are random [13]. Almost any known natural phenomenon can cause materials degradation.

The synergistic effects of the accumulation of all these degrading phenomena cause random roughness on surfaces of materials in service. It is, therefore, of much engineering interest to clearly assess the effects of random roughness on mechanical material failure in order to increase our level of predictability.

1.5 Impact on Performance of Surface Degradation and Roughness

Surface degradation can be characterized in terms of reduction in the level of performance of an engineering system[14]. All structures in service at power plants, solar cells, energy-harvesting micro electromechanical devices, lithium-ion anodes, turbine blades, are but a few of a long list of exposed configurations whose outer surfaces can degrade and hence hinder their functionality. For any of these items, there is a critical minimum level of performance. Degradation proceeds at a rate that varies with local conditions and parent material, and failure occurs if performance declines to below its critical level; alternatively, decrease in efficiency occurs if performance decreases but remains above the critical level. For instance, according to an IAEA 2009 report [15], as of year 2008, 327 (out of 439) nuclear power plants had been in operation for 20 years or more. Consequently, the issues of plant life management and license extension are receiving increasing emphasis in many countries. Pipe corrosion, containment (and other concrete-made structures) weathering and wearing, coatings degradation, reactor vessel embrittlement are some of the processes that required deeper understanding to ensure continued efficient and safe operation of the power plants.

Another important example of negative impact on performance due to surface degradation is in the area of heteroepitaxial structures with semiconductor films[16, 17]. The problem arises from the fact that high stresses—in the order of 10 GPa—can be induced due to lattice mismatch during film growth. Besides the direct negative effect on electronic or optoelectronic performance by the devices, these residual loads can induce further surface

evolution in a non-equilibrium manner. The progress of this mechanism can, in turn, lead to mechanical failure of the structure. Even if the evolution of the surface comes to an equilibrium, it is left roughened. This geometrical condition coupled with the aforementioned high residual stresses can lead to fracture of this brittle structures.

1.6 Applications

Early predictions of mechanical failure on surfaces that roughen randomly will be beneficial to several fields including energy and power[18], implant research[19, 20], micro/nanoelectromechanics [21–23], coatings [24–26], mineralogy[27, 28], etc. Recently, it has been reported that induced roughness on silicon-based solar cells increase light absorption, thus increasing the efficiency of the cells[29]. However, this provoked roughness also introduces mechanical weakness into the overall system which must be accounted for during design. In the field of dentistry, it has been strongly emphasized the effects that surface roughness has on the lifetime of dental implants [19, 20]. For example, from the dental laboratory perspective, one of the four most common causes of fractures in implant-supported removable dentures is roughness and wear of the posterior teeth to the point of loss of vertical dimension of occlusion resulting in anterior teeth fracture/debonding[20]. On the other hand, in the biomedical field, there is strong evidence that there is a positive correlation between surface roughness and bone-to-implant contact (see figure 2): within certain micro-roughness range, the higher the roughness the higher the contact [30]; this implies that osseointegration is expedited by the introduction of surface micro-roughness in the interface. Again, this benefit of roughness competes with the mechanical strength of the implant material, a dilemma that must be investigated and further understood for a random rough situation.

Much study has been done trying to characterize and predict the influence of roughness on micro/nano electromechanical devices. For example, the influence of random roughness on cantilever sensitivity and resonance frequency has recently been studied [21, 22] and

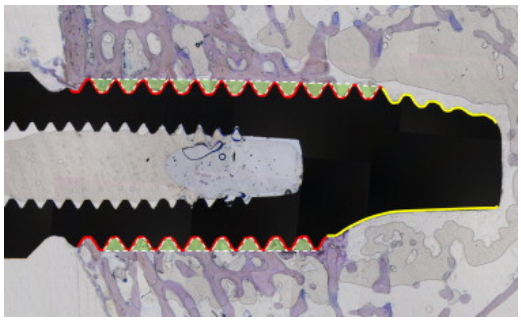

Fig. 2. Roughness of bone-to-implant contact is strongly and positively correlated to bone healing (within some range of roughness).

cantilever bending with rough surfaces was previously well studied by Jorg Weissmuller et al., who concluded that roughness has a non-negligible effect on the cantilever sensitivity[23]. This piece of knowledge has important implications in biosensor design and use.

Another application involves the prediction of lifetime of protective coatings. Failure of coating films (figure 3) takes place after the loss in barrier integrity due to the accumulated damage of small scale weather-induced degrading events. These events imprint random rough damage on the coating surface, which under some type of loading, could lead to chain scission and then probably to coating fracture [2]. A hefty number of investors have obvious interest in predicting the service life of polymeric products exposed to the environment, as these represent, for example, the protective coatings of many structures in service [31]. It has been found that cracks in the coating of gas turbine blades act as an initiator for the thermal fatigue crack in base metal[32]. Economical and safety reasons are among the most important benefits to gain from more accurate service life predictions of coatings [31]. These needs are more extensively expressed in a symposium entitled Service Life Prediction [33], which for the sake of conciseness of the present document, have been left to the choice of the reader.

Additionally, there are many other fields that could benefit from the present study such as: tribology, forensic sciences, surface engineering, etc.

Fig. 3. Failure of coating films can lead to subsequent failure of structures

CHAPTER 2

FROM A SINGLE NOTCH TO RANDOMLY DEGRADED SURFACES: LITERATURE REVIEW

2.1 Historical Background

One hundred years ago, on March 14, it was read at the Spring Meetings of the 54th Session of the Institution of Naval Architects, a work which would become one the first[1] quantitative evidence for the stress concentration effect of flaws[36]. Moved by a recommendation made in 1910 by B. Hopkinson [37], C.E. Inglis derived and delivered the results of his analysis of elliptical holes in flat plates, which later Griffith used as the basis to develop his now famous crack-criterion [38]. Consider a large flat plate with an elliptical hole having major axis a and minor axis b, Fig. 4a; assumed that is loaded with a remote normal stress σ_{remote}, sufficiently far—so that Saint Vernant's principle applies[39]—from the hole. Furthermore, the load is applied perpendicular to the major axis, Inglis found that the local stress at either extremes of the hole along the major axis is magnified by a factor of $(1 + \frac{2a}{b})$, and thus the stress concentration factor, SCF, is given by:

$$SCF_{Inglis} = \frac{\sigma_{extremes}}{\sigma_{remote}} = (1 + \frac{2a}{b}) \tag{2.1}$$

This mathematical result was coupled with the so called soap-film method of stress estimation developed by both Griffith and G.I. Taylor, and the First Law of Thermodynamics, to find a solution for the remote stress at failure of an elastic flat plate possessing a crack [38]. Thus, the most important difference between the two results was that while the King's

[1] Neuber explicitly states[34] that Kolosov had developed a similar work and reported it four years earlier[35] in a paper written in Russian.

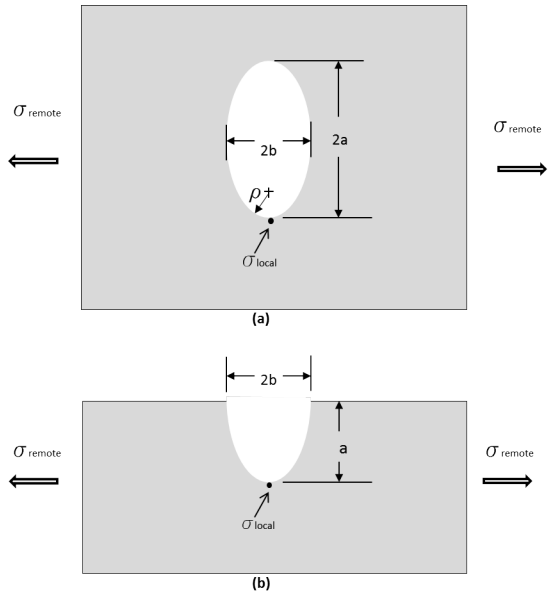

Fig. 4. (a) Elliptical hole in a infinite elastic thin plate. (b) Semi-elliptical notch in a semi-infinite elastic thin plate. In both cases, remote load is applied perpendicular to major axis and at location very far from the discontinuity.

College lecturer applied his to the concentration of stress due to a hole—or notch—Griffith directed his research to cracks. Unfortunately, although Griffith's result was successfully applied to brittle specimens, yet it failed to predict fracture of metals.

For the next 28 years, regrettably, engineers and scientists seemed to have lost interest to understand the reasons behind the discrepancies between metallic fracture behaviour and Griffith's model. Those, almost, three decades of indifference towards research on the fracture problem were interrupted, in Washington, D.C., by the fracture mechanics research team led by G.R. Irwin at the Naval Research Laboratory who were motivated, most likely, by the catastrophic failure of the Liberty ships—which the United States was supplying to Great Britain under the Lend-Lease Act during World War II [2]. Irwin's major contribution to fracture mechanics was the extension of Griffith's model for brittle materials to apply to ductile materials, where plasticity reduces the impact of surface features that

might lead to fracture[40].

After the reawakening of fracture mechanics, research was directed in two main areas: one focusing on crack analysis and the other, on design of structural members. For the former, the principal parameter—although not the only one—studied has been the stress intensity factor (SIF), while for the latter, the stress concentration factor (SCF).

Rendering Caesar what is Caesar's, if Griffith can be called the father of crack analysis, Inglis should be called the father[2] of the SCF. Furthermore, what makes the later–knighted civil engineer's result more significant is that it both preceded and served as basis to that of Alan A. Griffith. Granted, the latter has directly impacted more fracture mechanics research than the former,as it is obvious by the far larger number of citations[38]. However, as it will be shown on this chapter, Inglis' result is powerful enough to serve as a good estimate for multiple cases ranging from non-elliptical single-notch, multiple periodic notches, sinusoidal continuous surfaces, and even (as it will be shown in a later chapter) randomly roughened surfaces—with proper restrictions in the type of loading and other conditions which will be mentioned.

2.2 Single Notch

Inglis's result (2.1) of the SCF due to a single hole on a plate can be applied directly to the case of a single notch[3] possessing a configuration of a half ellipse, see Fig. 4b. Another version of (2.1) is that involving the radius of curvature (ρ) at the tip of the notch; so that equation (2.1) can be written as:

$$SCF_{Inglis} = \frac{\sigma_{extremes}}{\sigma_{remote}} = (1 + 2\sqrt{\frac{a}{\rho}}) \tag{2.2}$$

[2]Or, at least he should be called one of the fathers of the SCF, to give credit to Neuber's account of the facts

[3]Provided that the notch is shallow. Otherwise, a factor of 1.12 must be introduced into the equation

Equations (2.1) and (2.2) could be used interchangeably. After (2.1) was reported, a smorgasbord of single-notch cases have been studied[3, 34, 41] depending on type of loading (e.g.,tensile, compression, torsion, bending, etc.) and geometric configuration (e.g.,hyperbolic, v-notch, half-circle, rectangular, etc). Although, some solutions for the single-notch case will be briefly considered in the next subsection, however, in this document our goal is not to simply re-provide those solutions, as they can be found in the references to be indicated. At this point our goal is to understand the operational envelopes or limitations of those solutions. As it will be shown in the next subsections, some adjustments to those single-notch solutions of the SCF must be considered in order to compensate for heterogeneity of material, 3-dimensional conditions, Poisson's ratio and plasticity effects.

2.2.1 Other Geometries

Besides the semi-elliptical and semi-circular notches for which either equation (2.1) or (2.2) apply, there are analytical and/or empirical solutions for geometries such as v-notch, rectangular, parabolic, hyperbolic, and so forth[3, 41]. Perhaps Peterson [3] was the first to compile a comprehensive set of results of SCF's for different configurations. Hardy and Malik [41] reported a survey for a collection of solutions since after Peterson's work and until 1992. More recently, Noda and Takase [42, 43]derived and proposed consolidated formula for both flat specimen and round bar useful for all notch shape. They reported that their formula gave errors of only 1% or less in the SCFs for any shape of notch. However, the formula given are very lengthy, which does not serve the purpose of simplification needed in preliminary designs or to couple with more involved ordinary differential equations (such as the Navier-Stokes in fluid dynamics). For example, for the case of a round

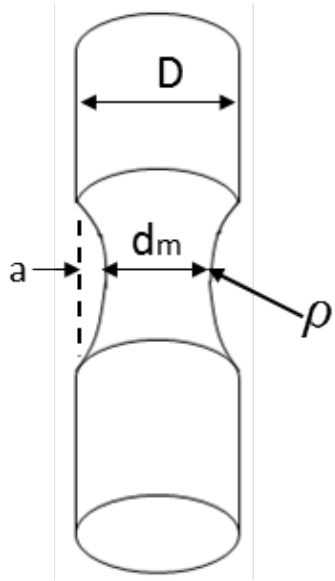

Fig. 5. Round-notched bar.

bar under tension, Fig. 5, the consolidated formula suggested by Noda and Takase[42] is:

$$\begin{aligned}\frac{K_t}{K_{tN}^{m=2.8}} = (&1.0001 + 0.0036g - 0.0065g^2 + 0.0021g^3 \\ &+(0.0116 + 1.404g - 1.28g^2 + 0.1799g^3)\theta \\ &+(-0.1311 - 8.165g + 9.687g^2 - 2.124g^3)\theta^2 \\ &+(0.4240 + 16.94g - 22.77g^2 + 5.618g^3)\theta^3 \\ &+(-0.5156 - 15.07g + 21.7g^2 - 5.57g^3)\theta^4 \\ &+(0.2112 + 4.890g - 7.332g^2 + 1.896g^3)\theta^5\end{aligned} \tag{2.3a}$$

Where $\theta = \frac{2a}{D}$= relative notch depth; and the other quantities are as follows:

$$K_{tN}^{m=2.8} = \frac{(K_{ts} - 1)(K_{td} - 1)}{((K_{ts} - 1)^{2.8} + (K_{td} - 1)^{2.8})^{\frac{1}{2.8}}} + 1 \tag{2.3b}$$

$$K_{ts} = SCF_{Inglis}(1.000 - 0.127\psi + 0.2908\psi^2 - 0.1420\psi^3) \quad (if 0 \leq \psi \leq 1.0) \tag{2.3c}$$

$$K_{ts} = SCF_{Inglis}(1.148 - 0.160\eta - 0.0345\eta^2 + 0.0693\eta^3) \quad (if 0 \leq \eta \leq 1.0) \tag{2.3d}$$

$$\psi = \sqrt{\frac{a}{\rho}}, \quad \eta = \frac{1}{\psi} \tag{2.3e}$$

$$K_{td} = SCF_{tH}(1.0011 - 0.025485g + 0.00613g^2 + 0.00613g^3) \tag{2.3f}$$

$$g = \begin{cases} \frac{d_m}{2\rho}, & \text{when } \frac{d_m}{2\rho} < 1.0 \\ 2 - \frac{2\rho}{d_m}, & \text{when } \frac{2\rho}{d_m} < 1.0 \end{cases} \tag{2.3g}$$

$$SCF_{tH} = \frac{1}{N}[(g_0(\sqrt{g_0 + 1} + 1) + (0.5 + \nu)g_0 + (1 + \nu)(\sqrt{g_0 + 1} + 1)], \quad N = g_0 + 2\nu\sqrt{g_0 + 1} + 2, \quad g_0 = \frac{d_m}{2\rho} \tag{2.3h}$$

Besides being extensive,another limitation is that some of these formula are material-dependent[4]—for example Noda and Takase [42] reported to have used a Poisson's ratio (ν)

[4]As they should be if they are to be applied for conditions other than plane-stress

of 0.3 in their derivation of the SCF formula for single notch and flat specimens. Thus, the equations reported in [42], for instance, need to be derived for each material's ν. On the other hand, Inglis' result, although simple, can only be applied to a limited number of single geometries with minor errors, such as U-notch [3]. However, for some shallow notches, it can provide reliable approximations as well. Furthermore, for periodic and even continuous surfaces it proves to be reasonably accurate to a first-order, as it will be discussed later.

2.2.2 3-Dimensional Conditions

Initially, most of the equations obtained for SCF's were developed assuming either plane-stress or plane-strain conditions. In reality, these assumptions only can reliably and validly estimate the SCF for cases with either very small or very large thickness, but not in-between. Consider a finite thickness large plate that contains a hole; the plate is subject to a normal load in the direction indicated (see Fig.6a). Depending on the length of the hole, it

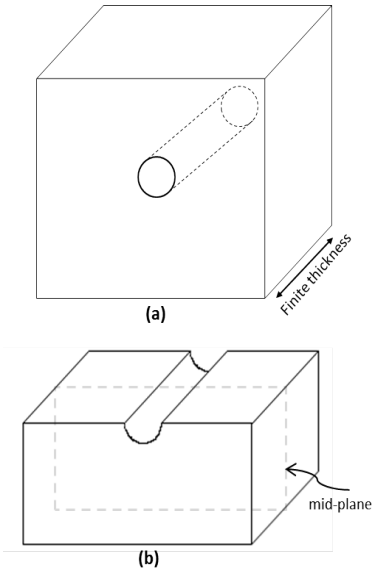

Fig. 6. Top: hole through a solid block; bottom: groove on a solid block

has been shown via finite element method[44] that the maximum stress concentration factor

can be located at a plane near the lateral surfaces at the ends of the holes, as opposed to the mid-plane. Extending the same idea to a 3-D groove configuration like the one shown in Fig. 6b, it is interpreted that there is a critical groove's length above which the SCF is not longer located at the midpoint—as it would be the case for either plane-stress or plane-strain conditions. In [44] it was reported that the maximum SCF was located at a plane located $\frac{1}{8}$ of the thickness away from the surface; and that it was slightly higher (1%) to that of the mid-plane, for a specimen's thickness that was 4 times the size of the hole (or notch), and a Poisson's ratio of 0.3. This number would seem to increase for higher Poisson's ratio. Therefore, when dealing with finite thickness notched specimens, one must consider the maximum SCF at a location nearer to the lateral surfaces perpendicular to the axis of the notch (groove) than to the mid-plane. This is particularly important, for example, when cutting out small lamillaes from mono-crystal Silicon substrate to produce specimens for Scanning-Electron Microscopy (SEM) testing[45]. Since stress could concentrate the most at a location close to the surface (depending on the thickness of the specimen), engraving of lamellaes should be started at some line in the mid-plane to avoid silicon substrate to chip off.

2.2.3 Poisson's Ratio Effect

The effect of Poisson's ratio on the SCF has been studied [44, 46–48]. It is known that for plane-stress of an elastic solid, the SCF is independent of the Posisson's ratio(ν)[3, 34, 44, 46–48]; On the other hand, for plane-strain it does depend on it. For a finite thickness, the dependence on ν varies according to the thickness of the specimen until it reaches a plateau, in a sigmoidal manner. Contrary to this knowledge, most design calculations rely on SCF values that were originally obtained from photoelastic experiments [3, 49–51]. The effect of Poisson's ratio on the SCF is due to the fact that material in the third dimension constrains the displacement of material in the other two dimensions. For isotropic, homo-

geneous and elastic conditions, Grant et al [46] reported that the 3-D SCF is affected by Poisson's ratio under tensile and bending loading but not when subjected to torsional stress. One could expect, however, that even under torsional loading, Poisson's ratio could have an effect on the SCF if the material is non-homogeneous, a hypothesis which yet need further investigation.

2.2.4 Plasticity Effects

Plasticity deformation can radically decrease notch-sensitivity[3, 36, 38, 52, 53]. Consequently the degree of brittleness should be accounted for in the formulations of stress concentration factors. Load-carrying capacity could be underestimated if the SCF does not consider, for example, percentage of elongation of the material in question. One could think of plastic flow as an "eraser" of surface irregularities, where the higher the potential for plastic flow there is the greater its "erasing" capabilities are. Thus, a relatively small notch in a brittle material could have the same load-reducing capacity effects as a large notch in a ductile material. This infers that a characteristic effective notch size dependent not only on the actual notch size but also on the ductility of the material is needed to properly characterize notch-sensitivity.

In order to model the aforementioned mechanisms, an approach that renders localized ductility as nonlinear springs has been reported and used in different applications[54–59]. Based on Cotrell's model, Suo et al [59] proposed a way to simulate the brittle-to-ductile transition at the root of a notch. Although the model was applied to composites, the idea is applicable to other materials like metals in the sense that elasticity-plasticity dual phenomena take place at the micro level, where grains and grain boundaries or different phases possess dual properties.

2.2.5 Heterogeneity

Homogeneous-material assumption serves well to a certain scale in metals and alloys, with regards to fracture mechanics and strength of materials analysis. However, at smaller scales—but still under solid continuum assumption—homogeneity conditions tend to model less validly the behavior of most engineering materials. This fact is particularly crucial when trying to utilize results of SCF that were developed at the macro level on applications at smaller scales.

In a study that involved the experimental utilization of paper as a fiber composite, Balankin et al [60] investigated the long-range density correlations on the stress concentration, among other aspects. In a rapid communication [60], they reported that the increase in SCF due to a small disorder at the notch tip is simply the result of adding a geometrical defect to the notch depth. This geometrical perturbation approach assumes fractal behavior on the heterogeneity of the material. However, in metals, grain boundaries do not necessarily appear in that type of pattern. More study, therefore, needs to be carried out in this regards. The stress concentration in composites, however, have been readily studied for over half a century [61–69]. Perhaps, Hedgepeth's work [61, 62] has been among the most influential studies on this area. First, he presented and solved for the SCF of a 2-D composite system under elastic behavior [61] and later for the 3-D case taking into consideration plastic deformation [62]. In general, the SCF of a non-homogeneous material is location-dependent and in general there is more than one location along the notch (es) where the stress becomes critical as to reduce significantly the load-carrying capacity of the structure in question.

2.3 Multiple Discrete Notches

That the stress concentration is relaxed by the addition of neighbouring irregularities, it is a fact well-known for a long time[3, 52], Fig.7. Therefore, more realistic 3D-

surfaces concentrate, fortunately, less stress than their idealized 2-D profile versions[5]. The Finite element method has made the solving for the SFC due to complex and multiple discontinuities a rather simple task. However, multi-physical problems required the need of theoretical—or at least empirical—solutions, in order to couple mathematical relationships that properly model the mechanical behaviour of complex discontinuities with those related to fluid and thermodynamics, wave propagation, heat transfer, electricity, just to name a few. Empirical relationships have been obtained for a large number of configurations, as it can be readily corroborated through the literature [3, 34, 41, 52, 70–73].

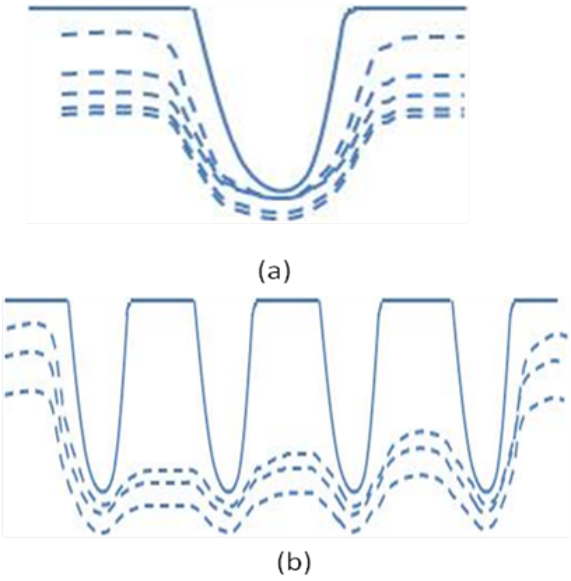

Fig. 7. (a) Single-notch stress lines. (b) Periodic-discrete-notch configuration. Stress is relaxed due to neighboring notches.

The multiple-periodic notch problem (Fig.7b) may be approximately reduced to a single-notch configuration (Fig.7a). This was first suggested by Neuber [52], and then

[5]However, there are cases when the reserve can happen, theoretically. For example, when the Poisson's ratio is between $(1 - \sqrt{2})$ and 1/2

others followed the idea[74, 75]. The German scholar proposed a method to relate the SCF of a single-notch to that of a multiple-notch one, having spacing between notches λ, by reducing the notch's depth, d, via a factor, γ, to an effective depth, d^*, as follows:

$$\gamma = \frac{\lambda}{\pi d} \tanh(\frac{\pi d}{\lambda}) \tag{2.4}$$

and

$$d^* = \gamma d \tag{2.5}$$

Thus, for a multiple-elliptical-notch configuration under normal tensional stress, for example, the stress concentration factor at each notch can be safely estimated by equation (2.1), where a is to be substituted by d^* of (2.5) and in equation (2.4), d is to be equal to a.

For several decades this method was used with little to no modification despite the fact that Neuber's method can significantly overestimate the SCF[75], for some geometrical configurations and loadings outside Neuber's assumptions—his assumptions were sharp shallow notches at the edge of a half plane under shear loading. Very recently, two modified expressions were suggested[75] to correct the effective depth, d^*, mismatch. The corrections, which does not modify the final form of the effectively single-notch simplification, change equation (2.4) to the following two:

$$\gamma = \frac{\lambda}{2\pi d} \tanh(\frac{2\pi d}{\lambda}) \tag{2.6}$$

For shear stresses; and,

$$\gamma = \frac{\lambda}{3\pi d} \tanh(\frac{3\pi d}{\lambda}) \tag{2.7}$$

For notches under normal stresses. Therefore, the problem of multiple periodical notches can be very well estimated using an equation similar to the form of Inglis' result, either equations (2.1) or (2.2), when the proper corrections suggested by equations (2.6) and (2.7) are applied.

A perhaps more difficult problem, that of closely located irregularities, has been recently solved numerically by Savruk and Kazberuk [70], using well-known singular integral equations[76] for periodic curvilinear notches in an elastic plane. this problem, however, still remains unsolved analytically.

2.4 Continuous Periodic Configuration

It seems that Gao [16, 77] was the first to investigate the effect of continuous surfaces—profiles—on the load-carrying capacity of bodies. In that outstanding development, Gao employed some elastic *Green's functions*[78] for a surface considered perfectly flat and treated the sinusoidal surface (see Fig. 8) as being perturbed from that referential plane. After the flat surface has been perturbed, the stress and displacements for the rough surface(T_{ij}

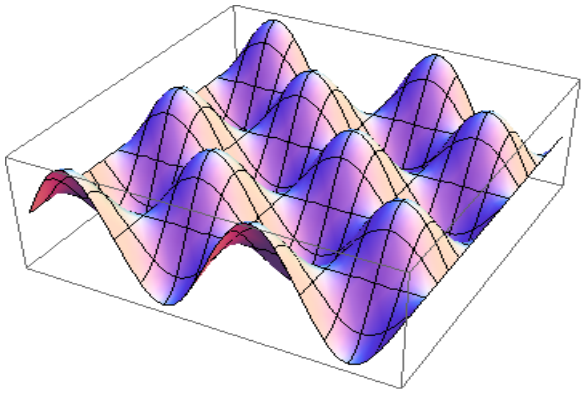

Fig. 8. A sinusoidal surface. The maximum SCF is found at the troughs of the waves [16].

and u_i) can be defined in terms of the reference state values (T^r_{ij} and u^r_i) and the perturbed elements (δT_{ij} and δu_i), as:

$$\begin{aligned} T_{ij} &= T^r_{ij} + \delta T_{ij} \\ u_i &= u^r_i + \delta u_i \end{aligned} \tag{2.8}$$

In order to solve eqn.(2.8), we need suitable expressions for the perturbed elements, δT_{ij} and δu_i. In [16] it was shown that the maximum stress concentration factor at the most concave locations on a sinusoidal 3-D surface can be expressed as:

$$SCF^{3D} = 1 + 2\sqrt{2}(1+\nu)\pi(\frac{a_s}{\lambda_s}) \tag{2.9}$$

Where ν is the Poisson's ratio, a_s is the amplitude of the sinusoidal wave, and λ_s is the wavelength.

2.5 Randomly Degraded Surfaces: the Problem to Solve

Materials are endlessly experiencing alteration, both at atomic and macroscopical regimes. The third law of thermodynamics elucidates—among other basic concepts—that, unless at absolute zero temperature, atomic structures are intrinsically unstable and therefore prone to change to a more stable state; nevertheless, for many materials this rate is a rather unhurried process. Both molecular and macroscopic changes can occur as a result of energy input to the material system, introduced through the surface, or boundary, or developed within the volume of the material.

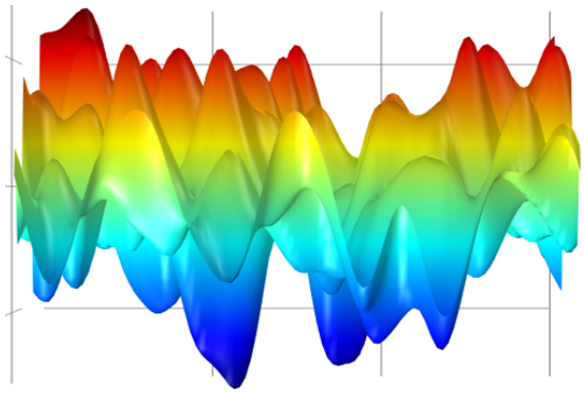

Fig. 9. Random rough surface with a prescribed finite auto-correlation length and whose heights are normally distributed

Assuming only through-boundary interactions, it is generally the case that surfaces are more susceptible to these morphological alterations than the interior part of the material. Almost any known natural phenomenon can cause materials degradation: heat, light, short-wavelength electromagnetic radiation, radioactive emissions, chemicals, mechanical stress and interactions with bacteria, fungi or other life forms. Despite the need for understanding the fundamental mechanisms of each particular physical, chemical, biological, etc., degrading phenomenon, the fact is that they seldom act individually. Instead, they seize the structural integrity of surfaces by the accumulation of a large number of small destructive events. Granted, most of these small attacks are usually of low probability, although the magnitude of the impact would depend on the size of the surface; (Consider, for example, the comparison of a corrosive attack on a bridge versus the same attack on a MEMS metallic device). But the build-up effect of these low-probability events lead to morphological changes on the surfaces that can be modeled mathematically using the Central Limit Theorem[24, 79]. Using the foregoing physical fact, in chapter 6 we derive a solution to the stress concentration factor for an elastic surface possessing a continuous height distribution of the Gaussian type.

CHAPTER 3

FUNDAMENTALS

In this chapter, we briefly discuss fundamental physical and mathematical insights considered crucial to our study.

3.1 Random Degradation

Materials are incessantly experiencing transformation, both at molecular and macroscopic levels. The third law of thermodynamics elucidates—among other basic concepts—that, unless at absolute zero temperature, atomic structures are intrinsically unstable and therefore prone to change to a more stable state; the foregoing applies even more when atoms of a guest material are brought near to atoms of a host material. Both molecular and macroscopic changes can occur as a result of energy input to the material system, introduced through the surface, or boundary, or developed within the volume of the material(s). Consequently, this can result in morphological changes that can drastically alter material behavior and performance.

3.2 Internal Degradation

Let us consider first degradation within the volume of a solid body. There are mechanisms which can degrade the material within its volume, even if transport of degrading agents takes place through the boundary surface. As an example, nuclear-fuel pellets, which could be made of Uranium dioxide—or other constituents—experience internal changes due to mechanisms related to nuclear fission; over time, its stoichiometry changes slowly, which leads to new material properties, cracking, and fission gas release[80]. Con-

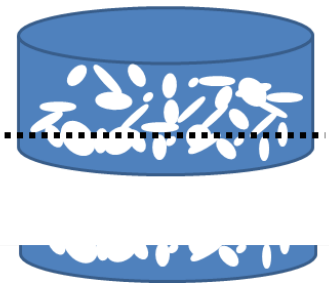

Fig. 10. (Top): Internal flaws in a solid due to internal degradation. (Bottom): A cross-section cutout of an internally flawed solid can be viewed as rough surface

sequently, the thermal conductivity of the UO_2 pellet decreases, as it is affected by porosity and burn-up. In turn, this burn-up permits: the introduction of fission products being dissolved in the lattice, the precipitation of fission products such as palladium, the formation of fission gas bubbles due to fission products such as xenon and krypton, and radiation damage of the lattice[80].

For all our purposes, internal damage in materials introduces voids within its volume that can be treated as internal flaws, which have always been an important topic in statistical fracture mechanics. A proper cut out of a section of a material allows the internal cracks to be analyzed as if it was a surface roughness, as presented in figure 10. In this case, we have assumed there is some kind of orientation of the cracks, which could be the case when only limited types of degrading phenomena are present, and this is what happens in mechanisms of degradation of a fuel pellet, for example. Moreover, as it will be seen in section 3.3, when the number of degrading events is large—whether they are random or not—the cumulative effect of them can be mathematically simulated. However, there are situations in which the degradation processes render the final degraded material non-homogeneous, as it might occur in a nuclear fuel pellet; in that particular case, even hydrostatic stresses

produce the same effects that deviatoric do. (Whatever the case may be, the mechanical behavior and properties of degraded nuclear pellets can alternatively be studied using molecular dynamics, but that is beyond the scope of the present work.) The approach to be used herein includes the prediction of failure of bodies that can be assumed both to possess such internal damage that it can be represented by a cutout surface similar to that of figure 10, and to remain homogeneous. Therefore, our analysis is reduced to surface degradation, which it is discussed in the following section.

3.3 Surface Degradation

Assuming only through-boundary interactions, it is generally the case that surfaces are more susceptible to these morphological alterations than the interior part of the material; therefore, surface degradation is crucial in the understanding of the loss of performance of components[14]. Almost any known natural phenomenon can cause materials degradation: heat, light, short-wavelength electromagnetic radiation, radioactive emissions, chemicals, mechanical stress and interactions with bacteria, fungi or other life forms. Despite the need for understanding the fundamental mechanisms of each particular physical, chemical, biological, etc., degrading phenomenon, the fact is that they seldom act individually. Instead, they seize the structural integrity of surfaces by the accumulation of a large number of small destructive events. Granted, most of these small attacks are usually of low probability–although the magnitude of the impact would depend on the size of the surface (Consider, for example, the comparison of a degrading attack on the surface of an aircraft carrier versus the same attack on a micro engine). However, the sum effect of these events of small likelihood lead to topographical alterations on the surfaces that can be mathematically modeled via the Central Limit Theorem.

As importantly, there are several applications for which it is desirable to introduce surface roughness for engineering reasons. In the field of tribology for example, roughness

is often beneficial for either contact or friction improvement. Likewise, in dental implant research, it has been established that osteoclast and osteoblast activity is enhanced through microroughness of titanium or titanium alloy implant surfaces.

3.4 Central Limit Theorem Applied to Surface Degradation

Let X_1, $X_2...X_n$, be a series of variables representing the size (depth, volume, etc.) of material removed or displaced as a consequence of respective degrading events, E_1, $E_2...E_n$, acting on a surface like the one shown in Fig. 1. In the same manner, let $X_1^{'}$, $X_2^{'}...X_m^{'}$, be a set corresponding to synergistic events, $E_1^{'}$, $E_2^{'}...E_n^{'}$, that are obtained from the possible combining attacks of two or more X_i. For example, $X_1^{'} = SC(X_1, X_2)$, where the function SC maps individual events effect into their combined effects. Now, let us further assume that all X_i's are random independent variables. This is a very reasonable assumption, since one expects that these environmental, damaging attacks often act independently one from the other. (Even though there are some events that could be inter related, yet when the number of independent E_i is considerably large then this assumption holds reasonably well). Then, $X_i^{'}$, are also random variables since the sum and multiplication of two or more random variables is indeed another random variable. Now we can apply the Central Limit Theorem to simulate random degradation, assuming a large number of degrading events. The Central Limit Theorem (CLT) explains the behavior of the sum of random variables. Let $Z_1...Z_n$ be random variables such that $Z_i = X_i + X_i^{'}$, with sum,$S = \sum_{k=1}^{N} Z_k$,then CLT predicts that S will have a Gaussian distribution provided that:

a. Each summand that is not negligible compared to the dispersion of the entire sum has a distribution close to Gaussian.

b. The maximum of the absolute value of the negligible summands is itself negligible compared to the dispersion of the sum.

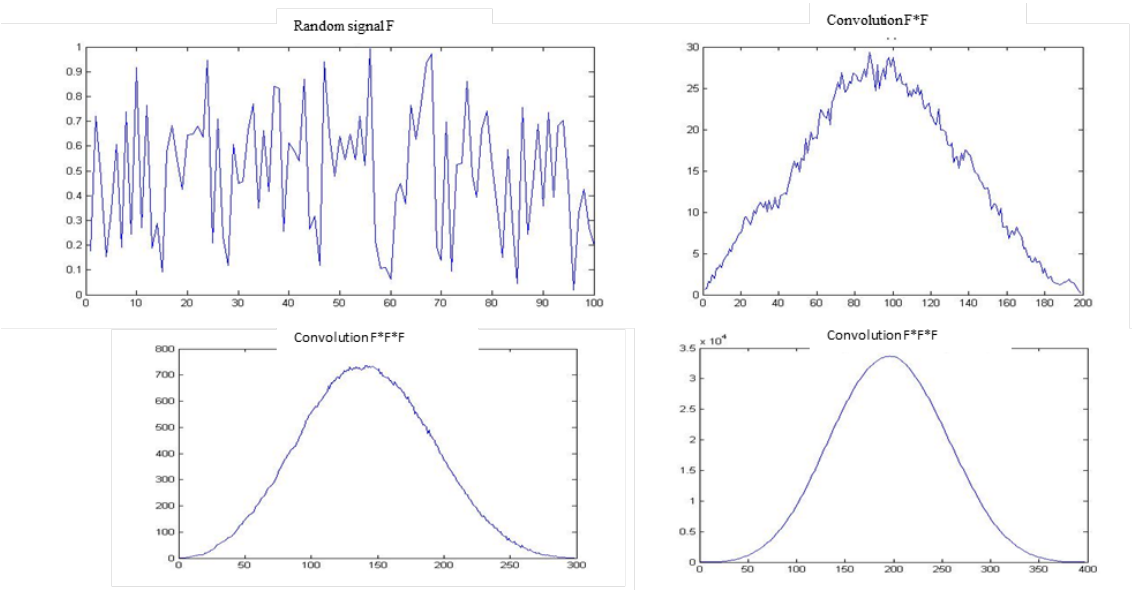

Fig. 11. A visual prove of how a random event when convoluted with itself grows into Gaussian. Notice that it only takes 4 convolutions to clearly see bell-shape Gaussian distribution.

Consider figure11. The upper left corner shows a random signal which could signify the effects of a random attack of certain degrading event on a certain surfaces profile. The other three figures (upper right, lower left, and lower right) show how when combining this random effect with other random ones, the behavior of the combined effect makes the degradation (distribution of depth) grow progressively into a bell-shape characteristic of a Gaussian (normal) distribution. So for our study, the size of material removed will be considered to eventually grow into a normally distributed random function. Consequently, if the size of pieces removed, due to degradation, is normally distributed so is the size of the pits left on the surface of the material.

3.5 Definition of Early Stage of Degradation

It is well known in fracture mechanics that materials may be weaken by the presence of flaws. Contrary to what the traditional strength of material analysis would predict,

this phenomenon takes place at stresses below the material's yield strength. In reality no material is flawless but all possess some degree of impurities and flaws. However, when dimensions of flaws are below certain critical value, strength of materials approach is sufficient to predict failure. On the other hand, when flaws are above that critical dimension then one must resort to fracture mechanics.

Above critical size, the presence of a flaw concentrates sufficient stress in its neighborhood to cause nucleation of fracture under some loading. The critical size of a flaw, a_c for a given material of yield strength, σ_y, and fracture toughness, K_c, is given by:

$$a_c = \frac{1}{\pi}(\frac{K_c}{\sigma_y})^2 \tag{3.1}$$

In the next section the use of poly methyl methacrylate (PMMA) will be justified in the experimental work developed. Using tabulated values of this polymeric material [81] of $\sigma_y = 70MPa$ and $K_c = .7MPa\sqrt{m}$, one gets, $a_c \approx 30\mu m$. This is of course for the case of a single flaw. For multiple flaws or notches, this dimension must be a little higher since neighboring pits tend to relax the stress concentration.

When dealing with random roughness with Gaussian distribution (our case), one is interested in finding a critical roughness or degradation which can make stress concentrate sufficiently as to cause brittle failure due that particular level of damage. In such configuration, it is expected to find pits that are below and above the critical size given by equation (3.1), but not too far from it. So we define "early stage of degradation" as the range of roughness around the critical level roughness that would concentrate stress sufficiently as to localize fracture. Based on our own previous studies [18], for PMMA, the critical root-mean-square roughness was found empirically to be within the range $\approx 10 - 20\mu m$.

3.6 Implications of the Use of Poly Methyl Methacrylate

The challenge at this point was to physically produce surfaces modeled via the Central Limit Theorem, as described before. A suitable material was needed to efficiently accomplish the purpose. Poly methyl methacrylate (PMMA) was selected as the base material[82]. The benefits of using this polymeric material are enormous. A polymer is a synthetic or natural material consisting of molecules strung together to form a long chain. The properties of a given polymer depends on the basic molecules (a mer unit, repeating unit) making up the polymer, the length of the chain, and the arrangement of the polymeric chains. In the particular case of PMMA, the repeating unit is $COOCH_3 - C_2H_2 - CH_3$, and the chains are arranged in a random manner making this polymer amorphous[83]. PMMA has been successfully used in many applications due to its excellent mechanical properties and low cost [84]. Except for micro scale applications, PMMA can be easily ablated without causing secondary mechanical effects on the surface [85]; and it has been reported that PMMA has a better cutting edge surface quality than, for example, polypropylene and polycarbonate [86]. It can be found commercially with relatively low surface roughness (10-200 nm) [84], so even minute damage caused on it (see previous section) could be distinguished. Also, at room temperature it behaves brittle and ductility starts to show above approximately 30 degrees Celsius (see figure 2.4) [81]. Based on those characteristics, in this study, PMMA is used to broaden the knowledge of mechanical failure of materials at initial service surface conditions and during random surface damage accumulation and environmental degradation. This is accomplished by laser ablation of repeated random rough surfaces on PMMA beams and their mechanical analysis.

3.6.1 PMMA's Mechanical Behavior Dependence on Temperature

In general, the mechanical properties of polymers not only vary from type to type, but also they depend greatly on temperature and strain rate; and some properties change almost discontinuously in the neighborhood of a critical temperature called the glass-transition temperature (T_g). T_g has been defined by [83] as the temperature at which the forces holding the distinct components of an amorphous solid together are overcome by thermally-induced motions within the time scale of the experiment, so that these components become able to undergo large-scale molecular motions on this time scale, limited mainly by the inherent resistance of each component to such flow. In other words, T_g is the temperature above which a thermoplastic polymer becomes a fluid free to flow. For uncrosslinked PMMA, T_g has been found experimentally to be around 378 Kelvin (105^oC) [83]; and well below that value, it behaves as an organic glass, and elastic solid with a relative high Young's modulus of about 3.3 GPa (tension) at about room temperature and relatively medium to low strain rates[[81]. There is a transition range around T_g in which viscoelastic phenomena predominate. However, the present study will consider only cross-linked PMMA and a temperature range from about 10 to about 30 degrees Celsius, which is well below T_g (although most of the work carried out was at room temperature). In this range of temperatures, the mechanical behavior of PMMA goes from very brittle to a slightly ductile material. Figure 12a is a stress-strain curve for a type of an uncrosslinked PMMA for a range of temperatures, as reported in the literature [81]. Notice that at 4^o C, there is no display of plastic deformation, and the material could be considered—at least for practical purposes—fully brittle. At room temperature (20^o C), there is a very small amount of plastic deformation, and the material can be taken as semi-ductile. For the present study, however, crosslinked PMMA was studied at room temperature. Its mechanical behavior is depicted in a plot of stress vs strain shown in figure 12b. Note that even though the

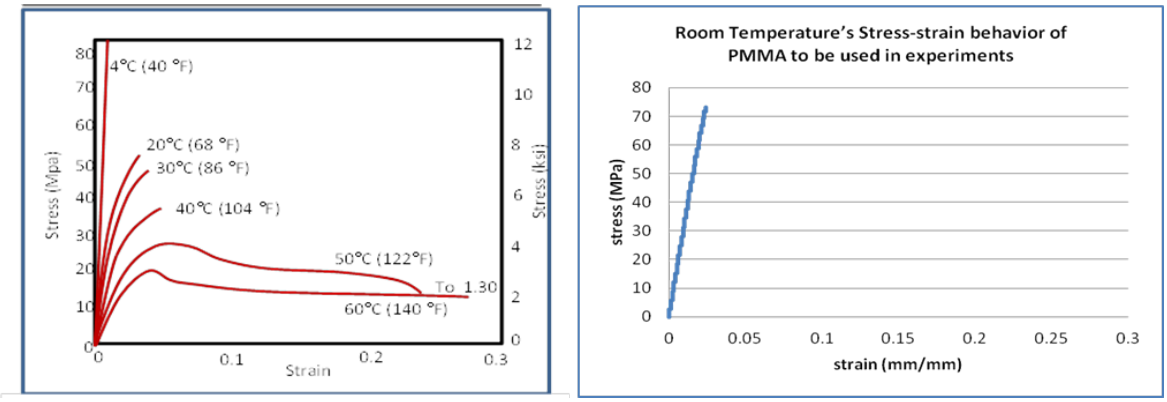

Fig. 12. (Left): Brittle to ductile behavior as a function of temperature for poly methyl methacrylate from [81]. Uniaxial tensile loading conditions; (right): PMMA mechanical bending behavior at room temperature. Three-point flexural loading conditions. Deflection rate= 0.2 in/min.

temperature is much higher than 4^o C, crosslinked PMMA presents a brittle behavior much earlier. Therefore, lowering the temperature to obtain brittle behavior will only increase its brittleness. Also, temperatures will be increased to obtain the desired ductile transition. At low levels of ductility, it is expected a transition of correlations of the controlling parameters at brittle conditions. Another important aspect to consider here involves the fact that since PMMA is an amorphous polymer—as opposed to a crystalline one—it seems to obey a time-temperature superposition principle [87]. This principle might allow the extension of data found at distinct temperatures by using it in a time range at a single temperature.

3.7 Linear Elasticity

Perhaps, the most important and most characteristic mechanical properties are called the moduli. A modulus is a measure of how the material resists strain upon an applied stress—i.e. the ratio of applied stress and the corresponding strain. If for a particular material and within a given range, that ratio happens to be constant, then the material is said to behave linearly elastic in that range. The three most important moduli are called bulk

(K), shear (G), and Young's (E), corresponding to volumetric, shear, and axial situations, respectively. There are other moduli used depending on the application, such as the reduced modulus for nanoindentation. For a bending test—present research—Young's modulus of elasticity applies. The reciprocal of these moduli are called compliances. Let us define k, J, and C as the compliances corresponding to K, G, and E, respectively.

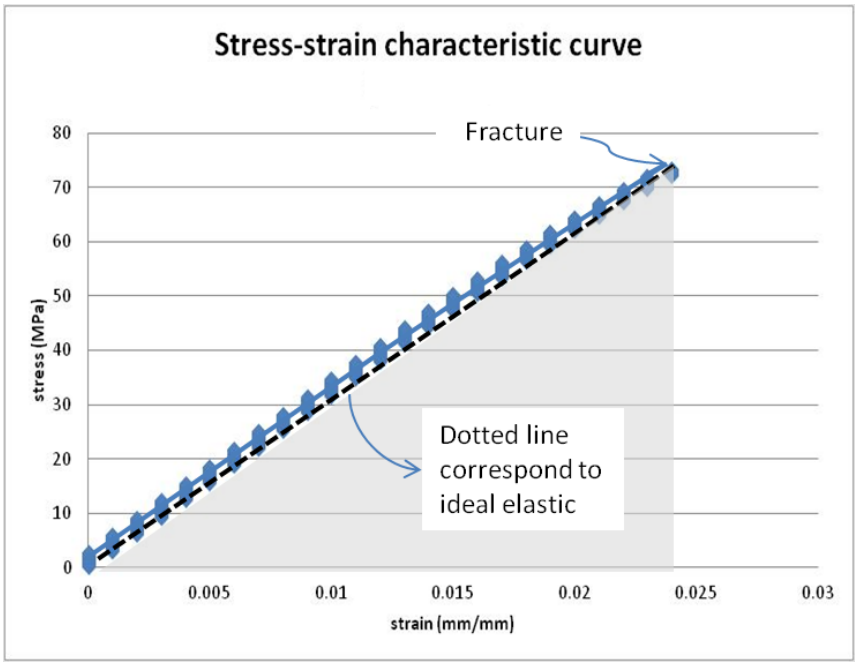

Fig. 13. Notable linear-elastic behavior at room temperature of PMMA used in the experiments.

Based on experimental preliminary evidence, undamaged PMMA can be assumed to behave perfectly linear-elastic for temperatures up to approximately 20^o C. In case of roughened PMMA, this temperature can be higher. Figure 13 shows a plot of data obtained from a bending test of specimens of PMMA at room temperature. The tests were three-point bending using a deflection rate of 0.2 in/min. The linear behavior of the material can be notably observed. Additionally, E was found to be around 3.2 ± .2 GPa, which is in complete agreement with modulus of elasticity reported in literature[81]. For this case, the field equations of liberalized isotropic isothermal elasticity can be applied [87]:

a. 3 equations of motion:

$$\frac{\partial \sigma_{ij}}{\partial X_j} + \rho(T) b_i = \rho(T) \frac{\partial^2 u_i}{\partial t^2} = 0 \tag{3.2}$$

b. 6 Hooke's Law equations:

$$\sigma_{ij} = \lambda(T) \epsilon_{kk} \delta_{ij} + 2\mu(T) \epsilon_{ij} \tag{3.3}$$

c. 6 geometric equations:

$$\epsilon_{ij} = \frac{1}{2}\left(\frac{\partial u_i}{\partial X_j} + \frac{\partial u_j}{\partial X_i}\right) \tag{3.4}$$

Equations (3.2) thru (3.4) constitutes a total of 15 equations, 6 stresses, 6 strains, and 3 displacements. Where σ_{ij} is the Cauchy stress tensor; X_j are the Cartesian coordinates for the material description, so that X_1, X_2, X_3 represent parcels of material; ρ is the density of the material; T is the temperature of the system; b represent the body forces; u is the displacement of parcels in a given direction; t is time; λ and μ are material properties related to the different moduli; ϵ_{ij} is the strain tensor; δ_{ij} is the Kronecker–delta function, equals to unity when i=j, otherwise, zero. (Herein we call parcel the minimum volume that a continuum can be divided into while still behaving as a continuum itself—others call it particle, as in [87] for example). Notice that the material properties, λ, μ, and ρ are dependent on temperature; thus, even though these equations were prescribed for isothermal conditions, at each distinct temperature considered, they have different values. As mentioned, we will use equations (3.2) thru (3.4) to develop our boundary-value problem and derivation in chapter 6. However, since one may argue that there could be considerable stretching for this polymeric material (figure 13), then finite-strain theory must be at least considered for discussion. This state of affairs is exposed in the following section. However, as it will shown, it was found that small-strain theory serves well for the range of conditions studied in the present work(see Chapter 5)

3.8 Finite Strain Theory

It is well know that small-strain theory applies very well to most metals. However, in general when dealing with polymeric materials it is often, yet not always, required to take into account the presence or larger strains. The equations of general linearized elasticity, as traditionally developed [87] assume small-strain conditions. Therefore, if large-strain are to be considered then strain must be re-formulated using a deformed state. (In this section, we will use capital letters to describe referential undeformed stated coordinates, and lower case for deformed material coordinates.) This difficulty is solved—not without bringing in complexity—by relating the undeformed coordinates (X_i) to the deformed ones (x_i). The way this is done is by defining a tensor, **F**, called the deformation gradient tensor, as:

$$\boldsymbol{F_{km} = \frac{\partial x_k}{\partial X_m}} \tag{3.5}$$

In other words, **F** relates parcels of material that have been deformed to the undeformed state of those parcels. This can be expressed, also, as $d\mathbf{x} = \mathbf{F} \cdot d\mathbf{X}$. By some simple mathematical manipulation, and relating both **F** and the strain tensor of equation (3.4) to the change in the squared length of the curve before and after deformation, one gets an expression of **E** (strain tensor) with respect to **F**, as:

$$\boldsymbol{E = \frac{1}{2}(\mathbf{F}^T \cdot \mathbf{F} - I)} \tag{3.6}$$

(Note that d**x** has been defined as the vector location occupied by the deformed expression of material vector d**X**.)

As it will be seen, from the experimental work the strain values will be obtained at a sufficient large number of points during the test. This can provide values for the displacement gradient both in terms of the undeformed state (Piola-Kirchoff) and in terms of the following immediate one (deformed state). Hence, we could couple equation (2.5) with

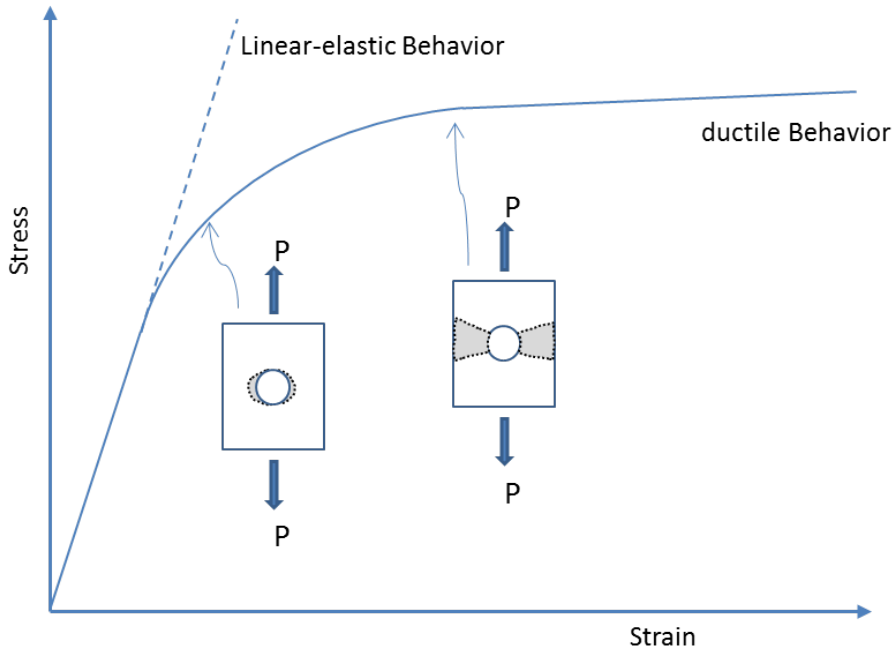

Fig. 14. Stress-Strain behavior of a notched member showing distinct regions of mechanical behavior [1].

Hookes law for the regions where the material remains linear. However, small-strain theory was initially used as a preliminary tryout and it turned out to give consistent results when experiments were compared with analytical work for simple well-known configurations. Additionally, one may recall that finite-strain theory was initially developed for highly stretchable materials such as hydrogels, human tissue, rubber, etc. In our case, deformation does not exceed 3% strain, which although greater than for most structural metals, it is still far below that of highly stretchable materials.

3.9 Effects of Multiple Well-defined Discontinuities:2-D Problem

Surface discontinuities impact failure of the entire volumes of material they bound, depending on both the geometry of the discontinuity and the degree of brittleness of the material in question.

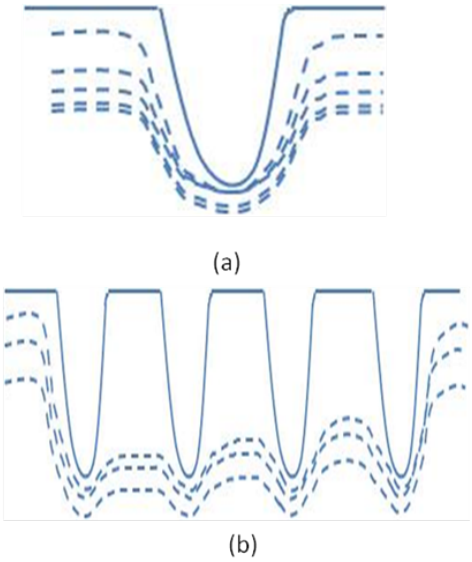

Fig. 15. Visual schematic of equal-stress lines distribution due to (a) a single discontinuity, and (b) multiple discontinuities. Stress is relaxed due to the presence of neighboring pits

It has been known for a long time that the presence of discontinuities in a material, subject to a remote load, introduces stress concentrations which depend, to a great extent, on the geometry, location and orientation of the discontinuity with respect to the overall dimensions [1, 2]. At a local parcel of material, the stress concentration factor, K_t, is defined as the ratio of the local stress to the remote stress:

$$K_t = \frac{\sigma_{local}}{\sigma_{remote}} \tag{3.7}$$

This definition of K_t applies well only for linear–elastic materials behavior. This type of behavior is usually seen in brittle materials, and therefore applies to the material and conditions used in this study, see chapter 4. For more ductile behavior, equation (3.7) over-estimates K_t, mostly because more energy gets stored into the larger plastic zone around the discontinuity (e.g., notch). Consider the behavior of single-notch members over a wide range of applied loads for a ductile material,as depicted in figure 14. For brittle materials,

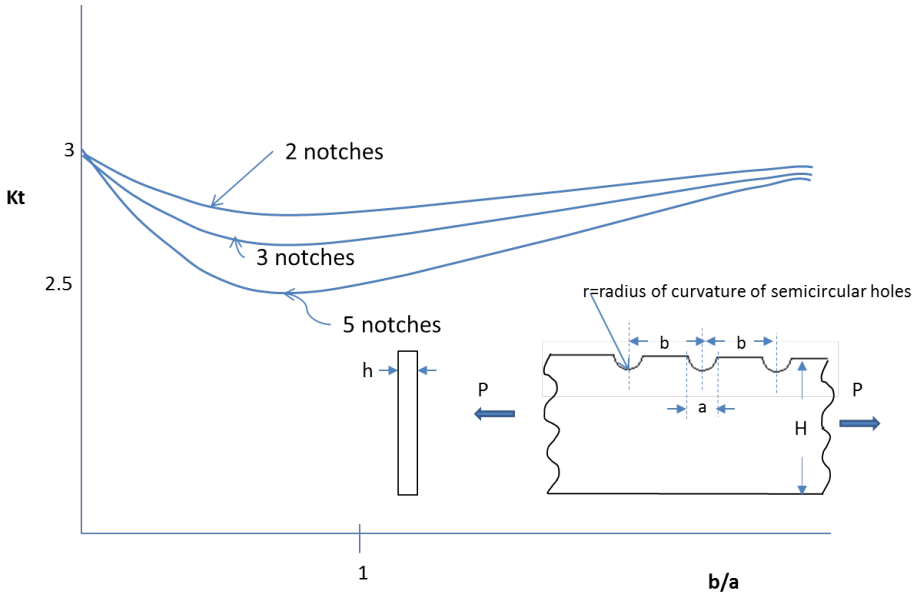

Fig. 16. Schematic-plot of stress concentration factor for tension of a flat member with periodic semicircular notches. r/H=18. Based on data from [3]

the behavior of a specimen is described simply by the linear section of the curve in figure 14. When two or more discontinuities are present in the material, the situation could change completely. A neighbor material singularity could cause a relaxing effect on the stress accumulation due to another singularity—unless the separation between singularities is far enough so that the effects can be neglected. This state of affairs can be visualized in figure 15. Equal-stress lines can be analogized to flow streamlines. One important aspect to keep in mind is that the presence of multiple discontinuities causes a relaxation phenomenon in all directions around a particular pit—except in the direction of the free surface. This decrease in K_t can be better visualized using figure 16, which is a cartoon-plot (based on data obtained from [3]) of K_t for a rectangular member with a multiple-notch configuration, under simple tensile loading. Notice—among other interesting behaviors—that the value of K_t decreases with the number of notches: the presence of a neighbouring discontinuity, as long as it is within the concentration field, alleviates the stress concentration around a

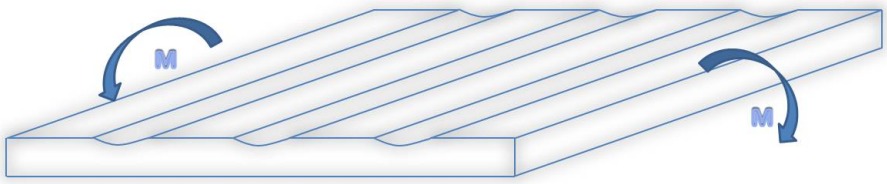

Fig. 17. Schematic of specimen with three grooves on its surface and under bending loading

particular discontinuity.

3.10 Effects of Multiple Discontinuities:3-D Problem

The previous analysis can be extended to 3-D configurations, with some warning limitations. Consider the grooved member shown in figure 17 which possesses 3 equally-separated grooves with one being in the center of the member. Notice that the grooves are perpendicular to the bending moment applied to the system, and they are separated by islands of material of more or less the same width. It has always been believed that stress concentration will be relaxed from the center groove by the effect of the presence of the other two grooves. Of course, the distance between grooves (that is the width of the islands) could remarkably change the situation, in a way that, distant grooves might not cause any effect on others, whatsoever. That this relaxation takes place can be observed from figure 18 obtained from finite element analysis. But, as stated previously, well-defined notches are seldom present on realistic degraded surfaces. In-service surfaces present a rather random configuration of discontinuities, as it will be extensively discussed in the foregoing sections and chapters. The distribution of local K_t over the surface is expected to be more complex than for a case with multiple equal-size discontinuities. To begin to perceive this complexity, let us consider again our three-groove member of figure 18. As an example, let us replace part of the middle groove with material as to form a tendon between islands such that islands and tendon together look like a letter H, as shown in figure 19. When the

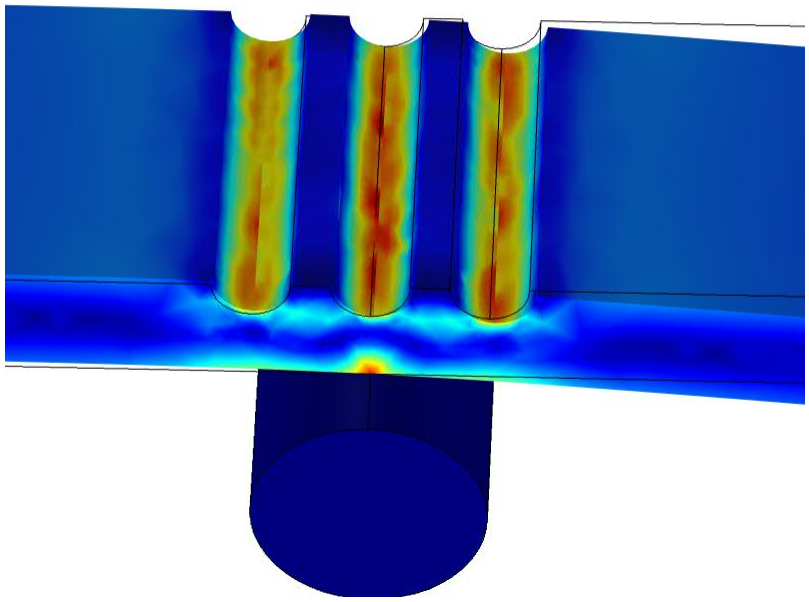

Fig. 18. Finite element simulation of beam under bending. Stress along central groove is relaxed due to presence of neighboring grooves

width of the tendon is large enough, the relaxation phenomenon described previously takes place, and the consequent reduction of stress concentration occurs in the middle groove. However, when the tendon is sufficiently narrow, stress accumulates mostly in the tendon itself, thus relaxing the stress that concentrates at the grooves. It is important to emphasize again that for a random surface—which of course contains an unexpected irregular configuration of discontinuities—one would expect a more complex combination of parameters that control where and when failure will occur. One of the goals of the present proposed work is to find empirically surface and material parameters that control failure through experimental study. Additionally, we will also attempt to find an analytical solution of the stress concentration factor of surfaces with random configuration of discontinuities, using a perturbation method.

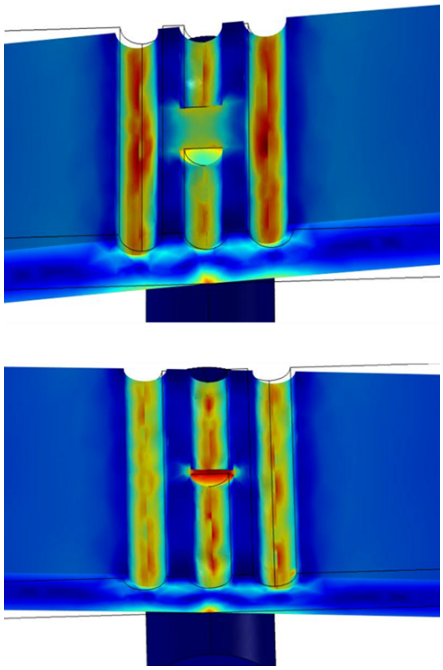

Fig. 19. When less simple discontinuities are introduced behaviors can vary. (Top): Thick tendon relaxes middle groove and concentrates stress in neighboring ones; (Bottom): Thin tendon concentrates stress around itself.

3.11 Perturbation Method for Stress Concentration Problem

Perturbation theory allows the approximation to the solution of a problem with given conditions B, by beginning with the exact solution of a related problem with conditions A. It is required, therefore, that conditions B only deviate slightly from A. In other words, B is a perturbed A.

In order to attempt to find an analytical solution for the stress concentration due to a random rough surface on a nominally brittle material, a perturbation method on a half-plane will be used. The method thinks of the non-flat surface as a perturbed flat one. Results will be compared with the experiments performed at similar conditions of brittleness; hence, linear-elastic behavior will be assumed. Since the surfaces to be considered are at early stage of degradation, they can be considered as a small perturbation from a nominally flat surface. Only to show the method to be used to find the stress concentration factor, let us briefly present a summary of the problem setup (the complete derivation is presented in chapter 6). Let figure 20, be a flat surface with Cartesian coordinates as shown, and a rough surface which represent the deviation from the mean. Since bending loading is to be used, the damage surface can be considered to be in tension in the neighborhood near the flat surface (this is a reasonable assumption, since the maximum average roughness of degradation is to be about 15 thousandths of the specimen's bulk thickness.) Let $d(x')$

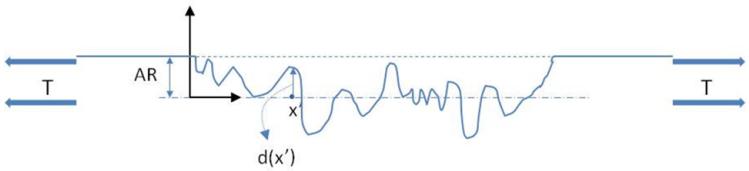

Fig. 20. A random surface can be thought of as one previously flat but to which material has been added and/or from which material has been removed randomly.

be the distance between the mean and the local spread at point x'. If a point force F is

considered at an arbitrary point (x,y), and treating $d(x')$ as infinitesimal, the change in total energy ($\Delta\Pi$) of the system is given by:

$$\Delta\Pi = F_i \Delta u_i(x, y) + \int_{\infty}^{-\infty} w d(x') dx' \tag{3.8}$$

Where $F_i \Delta u_i(x, y)$ is the work done by the force at an incremental displacement $\Delta u_i(x, y)$, and w represents the strain energy density distribution along the surface. Solving equation (3.8) involves quite a challenge since $d(x')$ is, at best, a Gaussian distribution function.

3.12 Flexural Tests on Slightly–Roughened Surfaces

Our goal of finding how a slightly damaged surface impacts the failure of a polymeric body requires the use of flexural tests. Since the damage is small compared to the overall thickness of the specimens to be used (in the order of 10 thousandth), the entire damaged surface can be considered as outer fiber. Test methods to determine flexural properties of plastics have been standardized since 1970 by ASTM [88–90]. These methods apply to both rigid and semirigid materials. It is limited to materials that fail in the outer surface of the specimen within certain limit of outer-fiber strain (5 %). Figure 21 shows a typical three-point flexural set up with the corresponding parameters.

Following the standard procedure, calculation of certain flexural properties can be made as follows:

3.12.1 Flexural Stress (σ_f)

The flexural stress (σ_f) is the maximum stress in the outer surface of the specimen which occurs in the midpoint of the span length (L). The way σ_f is calculated depends on the value of L-to-t ratio. In our case, $\frac{L}{t} \approx 25$, thus it can be reasonably approximated as [88]:

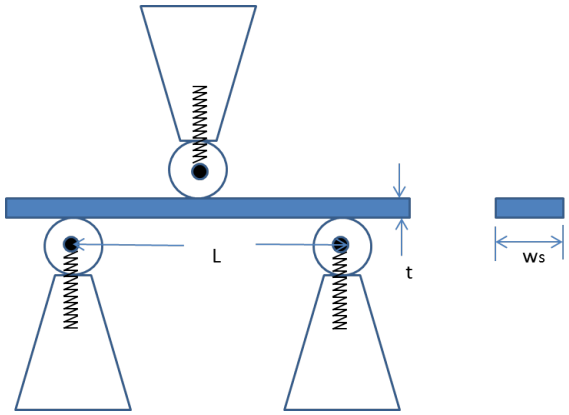

Fig. 21. Three-point flexural test. L= span length and t=thickness of specimen. ASTM D790 is the standard for acrylic testing.

$$\sigma_f = \frac{3}{2}\frac{PL}{W_s t^2}[1 + 6(\frac{D}{L})^2 - 4(\frac{t}{L})(\frac{D}{L})] \tag{3.9}$$

where:

σ_f = stress in the outer fiber at midpoint, MPa

P = load at a given point on the load-deflection curve, N

L = span length, mm

W_s = width of the specimen tested, mm

t = thickness of the specimen tested, mm

D = deflection of the centerline of the specimen at the middle of the span length, mm

From the above equation (3.9), one can also find the flexural stress at break (σ_{fB}).

3.12.2 Flexural Strain (ϵ_f)

It is defined as [88] "the nominal fractional change in the length of an element of the outer surface of the test specimen at midspan, where the maximum strain occurs"; the formula of equation (3.10) may be used to calculate it:

$$\epsilon_f = 6\frac{Dt}{L^2} \tag{3.10}$$

where the parameters involved are as described before.

3.13 Replicates of Random Surfaces. Statistical Analysis

The mathematical model introduced in section 3.4 and which is fully described in chapter 4 allows us to control the different topographies to be realized on the specimens. This adds great advantages to the study, and the impetus is very broad. Let us consider the field of protective coatings, as an example of the applications. Investigation of the degradation dynamics of surfaces have led to the manufacturing of, for instance, in–laboratory accelerated weathering equipment, due to the accumulated knowledge and quantification of the aforementioned stresses. Devices for artificial weathering of coatings are widely used to simulate environmental parameters such as temperature, UV radiation, humidity and gaseous pollutants. This type of equipment has, to some extent, served well in facilitating in-lab study of processes that otherwise would take enormous periods of time; yet there is ongoing research to improve this procedure since they introduce a new set of uncertainties related to acceleration factors and correlation with outdoor exposure. Also, accelerated weathering chambers do not possess the capability of repeatability of the specimens; instead, each specimen is distinct (although in some cases, statistically correlated), which limits statistical analyses.

The advantage of carrying out experiments with replicates cannot be overemphasized. Experimental studies are scrutinized with respect to, at least, their validity and accuracy. In the heart of the group of factors considered to validate experimental methods lies tests repeatability, which provides a—hopefully reasonable—variation in measurements obtained

by a single experimenter or instrument, on replicates (for destructive tests) or the same specimen (for nondestructive tests). These measurements, in turn, are then appropriately organized, analyzed and interpreted using statistical methods. Hence, in experimental investigations the need of having replicate specimens is crucial. This need becomes even more critical when destructive tests are required, as it is our particular case. As part of our work, we developed a technique to generate and realize different levels of surface random degradation. This method permits to the production of replicates of specimens in order to statistically analyze our results. Traditionally, studies of random rough surfaces have been carried out using single specimens and the results assumed to be equal for the same topography. However, a preliminary related work previously done proves the contrary [18], and this will be discussed fully in chapter 4.

3.13.1 Repeatability and Reproducibility

In the heart of the reliability of experimental results lies the concept of repeatability and reproducibility [91]. The former is a measure of the deviation of a physical quantity for n tests, given the conditions are identical in the n runs. These identical conditions refer to: the same instrumentation, the same facilities (laboratory), the same experimenter, the same replicated specimen, and within a short time period between tests. On the other hand, reproducibility is a measure of the deviation of a physical quantity under more realistic and diversified conditions. It is intuitive that reproducibility be larger than repeatability, in general.

In order to guarantee reasonable levels of repeatability (r) and reproducibility (R), the present work will make use of the recommended values reported in the standard literature [88] for the acrylic material to be used. Tables 1 and 2 contains the recommended values for variability, repeatability and reproducibility, as tabulated by ASTM[88] corresponding

Table 1. Recommended values for variability, repeatability and reproducibility for flexural strength tests for various polymeric materials. ABS = Acrylonitrile butadiene styrene, DAP = Diallyl Phthalate, GR = glass-reinforced, SMC = Sheet molding compounds. V_r, V_R, r and R are defined in the text.

Material	Mean, MPa	V_r	V_R	r	R
ABS	68.9	11.0	41.7	30.6	119
DAP thermoset	98.6	45.4	45.4	128	128
Cast acrylic	112	11.5	77.9	32.6	221
GR polyester	134	9.86	14.8	27.9	41.9
GR polycarbonate	145	35.6	41.7	101	118
SMC	179	32.8	49.6	93.1	141

to flexural strength and modulus measurements, respectively. V_r, V_R, r, and R are given in units of % MPa. As one can notice, PMMA is not in the list of materials recommended. However, we can select other materials with similar properties. For flexural strength values, ABS can be selected since it shows a similar average value as that found for flat PMMA specimens ($\approx 70MPa$); as for the flexural modulus, DAP thermoset shows comparable values as for PMMA ($\approx 3.2GPa$).

Where the V_r, V_R, r, and R are as follows:

V_r = within-laboratory coefficient of variation for the indicated material. It is obtained by first pooling the within-laboratory standard deviations of the test results from all of the participating laboratories: $S_r = [[s_1^2 + s_2^2 + ... + s_n^2]/n]^{1/2}$, then $V_r = S_r$/(overall average of material)×100.

V_r= between-laboratory reproducibility, expressed as the coefficient of variation: S_R =

Table 2. Recommended values for variability, repeatability and reproducibility for flexural modulus tests for various polymeric materials. ABS = Acrylonitrile butadiene styrene, DAP = Diallyl Phthalate, GR = glass-reinforced, SMC = Sheet molding compounds. V_r, V_R, r and R are defined in the text.

Material	Mean, MPa	V_r	V_R	r	R
ABS	2330	33.0	53.0	93.8	150
DAP thermoset	3340	19.9	49.5	56.2	141
Cast acrylic	5580	94.5	111	268	313
GR polyester	5630	24.1	29.0	68.3	82.0
GR polycarbonate	12300	38.1	38.1	108	108
SMC	13400	75.2	95.1	212	270

$(S_r^2+S_L^2)^{1/2}$ where S_L is the standard deviation of laboratory means. Then:$V_R = S_R$/(overall average of material)×100.

r = within-laboratory critical interval between two test results = 2.8 ×V_r.

R = within-laboratory critical interval between two test results = 2.8 ×V_R.

CHAPTER 4

METHODOLOGY

4.1 General Methodology

Figure 22 shows a flowchart of the general methodology used. Enclosed in the dotted rectangle are the steps of a developed technique to produce replicates of random of rough surfaces [79]. Since that technique is also a deliverable in the present work, we will dedicate the first part of this chapter solely to it. In Part II, the methodology of the rest of the work is described.

4.2 PART I: Technique to Produce Replicates of Random Rough Surfaces

4.2.1 Motivation

Validity and accuracy are crucial parameters that need to be carefully considered when carrying out experimental studies. In the heart of the group of factors considered to validate experimental methods lies tests repeatability[92], which provides a–hopefully reasonable– variation in measurements obtained by a single experimenter or instrument, on replicates (for destructive tests) or the same specimen (for nondestructive tests). These measurements, in turn, are then appropriately organized, analyzed and interpreted using statistical methods. The foregoing implies that, in experimental research it is crucial to run tests with replicates of specimens. Furthermore, this is even more critical for studies that require destructive tests, as it is the case of the present work. In the subsequent sections of this chapter, we present a novel technique[79] to generate replicate specimens of surfaces, that

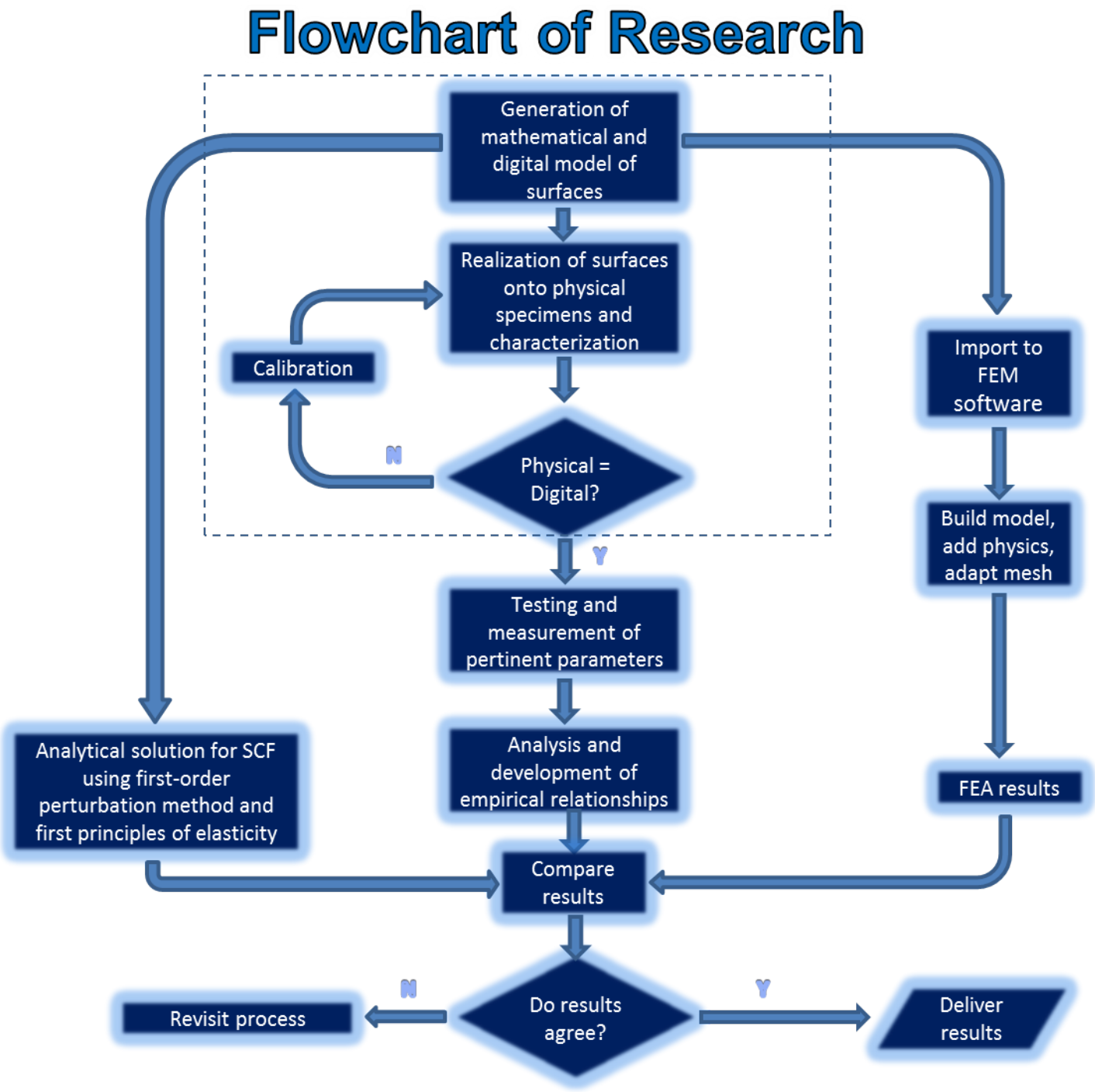

Fig. 22. Flow diagram of general methodology used in the present study

simulate random dynamic degradation. The impetus of this technique is explained next. Structural materials which are exposed to natural weathering or service conditions undergo small attacks of random damaging events which nearly always generate surface roughness. These events, which take place individually, are ultraviolet photons, moisture molecules, pollutant molecules, fast flows, neutron irradiation, thermal impacts, chemicals, biological stressors, sand or dust impacts, and many others. Investigation of the degradation dynamics of surfaces have led to the manufacturing of, for instance, in-laboratory accelerated weathering equipment, due to the accumulated knowledge and quantification of the aforementioned stresses. Devices for artificial weathering of coatings are widely used to simulate environmental parameters such as temperature, UV radiation, humidity and gaseous pollutants [92–94]. This type of equipment has, to some extent, served well in facilitating in-lab study of processes that otherwise would take enormous periods of time; yet there is ongoing research to improve this procedure since they introduce a new set of uncertainties related to acceleration factors and correlation with outdoor exposure[95]. Also, accelerated weathering chambers do not possess the capability of repeatability of the specimens; instead, each specimen is distinct (although in some cases, statistically correlated), which limits statistical analyses.

Additionally, this method finds direct applications in many other fields. For example, in the forensic sciences, where the safeguarding of evidence material is indispensable for multi-testing purposes, replicates are crucial. A common practice of that investigative field consists of obtaining 3-D laser scans of pertaining surfaces and their respective conversion to digital format[96]. Coupling that procedure with this method, one could obtain replicates of rough surfaces on materials that would represent a much less costly alternative than modern 3-D printing, for which there is still, to present time, limited types of base materials that can be used.

As a second example, it is widely accepted that surface roughness and topology of implants affect differentiation and proliferation of bone-producing cells[97–100]. However, the lack of highly controlled replicates of random rough surfaces truncates statistical analysis of the resulting data. In turn, this limitation impedes the proper correlation of surface topological properties to osteo-integration markers. Replicates of random rough surfaces could be used to statistically study bone formation as a function of highly controlled surface parameters such RMS-roughness and autocorrelation length.

Evidently, the problem lies in developing repeatable random rough surfaces, and their realization on specimens that can be then destructively tested and analyzed statistically. This difficulty is due to the complexity and randomness of the small events that lead to surface degradation[101]; yet, these have been stochastically modeled[102] using methods like, Monte Carlo[103] and the Central Limit Theorem[24, 104]. Now, the actual realization of rough surfaces requires a high degree of controllability, in order to produce the repeatability that statistical analysis requires.

4.2.2 Algorithm of the Technique

Following is a set of steps that represent the pseudo-algorithm of the generation and dynamic growth of the surface:

i. Generation of a surface in the form of a 2-D array, in which the entries represent the depth of the surface at some discrete location from a horizontal plane. This plane is represented, in turn, by the other two coordinates corresponding to the indexes of the respective entries.

ii. The value of the depth is subtracted by a certain amount. This process is called here *truncation*. After truncation, the resulting array represents the new initial surface at

which degradation will start. This could represent a machined surface, consisting of a large number of flat points and relatively smaller number of valleys. The level of truncation would depend on the desired conditions that the new initial surface is to have, which in turns depends on the particular application.

iii. The process of truncation is then reversed by adding values to the entries of the 2-D array. This addition is done by steps. The size and nature of the step will depend on the application. This process represents the growth of the surface. For linear growth, the value of the step will be constant. For nonlinear growth, the step will vary as a function dependent on the nature of the process of degradation. The number of the steps however will be determined by how many levels of degradation are needed to be modeled.

iv. Once all the surfaces are properly stored, these are conveniently translated to a format that can be interpreted by the etching system to be used, according to a proper calibration function. Surfaces are then physically realized on a suitable substrate.

4.2.3 Generation of Normally Distributed Random Rough Surfaces

Based on the Central Limit Theorem and the arguments given in chapter 3, randomly rough surfaces whose heights are normally distributed are to be generated. It is well known that if a distribution follows the Gaussian (normal) behavior, then its probability distribution function is:

$$P(x) = \frac{1}{\sigma\sqrt{2\pi}} e^{-\frac{(x-\mu)^2}{2\sigma^2}} \tag{4.1}$$

where:

σ = standard deviation;

μ = mean of the distribution;

Commonly equation (4.1) is normalized by making the following change of variable:

$$\chi = \frac{x - \mu}{\sigma} \tag{4.2}$$

Carrying out this change of variables, one gets the normalized version of equation 4.1:

$$P(x)dx = \frac{1}{\sqrt{2\pi}} e^{-\frac{\chi^2}{2}} d\chi \tag{4.3}$$

Thus, the integral of the left hand side of equation (4.3), which is the probability of a raw variable x, is equal to the probability of a normalized variable χ with mean zero and standard deviation equals to unity.

Let the depth of the surface be a function of x and y, according to the coordinate system shown in figure 23, such that:

$$z(x, y) = \sigma \cdot random(x, y) \tag{4.4}$$

where:

σ = (prescribed) standard deviation;

random(x,y) = a random value at each point on the x-y plane.

Notice that z is a random (normally distributed) variable with mean zero and standard deviation, σ. Assuming isotropy in the x-y plane, then we defined the Gaussian filter g as:

$$g(x, y, ACL) = e^{-\frac{r^2}{ACL^2}} \tag{4.5}$$

where:

$r = \sqrt{x^2 + y^2}$, and

ACL = autocorrelation length.

ACL is defined [105] as the distance from a point beyond which there is no further correlation of a physical property associated with that point. Values for a given property at

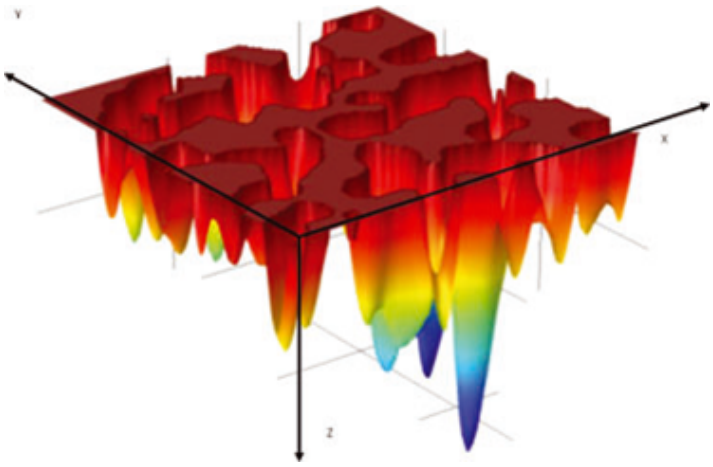

Fig. 23. A typical surface produced in the present study, in a Cartesian coordinate system.

distances beyond the correlation length can be considered purely random. In our case, the relevant physical property is height.

We now apply the so-called Direct Convolution Method [106]which leads to the following array:

$$F_{surface} = \frac{2}{\sqrt{\pi} \cdot N \cdot ACL} L \cdot \frac{1}{N} \sum_{k=0}^{N-1} [DFT(z) \cdot DFT(g)] e^{\frac{i2\pi kn}{N}} \tag{4.6}$$

where:

N = number of grids along each axis;

ACL = auto correlation length;

L = (in this application) same as N;

DFT = Discrete Fourier Transforms, such that in equation (4.6), the two respective expressions can be written as:

$$DFT(z) = \sum_{k=0}^{N} z(n) \cdot e^{-\frac{i2\pi kn}{N}} \tag{4.7}$$

and similarly,

$$DFT(g) = \sum_{k=0}^{N} g(n) \cdot e^{-\frac{i2\pi kn}{N}} \tag{4.8}$$

Therefore, $F_{surface}$ is a 2-D array whose entries represent the heights (or depths) of the

surface, and the respective indexes are the other two corresponding coordinates, as depicted in figure 23.

4.2.4 Surface Damage Growth

Although the technique developed can be used to model nonlinear growth of damage [79], however for the present work, linear degradation was assumed. This assumption can be made since, at the end, what is important is the level of roughness attained and not how the surface grew to that level. In order to model degradation growth, a process called herein "truncation" is used. Surfaces obtained using (4.6) were truncated and replaced back by taking the average location and only including values below that average. D_i stands for complete truncation and no replacement; D_1, D_2, D_3 (and so on) represent, D_1, D_2, D_3 points of replacement of surface after truncation, respectively. A simple pseudo algorithm showing that, follows:

Begin loop;

For $i = 0$ until *imax* increased by *step*;

$F_{surface}(i) = F_{surface} + D_i$;

$Surface(i) = (F_{surface}(i) > 0) \cdot F_{surface}(i)$;

count;

end loop;

Let D_{imax}, for instance, equal to 45 and $step = 5$, then $count = 10$. So for a given ACL in equation (4.6), 10 distinct levels of degradation are produced. One can always increase the levels of degradation but this would be impractical if the resolution of the etching system is not high enough or if the substrate is not appropriate (i.e., if the intrinsic roughness of the substrate is not low enough). Then these D_i are related to the roughness of the respective surfaces. Root-mean-square (RMS) roughness, being a more measurable value, is the parameter used in substitution of D. Figure 24 shows a set of typical surfaces developed

using the technique in discussion, at various levels of roughness. The plots are in gray scale: the darker the spot the deeper the pit. Surfaces in the same row have the same ACL but the roughness increases as one moves to the right, and ACL increases as one moves downwards. Also, figure 25 shows 3-D plots of typical surfaces, in those plots more red means flatter and more blue means deeper. The various features are obtained by varying ACL and level of degradation.

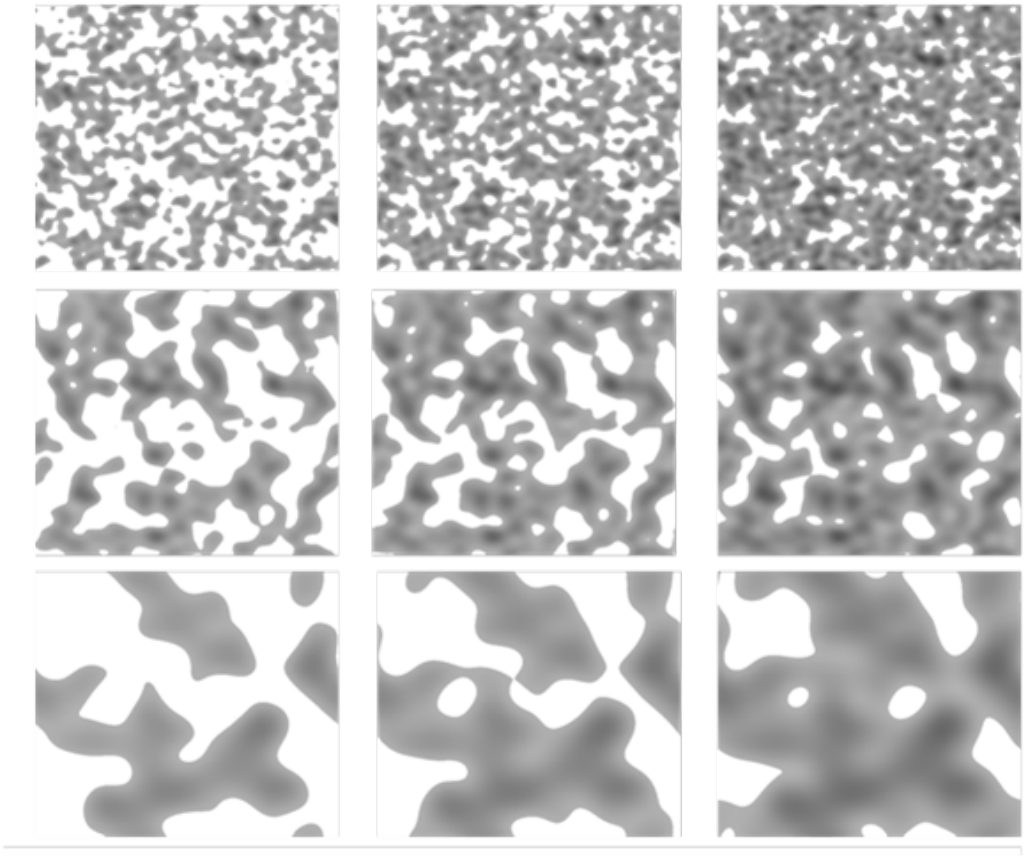

Fig. 24. Surfaces in gray-scale at various ACL and roughnesses. Surfaces in a row have the same ACL but increase in roughness to the right. ACL increases from top to bottom. The darker the spot the deeper the pit.

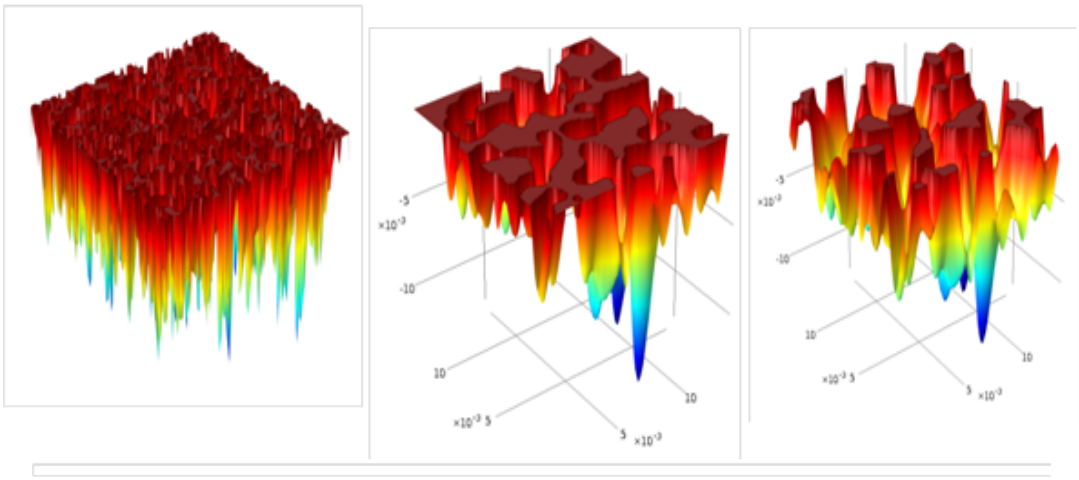

Fig. 25. Typical surfaces produced with the technique in discussion. Different features result from varying ACL and the level of degradation (or roughness). All surfaces correspond to relative high level of roughness. The ACL for these surfaces are (left) small, (center) medium, (right) high.

4.2.5 Realization of the Surfaces Using CO_2 Laser System and PMMA

Next, the random surfaces were 3-D engraved using a CO_2–laser machine of the type Mini Epilog 30 watt (by Epilog Laser), with a resolution of 9 microns. This spot size resolution limited the ACL used to a minimum of 10 microns. The laser beam was passed on the PMMA surface using 3-D engraver mode which adjusts depth per pass (D_p) by varying power (p) at a given speed (v), according the following relationship [107]:

$$D_p = \frac{C}{\rho W}\left(\frac{\alpha p}{v} - \frac{Q_{th}}{W}\right) \tag{4.9}$$

where:

C = constant of proportionality;

ρ = density;

W =width of laser beam;

α = absorptance;

Q_{th} = threshold heat.

Combining the material properties and constants into two parameters, we can write equation (4.9) as:

$$D_p = m\frac{p}{v} + b \tag{4.10a}$$

$$m = \frac{C\alpha}{\rho W} \tag{4.10b}$$

$$b = \frac{CQ_{th}}{\rho W^2} \tag{4.10c}$$

Figure 26 shows two pictures of actual replicates of surfaces etched on PMMA. The ablated dimensions are 12.7 mm by 12.7 mm. The thickness of the specimen was 3 mm. The maximum ablation depth was around 50 micrometers.

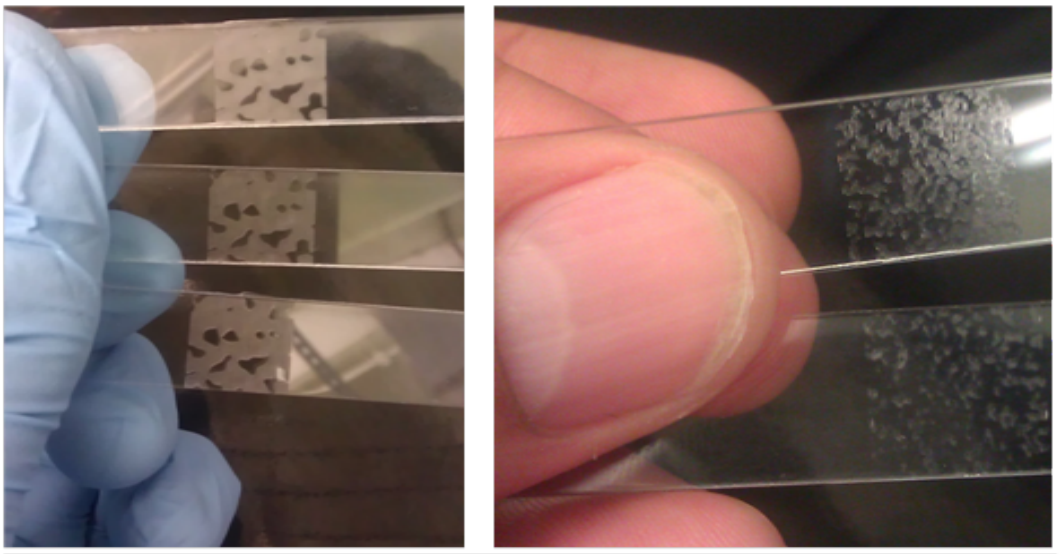

Fig. 26. Samples of two sets of replicates of specimens produced with the described technique. Unablated specimens were laser-cut from commercially available sheets of PMMA.

4.2.6 Characterization of Realized Surfaces

A benchtop scanning electron microscope(SEM) model TM3030 (by Hitachi) was used to investigate the details and micro resolution of the laser on the acrylic beams, see figure 27. Shown in figure 28 is a micrograph of the smallest features obtained with this CO_2 system. Note the wavelength of about 10 micrometers etched. Also note the tiny

Fig. 27. Benchtop Scanning Electron Microscope, model TM3030 (by Hitachi) used to produce micrographs of ablated surfaces. Equipment located in the Wright Center Laboratory at the Virginia Commonwealth University.

circular shaped features (defects) produced by sparks which apparently would be non negligible if ACL was below 10 micrometers. One can easily notice that the largest defects diameters are never bigger than distance between two adjacent peaks, in figure 28. In fact, the average diameter of these defects was around 5 micrometers, and the maximum diameter less than 10 micrometers. However, the amplitudes of these wave-like features are about 1-2 μm, making them negligible if compared to the average pit depth considered and studied here. One would expect different defect sizes for different power, speed, and frequency configuration. Therefore, for smaller roughness levels, lower values of ACL are limited by the resolution of the etching system to be used. If smaller RMS and ACL are

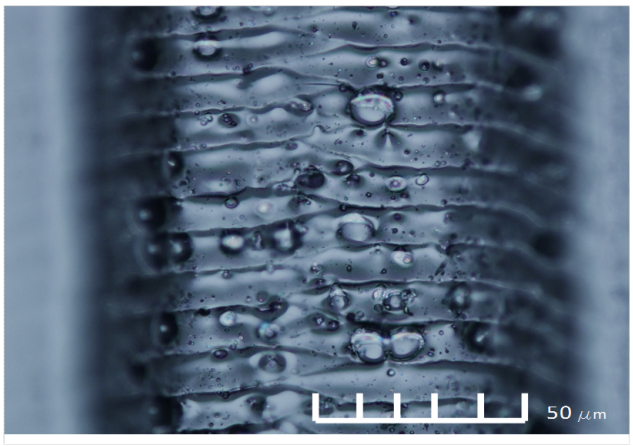

Fig. 28. Micrograph of ablated feature on PMMA using a miniEpilog CO_2 laser system (by Epilog). Note that sparks cause negligible bubble-like damage on the surface. Amplitudes of wave-like features, $\approx 1 - 2\mu$m, are negligible compared to average pit size in actual surfaces studied. Laser equipment located in the machine shop of the School of Engineering at the Virginia Commonwealth University.

desired, other reported techniques could be incorporated. For example, the immersion of a PMMA sample sheet in a water bath with a uniform temperature of about 80 °C has be shown to reduce the amount of sparking bubbles, and hence reduce drastically the surface roughness created due to laser cutting by up to one order of magnitude [108]. True, there are high resolution lasers that could simply improve the roughness considerably, as well—although adding to the research budget. A limitation, however, would be the base material used, since other types of polymers result in rougher cut or ablated surfaces than with the use of poly methyl methacrylate.

Next, an Ambios XP-1 stylus profiler 29 was used to compare the depth of ablation. Figure 30 shows a typical profile observed during the comparison process. Average of actual depth values were compared to those predicted by the respective surface arrays given by eqn. (4.6), and the difference is visually shown in figure 30. The margin of error was found to be consistently below 5%.

A nanoindenter Ubi 1 (by Hysitron)was also used (see figure 31) to investigate me-

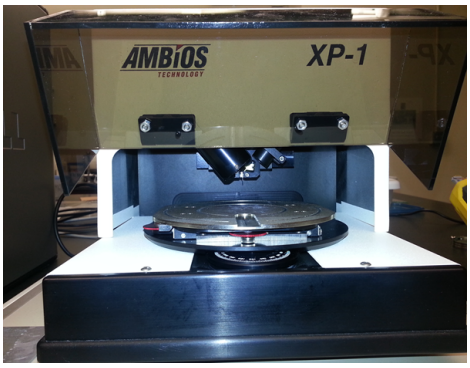

Fig. 29. Ambios XP-1 stylus profiler used to characterize profiles of the surfaces. Profilometer located in the Department of Mechanical and Nuclear Engineering at the Virginia Commonwealth University.

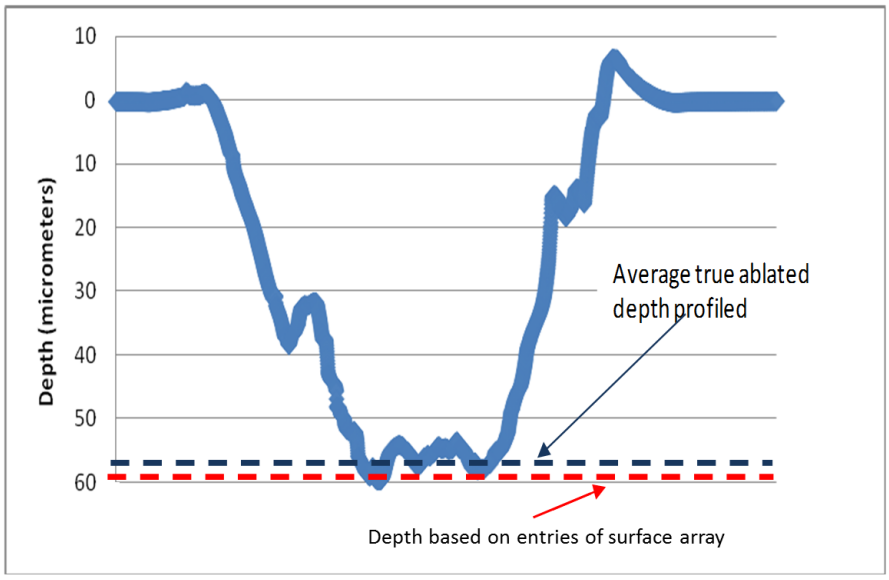

Fig. 30. Typical plot comparing profile measured with stylus profiler against that predicted by digital model. The x-axis represents the scanned distance.

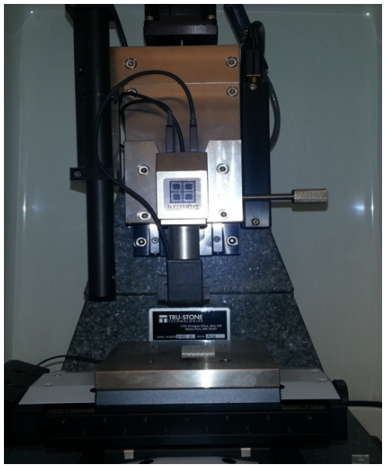

Fig. 31. Nanoindenter Ubi 1, by Hysitron, used to characterize surface's hardness and reduced modulus. Equipment located in the east building of the Department of Mechanical and Nuclear Engineering at the Virginia Commonwealth University.

chanical changes near the surface, due to chemical reactions or physical insertions of laser ablated regions. The hardness for ablated surfaces resulted within reasonable similarity (2-5%) to that of non ablated surfaces. Other characterization techniques like optical profilers could be used, as well, depending on the degree of reflectance of the base material to be used.

4.2.7 Other Applications of this Technique

This technique complements the use of accelerated weathering chambers by offering more controllability of the created surfaces and hence allowing the repeatability of them. Among the benefits of producing in-lab repeatable random rough surfaces, is the ability to carry out multiple (especially destructive) testing on replicates and hence allowing robust statistical analyses. The extension of this technique to the study of several coating materials is obvious and could only be limited by the type of etching process to be implemented, which in turn would depend on the material to be etched.

In the forensic sciences, this technique can find direct applications, as well. Criminolo-

gists, for example, reckon crucial the safeguarding of evidence material for multi-testing purposes. A common practice of that investigative field consists of obtaining 3-D laser scans of crime scene surfaces and their respective conversion to digital format[96]. Our technique would represent a much less costly alternative than modern 3-D printing, for which there is still, to present time, limited types of based materials that can be used. Furthermore, the study of fingerprints as evidence finds complications when they are left on rough surfaces. Facilitation for the investigation of new methods to trace back fingerprints could be accomplished by using replicates of rough surfaces on proper base materials. Investigation of contact angle on random rough surfaces is an explicit example of a fun-

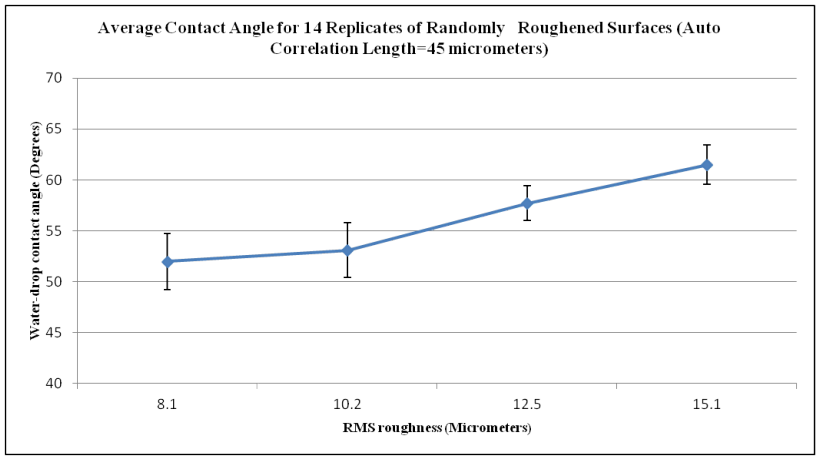

Fig. 32. Plot of contact angle vs. RMS roughness for replicates obtained with the developed technique. This shows an example of the usefulness of producing highly controlled replicates of random rough surfaces. Contact angles were measured with a water–drop goniometer.

damental research for which the generation of surfaces with controlled topography can be applied. Figure 32 shows a plot of water-drop contact angle versus roughness corresponding to 14 replicated specimens developed using the proposed technique. Contact angle measurements are nondestructive, but the often use of multiple liquids—e.g. methylene iodide, hexane, and water—is common. Each chemical alters the subsequent contact angle

measurement, even for repeated use of the same liquid. Nominally identical replicates allow the generation of standard deviation bars that quantify the impacts of the experimental setup, thus removing the effects of extra chemical impacts on the surfaces caused by residual liquid nanofilms from previous measurements. The study of surface wettability via contact angle offers promise to gain further understanding of surface degradation in coatings, incorporating both ACL and roughness into service lifetime prediction of corrosion protective coatings.

In the field of implant research, it has been widely accepted that surface roughness plays a key role in the differentiation of bone-forming cells [99]. Studies on this field have depended on the use of nonidentical specimens of surface roughness. Also, so far there has not been any study that correlates ACL to bone-formation markers. A technique such as this would provide researchers in the implant research field means to carry out statistical studies and the addition of more geometrical parameters.

Other applications include the development of random controlled surfaces for tribological studies combined with statistical analysis. For example, in studying the coefficient of friction as a function of wear (undesired loss of material from a solid surface), one could experiment with nominally exact replicates at the same stage of wear, by using the present technique, thus allowing statistical study of the behavior.

4.3 PART II: Methodology for the Remainder of the Work

After the specimens were produced using the foregoing technique, the following steps were carried out:

- Flexural and failure properties were determined from three-point bending tests based on ASTM D790-10 standards, procedure B, using an Insight 30 MTS® machine (by MTS Systems Corporation). Identical replicates of the surface topography laser etched on D790 samples were used to generate statistical distribution of stress/strain

curves and stress, strain, and energy to fracture measurements. Temperature variation and control inside an environmental chamber allow the study of brittle and quasi-ductile regions, as to simulate a variety of materials.

- Statistical analysis was performed using IBM SPSS® software (by IBM). Bivariate, multivariable, and partial correlations were carried out using linear correlation models.

- The generated surface topology template was imported into the finite element code, COMSOL®, in order to compare our experimental and analytical results with finite element analysis.

- The perturbation method mentioned in chapter 3 was utilized in order to derive the stress concentration factor due to random discontinuities.

4.3.1 ASTM D790 Procedure B, Flexural Tests

Flexural tests of the type ASTM D790, procedure B, were carried out using an Insight 30 MTS machine, see figure 33. Specimens produced with the technique described in the first part of this chapter were bent to fracture at a deflection rate of 0.2 in/min. This rate was kept constant throughout the experimental work. The dimensions of the specimens are shown in figure 34. Samples with dimensions of 3 mm x 12.7 mm x 127 mm were cut from acrylic sheets using a CO_2 laser system. Power, speed and frequency were set in laser so that smoothness was guaranteed during cutting. Set of samples with different roughness were tested. The autocorrelation length and depth of ablation (related to roughness) were used as characteristic parameters of these different surfaces. The engraved areas were located at the center of the sample and had dimensions of 12.7 mm x 12.7 mm, having patterns and depths based on the digital surfaces produced by equation (4.6). The span length was 3 inches and cylindrical noses were used for both supporting points and application of

Fig. 33. Insight 30 MTS machine used to carry out flexural tests. Equipment located in the east building of the Department of Mechanical and Nuclear Engineering at the Virginia Commonwealth University.

load. Flexural stress vs. strain data was obtained for a large number of specimens. A least

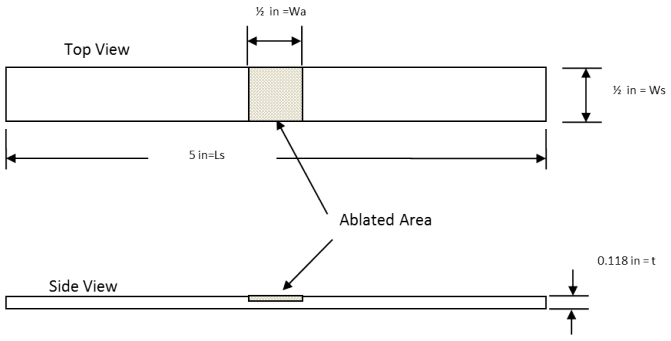

Fig. 34. D790 specimens with ablated surfaces in the central location

14 replicates for each type of surface were tested, but the majority of the sets of replicates consisted of 24 specimens. Each type of surface was characterized by its ACL and depth ablation, which in turn is a function of surface roughness. Three distinct ACL were considered: 10, 45 and 90 micrometers. Additionally, four levels of degradation were considered

per ACL, namely, D=0, 15, 30, 45; and for each D, there corresponds a respective RMS roughness depending on ACL used.

4.3.2 Flexural Energy at Fracture

Flexural energy at fracture (w_{fb}) is defined as the area under the flexural stress-strain curve, or:

$$w_{fb} = \int_0^{\epsilon_{fb}} \sigma_f d\epsilon_f \tag{4.11}$$

where:

ϵ_{fb} = flexural strain at fracture (b=break);

σ_f = flexural stress;

ϵ_f = flexural strain.

It provides a measurement of how much energy the surface of the specimen absorbs before failing by fracture. For brittle or quasi-brittle materials (our case), this value gives a good estimate of the tensional elastic energy at fracture of a slightly degraded surface. Since our measurements provided a large number of data points then equation (4.11) can be very well approximated by:

$$w_{fb} = \sum_{i=2}^{N} \sigma_{f_i}(\epsilon_{f_i} - \epsilon_{f_{i-1}}) \tag{4.12}$$

4.3.3 Statistical Analysis

Statistical analysis was performed using IBM SPSS software version 19. Bivariate, multi-variable, and partial correlations were carried out using linear and nonlinear correlation models. Previously[18], several surface geometrical parameters had been considered such as average roughness, standard deviation, variance, kurtosis, root-mean-square

roughness, skewness, slope, curvature, maximum pit depth, and autocorrelation length. Safety envelops for fracture location probability distribution and fracture toughness as a function of topological parameters were directly derived from this analysis[18]. Bivariate correlations were used to find Pearsons product-moment correlation coefficient. The Pearson Coefficient is a dimensionless index that can measure linear dependence between two variables[109], in order words it is invariant to linear transformations of either compared variable. Pearson initially formulated a mathematical relationship for this rather important measure in 1895, as the ratio of the inner product of the variances (also called covariance) into the product of the standard deviations. The foregoing ratio, called, Pearson's correlation coefficient, p, gives a measure of how strong the two given variables a linearly correlated. If $p = 1$ for two variables A and B, it is said that A and B and perfectly correlated in a positive manner: the higher A the higher B; although it does not establish direct proportionality strictly speaking. Conversely, if $p = -1$, then A and B are still perfect correlated but in a negative manner; that is, the higher A the smaller B, or vice-versa. Now, if $p = 0$ then A and B are not correlated, at all. In that case, a scatter plot of, say, A vs. B would be completely scattered. As p goes from 0 to 1, positive correlation increases, and as it goes from 0 to -1, negative correlation increases. Empirical relationships were derived by coupling the highest correlated parameters. The procedures described above were used to corroborate the derived models based on surface topology (auto correlation length and level of surface degradation) and temperature. The results of the experiments were compared to the analytical model derived in chapter 6, and to some cases analyzed via FEA in chapter 7.

4.3.4 Topographical Parameters and Correlation

Several topographical parameters were studied in order to explore which best correlate with the markers of mechanical failure. The parameters considered in this study have been

included in standardized literature for many years [110–113]. They following parameters can be applied to both surfaces and profiles:

$$m = \frac{1}{N}\sum_{i=1}^{N} Z_i \tag{4.13a}$$

$$R_a = \frac{1}{N}\sum_{i=1}^{N} |Z_i - m| \tag{4.13b}$$

$$V = s^2 = \frac{1}{N}\sum_{i=1}^{N} (Z_i - m)^2 \tag{4.13c}$$

$$Sk = \frac{1}{s^3 N}\sum_{i=1}^{N} (Z_i - m)^3 \tag{4.13d}$$

$$RMS^2 = R_q^2 = \frac{1}{N}\sum_{i=1}^{N} (Z_i - m)^2 + m^2 \tag{4.13e}$$

$$K = \frac{1}{s^4 N}\sum_{i=1}^{N} (Z_i - m)^4 \tag{4.13f}$$

$$Z'(x) = \frac{\partial Z}{\partial x} = \frac{1}{N-1}\sum_{i=1}^{N-1} \frac{Z_{i+1} - Z_i}{\Delta x} \tag{4.13g}$$

$$-Z''(x) = -\frac{\partial^2 Z}{\partial x^2} = \frac{1}{N-2}\sum_{i=2}^{N-1} \frac{2Z_i - Z_{i+1} - Z_{i-1}}{(\Delta x)^2} \tag{4.13h}$$

where:

m = arithmetic mean of the surface height as measured from a flat surface;

R_a = Average roughness around m;

s = Standard deviation of the surface peaks and valleys around m;

V = variance of the heights;

Sk = Skewness of the surface;

$RMS = R_q$ = root-mean-square roughness of surface;

K = Kurtosis of the surface;

$Z'(x)$= slope of surface in the x direction. (So, $Z'(y)$ would be the slope in the y direction);

Z"(x) = curvature of the surface in the x direction.(So, Z"(y) would be the curvature in the y direction.)

Besides the aforementioned parameters, the autocorrelation length (ACL) was pescribed in the generation of the surfaces (see chapter 4), and therefore must be included in the list of surface parameters.

In order to examine correlation between topographical variables and markers of failure of material, scatter plots were obtained and the respective Pearson's correlation coefficient computed. Scatter plots provide a visual way to observe the correlation behavior between any two given parameters. The two parameters considered were RMS roughness and ACL. Also, plots showing behavior of p with level of degradation (RMS roughness) were developed.

The markers of failure considered were stress, strain and energy at fracture, and the fracture location density (FLD). FLD provides the probability distribution of where fracture takes place on the roughened surface along the axis of loading.

4.3.5 Division of Ablated Area into Profiles for Fracture location Density Measurements

In order to study how stress concentrates along profiles which are perpendicular to the axis of loading, the ablated area was divided into 20 equally-spaced profiles (or lines). The two lines that coincided with the flat-to-rough interfaces were excluded from consideration based on Saint-Vernant principle [39] which motivates the studies of effects or mechanisms away from the boundaries of the region of interest.

Figure 35 shows the aforementioned state of affairs. For each specimen tested until fracture, the fracture location distance, x_i, was measured and recorded. Fracture location density for each location i (FLD_i)—which can also be understood as a theoretical probability—is simply defined as the ratio of the number of specimens fractured at location i divided by the total number of fractured specimens. In order to correlate FLD_i with appropriate statistical parameters, the RMS roughness and ACL of each individual profile i were obtained, as well. Other statistical parameters were discarded based on previous studies [18]. All the results from the experimental work are presented in chapter 5.

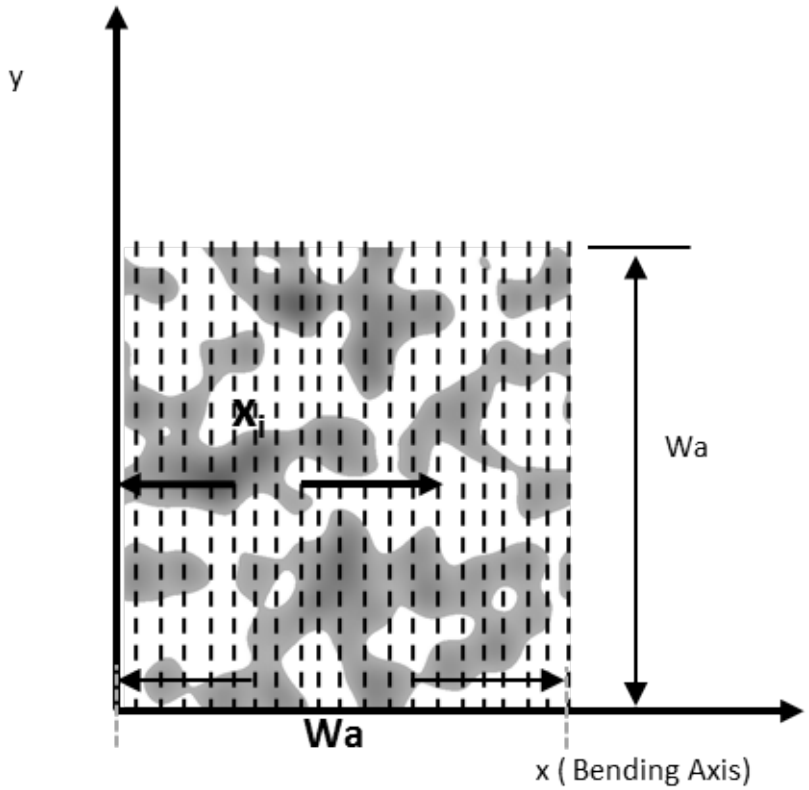

Fig. 35. Division of ablated area into 20 equally-spaced lines or profiles.

CHAPTER 5

EXPERIMENTAL RESULTS

This chapter is solely dedicated to results and discussion of experimental work[1].

5.1 How to Read Scatter Plots

The scatter plots of fracture location density (FLD) versus parameters of profiles were developed. These plots are intended to show the probability of fracture at certain profiles depending on the characteristics of those profiles. Each plot contains 18 data points which indicate the 18 possible locations where the surface can break at. So since there are locations where the surface never breaks, these corresponding points lie on the x-axis. Additionally, the sum of the probabilities add up to 1 for each plot, as it should. The number of specimens for each plot varies, as indicated; moreover, this number was increased for more stochastic behavior of FLD and depending on how many specimens fractured at the flat-to-rough interface.

5.2 Flexural Properties at Fracture

Flexural stress and strain at fracture were measured from ASTM D790 tests on replicates of random rough surfaces ablated on PMMA beams. The energy at fracture was calculated as described in chapter 4. Characteristic values of the results are shown in figures 36 through 40. These sets of values are but a small sample of the hundreds of tables

[1]For analytical results see chapter 6 and for the finite element analysis results see chapter 7

produced.

Stress at fracture		strain fracture		Energy at fracture	
flex stress (Mpa)	Stress ratio	flex strain (mm/mm)	strain ratio	energy (MJ/m^3)	Energy Ratio
75.48382248	0.99267373	0.02596	0.97465741	1.959560032	0.953524509
88.46665384	1.16340853	0.03403	1.2776422	3.01052023	1.464923134
66.50684615	0.87461918	0.02181	0.81884738	1.450514315	0.705822188
70.69196492	0.9296569	0.02367	0.88868031	1.67327881	0.814219686
74.60129332	0.98106775	0.02508	0.94161817	1.871000436	0.910431292
59.41213905	0.781318	0.0213	0.79969964	1.265478562	0.615783545
79.58620414	1.04662339	0.02747	1.03134973	2.186233028	1.063823889
82.33031826	1.08271072	0.02943	1.10493711	2.422981266	1.179025896
79.11736052	1.04045771	0.02738	1.02797072	2.166233331	1.05409201
84.21258749	1.10746409	0.03022	1.13459733	2.544904394	1.238353851

Fig. 36. Table of a selected group of data points obtained for stress at fracture, strain at fracture, and the calculated, energy at fracture. Energy at fracture is defined as the area under the curve of the stress-strain curve until the point of fracture. This plot correspond to flat specimens. The total number of specimens were 30.

RMS = 9 micrometers		ACL=10			
Stress at fracture		strain fracture		Energy at fracture	
flex stress (Mpa)	Stress ratio	flex strain (mm/mm)	strain ratio	energy (MJ/m^3)	Energy Ratio
69.469	0.91357391	0.022	0.82598085	1.528318	0.743681564
66.397	0.87317461	0.022	0.82598085	1.460734	0.7107951
52.889	0.69553341	0.017	0.63825793	0.899113	0.437509577
64.017	0.84187567	0.021	0.78843627	1.344357	0.654165898
70.822	0.93136697	0.023	0.86352544	1.628906	0.792627819
65.466	0.8609312	0.022	0.82598085	1.440252	0.700828532
70.523	0.92743487	0.023	0.86352544	1.622029	0.789281461
64.951	0.85415854	0.021	0.78843627	1.363971	0.663710096
67.923	0.89324276	0.022	0.82598085	1.494306	0.72713128
67.979	0.8939792	0.022	0.82598085	1.495538	0.727730773
69.957	0.91999151	0.023	0.86352544	1.609011	0.782946885
69.271	0.91097005	0.023	0.86352544	1.593233	0.775269289

Fig. 37. Table of a selected group of data points obtained for stress at fracture, strain at fracture, and, the calculated, energy at fracture. Energy at fracture is defined as the area under the curve of the stress-strain curve until the point of fracture. ACL= 10, RMS= 9 micrometers. The total number of specimens were 24.

RMS= 11 micrometers		ACL=10			
Stress at fracture		strain fracture		Energy at fracture	
flex stress (Mpa)	Stress ratio	flex strain (mm/mm)	strain ratio	energy (MJ/m^3)	Energy Ratio
84.564	1.11208545	0.031	1.16388211	2.621484	1.275617589
78.516	1.03254933	0.027	1.01370377	2.119932	1.031561721
75.247	0.98955932	0.025	0.9386146	1.881175	0.915382248
77.013	1.01278366	0.026	0.97615919	2.002338	0.974340325
76.758	1.0094302	0.026	0.97615919	1.995708	0.971114158
67.807	0.89171726	0.022	0.82598085	1.491754	0.725889474
73.427	0.96562484	0.025	0.9386146	1.835675	0.893241888
64.587	0.84937164	0.021	0.78843627	1.356327	0.659990516
67.519	0.88792983	0.022	0.82598085	1.485418	0.722806368
76.425	1.00505098	0.026	0.97615919	1.98705	0.966901164
70.963	0.93322123	0.023	0.86352544	1.632149	0.794205867
72.922	0.95898368	0.024	0.90107002	1.750128	0.851614604

Fig. 38. Table of a selected group of data points obtained for stress at fracture, strain at fracture, and, the calculated, energy at fracture. Energy at fracture is defined as the area under the curve of the stress-strain curve until the point of fracture. ACL= 10, RMS= 11 micrometers. The total number of specimens were 24.

RMS = 14 micrometers		ACL=10			
Stress at fracture		strain fracture		Energy at fracture	
flex stress (Mpa)	Stress ratio	flex strain (mm/mm)	strain ratio	energy (MJ/m^3)	Energy Ratio
57.756	0.75953843	0.019	0.7133471	1.097364	0.533978777
66.584	0.87563381	0.022	0.82598085	1.464848	0.712796978
63.132	0.8302372	0.021	0.78843627	1.325772	0.645122412
68.512	0.90098858	0.023	0.86352544	1.575776	0.76677469
64.661	0.8503448	0.021	0.78843627	1.357881	0.660746694
47.536	0.62513711	0.015	0.56316876	0.71304	0.346966209
69.81	0.91805834	0.024	0.90107002	1.67544	0.815271325
67.796	0.8915726	0.023	0.86352544	1.559308	0.758761339
59.709	0.78522197	0.02	0.75089168	1.19418	0.581089571
55.527	0.73022526	0.018	0.67580252	0.999486	0.486351212
65.624	0.86300903	0.022	0.82598085	1.443728	0.702519958
65.505	0.86144409	0.022	0.82598085	1.44111	0.701246036

Fig. 39. Table of a selected group of data points obtained for stress at fracture, strain at fracture, and, the calculated, energy at fracture. Energy at fracture is defined as the area under the curve of the stress-strain curve until the point of fracture. ACL= 10, RMS= 14 micrometers. The total number of specimens were 24.

RMS = 16 micrometers		ACL =10			
Stress at fracture		strain fracture		Energy at fracture	
flex stress (Mpa)	Stress ratio	flex strain (mm/mm)	strain ratio	energy (MJ/m^3)	Energy Ratio
63.108	0.82992158	0.021	0.78843627	1.325268	0.644877165
65.539	0.86189121	0.021	0.78843627	1.376319	0.66971865
67.331	0.88545747	0.023	0.86352544	1.548613	0.753557138
64.824	0.85248838	0.021	0.78843627	1.361304	0.662412331
66.405	0.87327982	0.022	0.82598085	1.46091	0.710880742
66.183	0.87036034	0.022	0.82598085	1.456026	0.708504181
67.579	0.88871887	0.022	0.82598085	1.486738	0.723448681
64.786	0.85198865	0.021	0.78843627	1.360506	0.662024023
69.142	0.9092736	0.023	0.86352544	1.590266	0.773825543
65.512	0.86153614	0.022	0.82598085	1.441264	0.701320973
69.012	0.90756399	0.023	0.86352544	1.587276	0.772370605
65.312	0.85890598	0.022	0.82598085	1.436864	0.699179927

Fig. 40. Table of a selected group of data points obtained for stress at fracture, strain at fracture, and, the calculated, energy at fracture. Energy at fracture is defined as the area under the curve of the stress-strain curve until the point of fracture. ACL= 10, RMS= 16 micrometers. The total number of specimens were 24.

5.2.1 Stress at Fracture

Using the result values similar to those contained in figures 36 through 40, plots of flexural stress at fracture for replicates of surfaces at various ACL were obtained and are shown in figures 41, 42, 43, 44, and 45. Each one of these plots were obtained using data from 24 replicates of each kind of surface. The y-axes represent the ratio of stress at fracture for a given surface to the average stress at fracture for flat specimens (we will refer to that ratio as RSF). The x-axes represent the level of degradation via RMS roughness of the surface. Some plots include only the range of degradation at early stage since that is the focus of the present study. Other plots are shown starting at a flat condition (no degradation), that is when RMS=0. A few plots shown do include a further level of degradation—RMS roughness levels higher than those characteristic of early degradation, as understood in the context of the present study. A characteristic ACL is included in each plot. Of course, when flat specimens are included, the ACL does not correspond to them.

Figures 41 and 42 show two plots of RSF vs. RMS starting with a flat surface, for ACL=10. In the plot of figure 41 the x-axis starts with a flat condition, while in figure 42 it only covers early stage of surface degradation. As it can be noticed, in average there is a decrease in the stress required to fracture roughened specimens compared to that of flat specimens; the standard deviations are significantly high and the decrease in stress at fracture seem to range from about 10 to 20 %. Focusing on the plot of figure 42 the relative stress at fracture as the RMS progresses do not seem to change significantly. However, there seems to be a point of relaxation at $RMS \approx 11$ μm where the surface seem to prolong the point of stress where it fractures. In fact, as it can be noticed in the next plots, this relaxation location is related not only to the RMS but also to the ACL.

Figures 43 and 44 show plots of RSF versus RMS roughness for ACL=45.

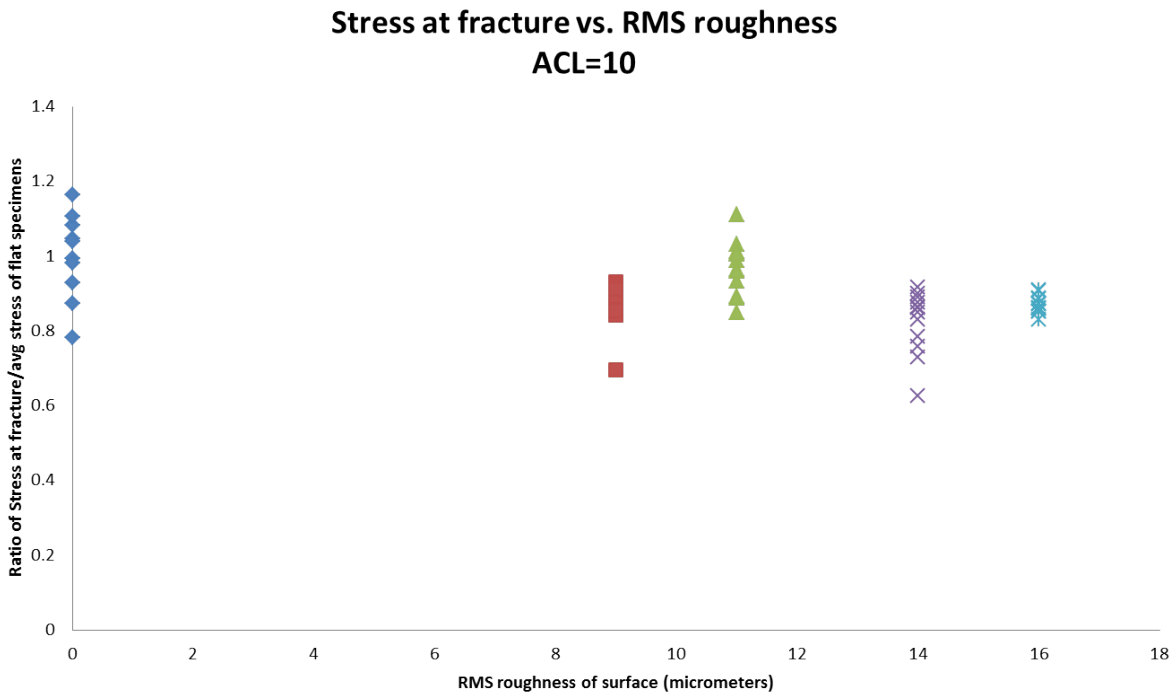

Fig. 41. Flexural stress at fracture versus RMS roughness of surface, starting with a flat surface. RMS = 0 means a flat surface. For each roughness included in this plot there correspond 14 replicates of the exact same surface. ACL = 10.

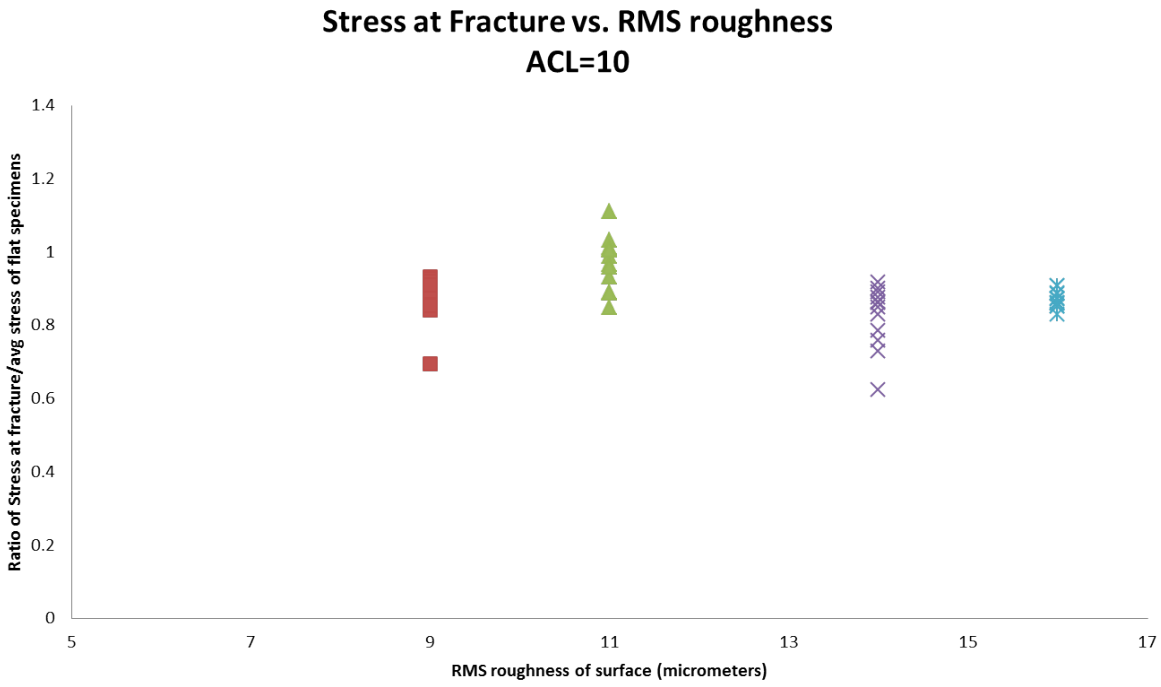

Fig. 42. Flexural stress at fracture versus RMS roughness of surface. For each roughness included in this plot there correspond 14 replicates of the exact same surface. ACL = 10.

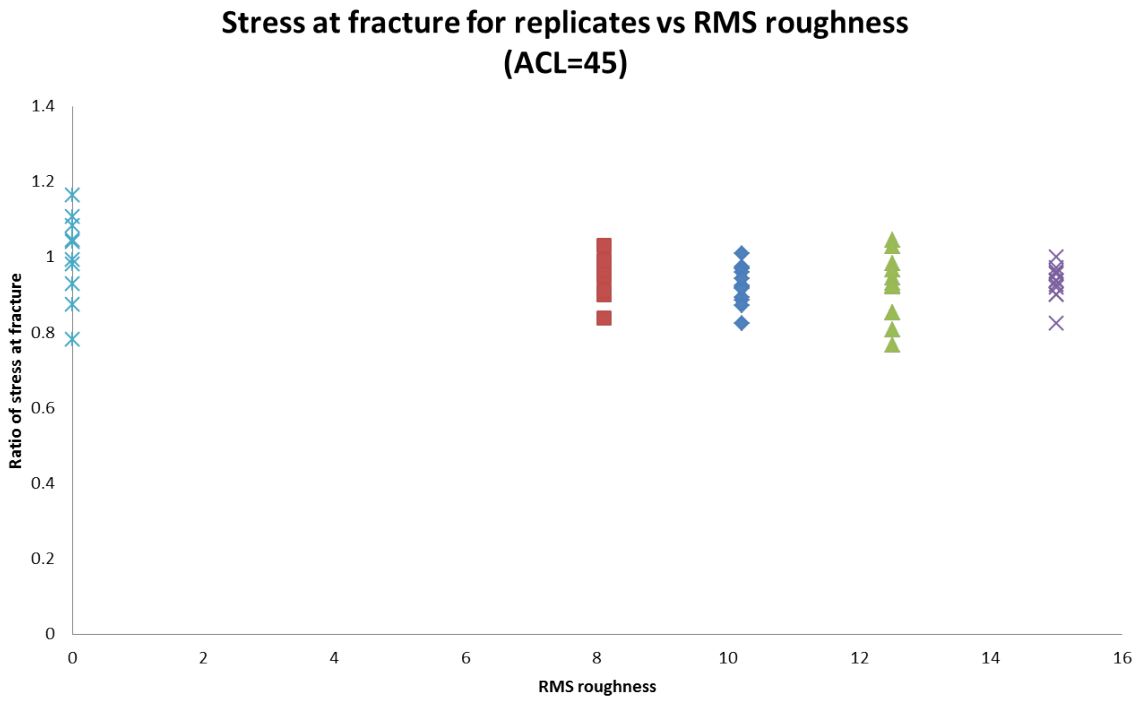

Fig. 43. Flexural stress at fracture versus RMS roughness of surface, starting with a flat surface. RMS = 0 means a flat surface. For each roughness included in this plot there correspond 14 replicates of the exact same surface. ACL = 45.

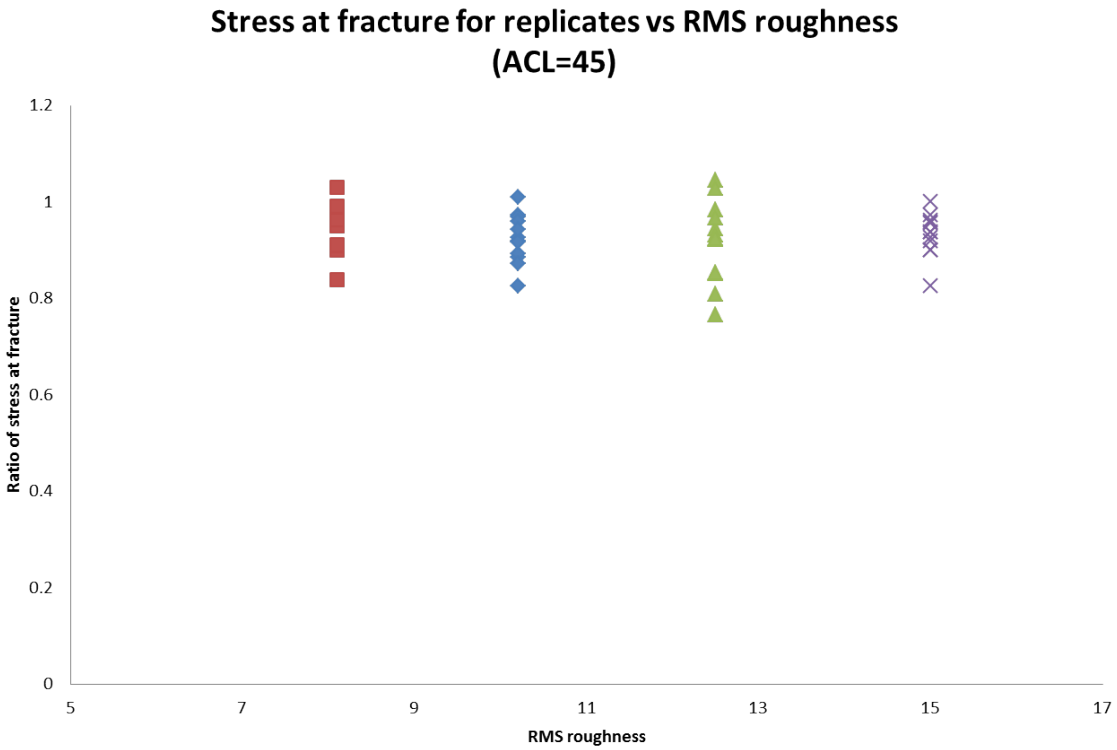

Fig. 44. Flexural stress at fracture versus RMS roughness of surface. For each roughness included in this plot there correspond 14 replicates of the exact same surface. ACL = 45.

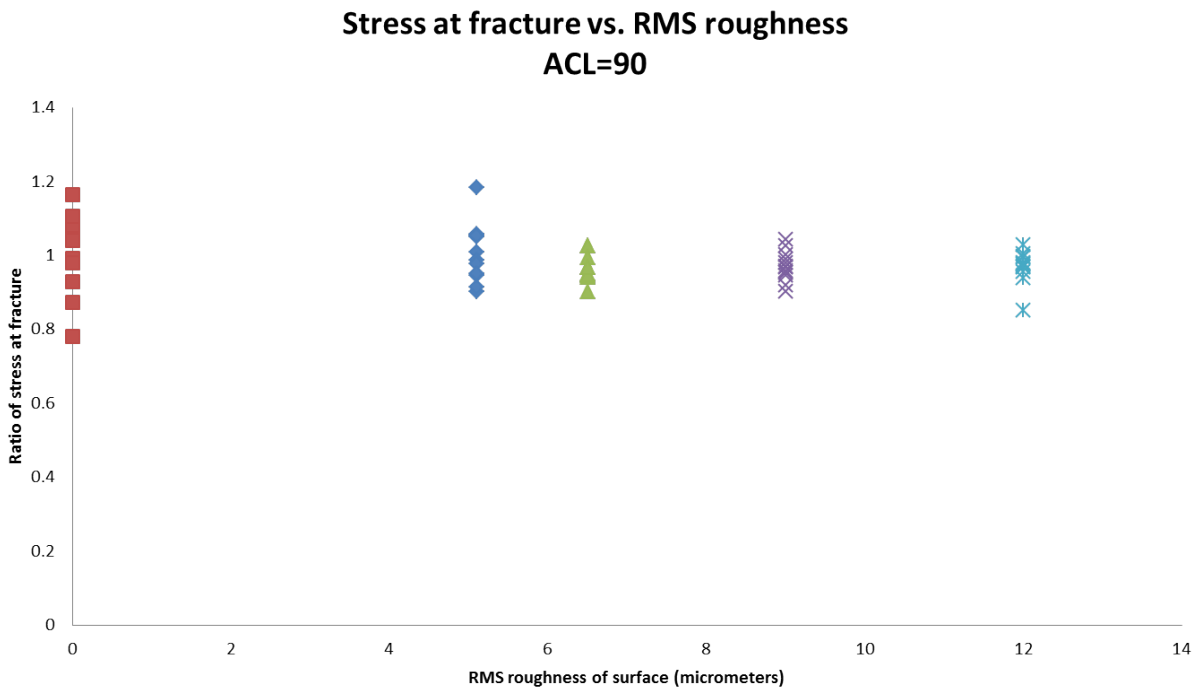

Fig. 45. Flexural stress at fracture versus RMS roughness of surface, starting with a flat surface. RMS = 0 means a flat surface. For each roughness included in this plot there correspond 14 replicates of the exact same surface. ACL = 90.

5.2.2 Strain at Fracture

Following are a set of plots of strain at fracture versus RMS roughness of surface. The y-axes correspond to the ratio of strain at fracture of a roughened specimen to that of a nominally flat one. RMS roughness is expresses in micrometers, as before. The plots correspond to sets of 14 replicates for each surface. More specimens were also tested and showed the same trend. The plots are divided by the ACL of the surface. Some plots only cover the range within the early stage of degradation, and others start with a flat specimen (RMS = 0).

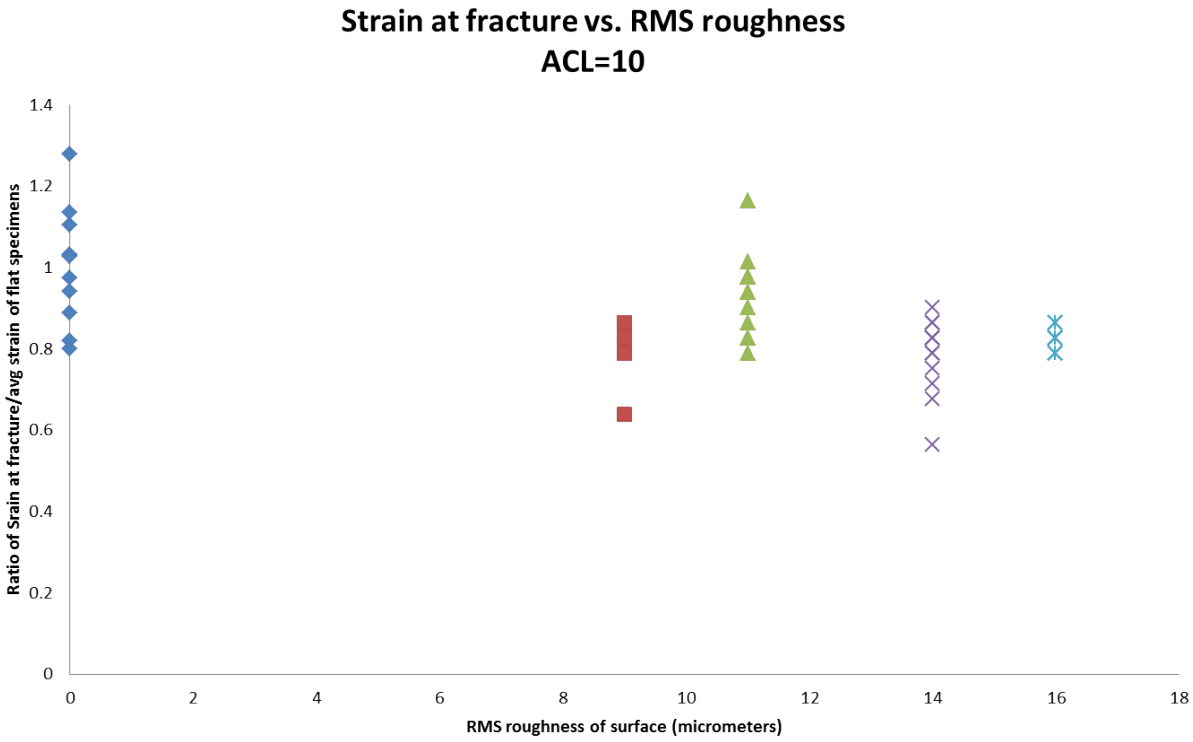

Fig. 46. Flexural strain at fracture versus RMS roughness of surface, starting with a flat surface. RMS = 0 means a flat surface. For each roughness included in this plot there correspond 14 replicates of the exact same surface. ACL = 10.

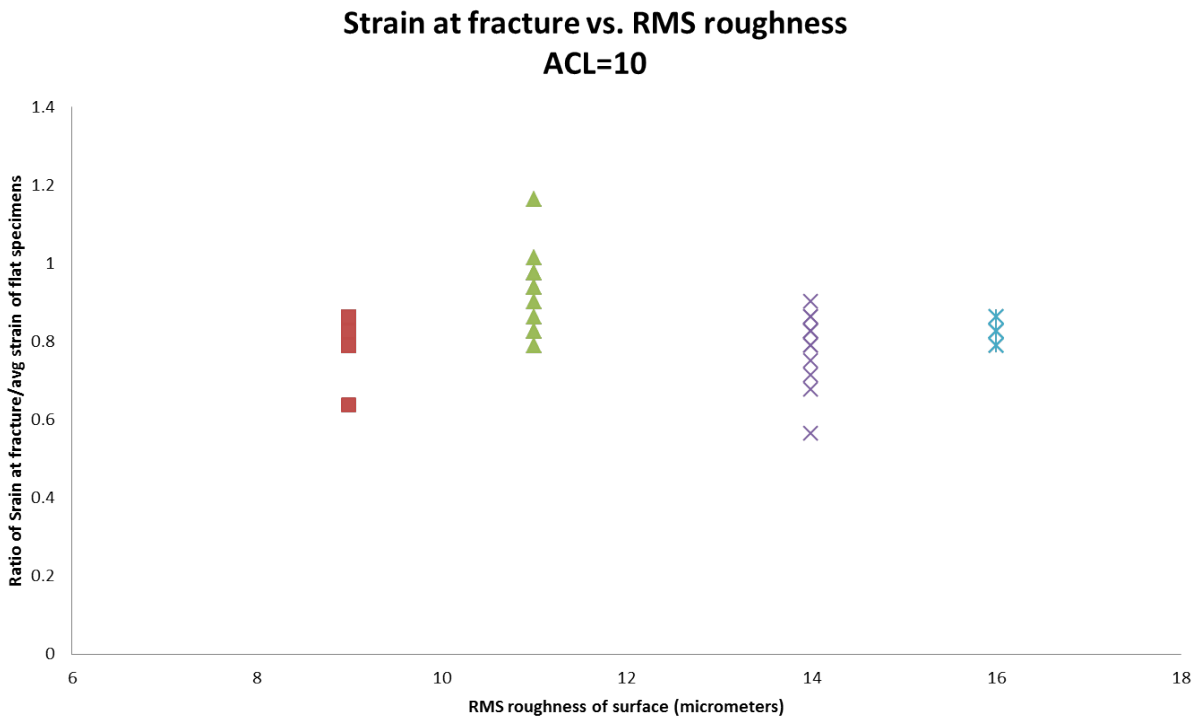

Fig. 47. Flexural strain at fracture versus RMS roughness of surface. For each roughness included in this plot there correspond 14 replicates of the exact same surface. ACL = 10.

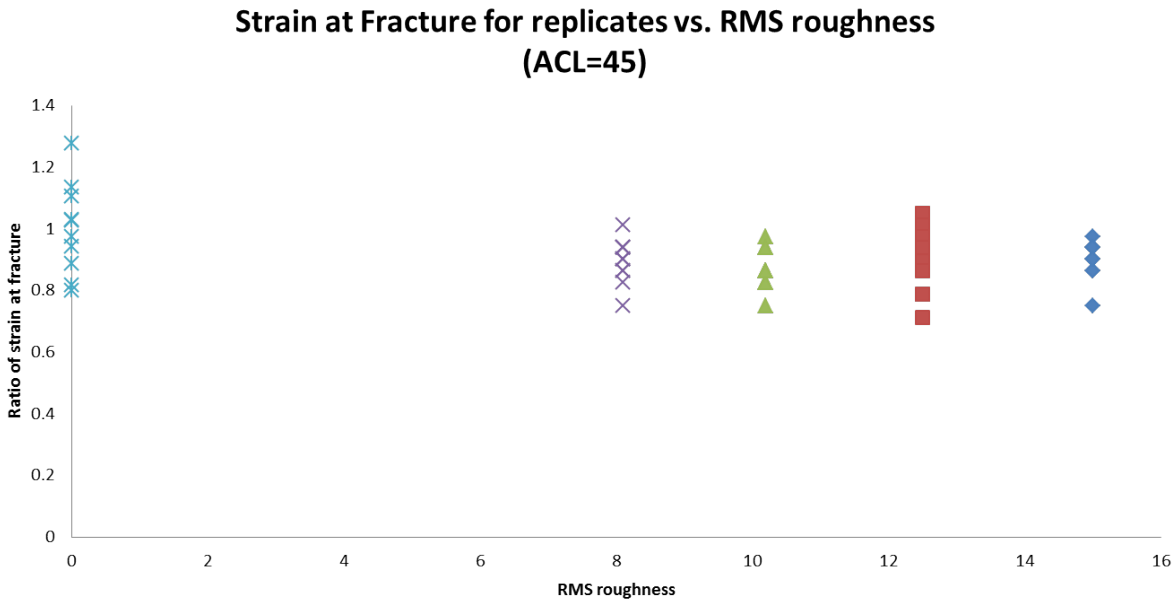

Fig. 48. Flexural strain at fracture versus RMS roughness of surface, starting with a flat surface. RMS = 0 means a flat surface. For each roughness included in this plot there correspond 14 replicates of the exact same surface. ACL = 45.

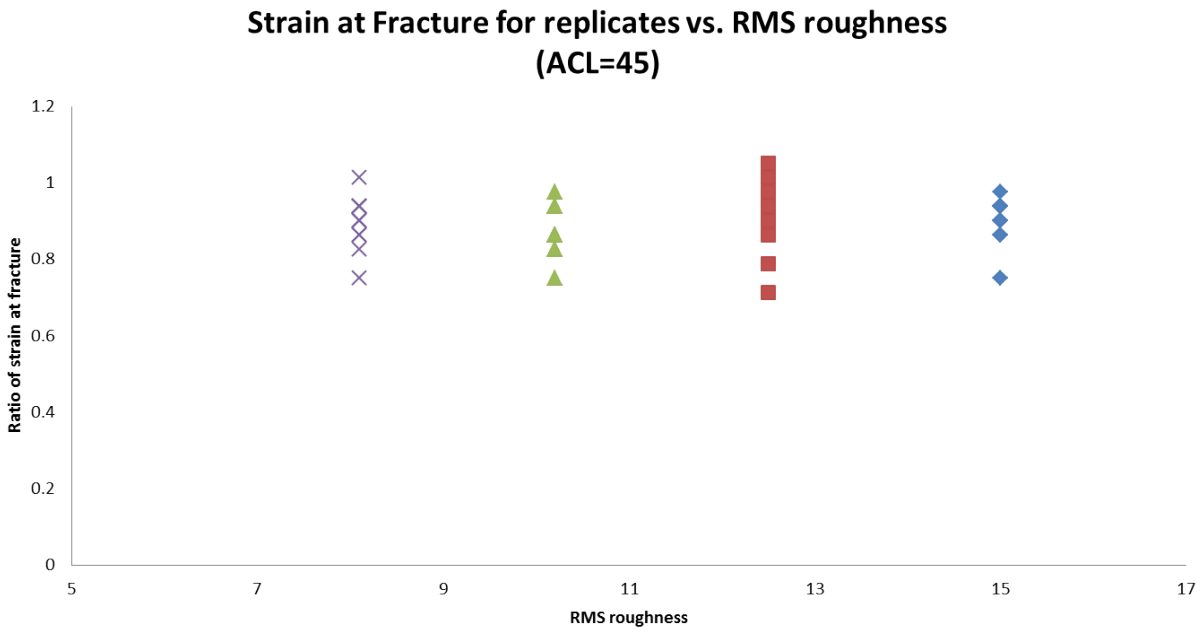

Fig. 49. Flexural strain at fracture versus RMS roughness of surface. For each roughness included in this plot there correspond 14 replicates of the exact same surface. ACL = 45.

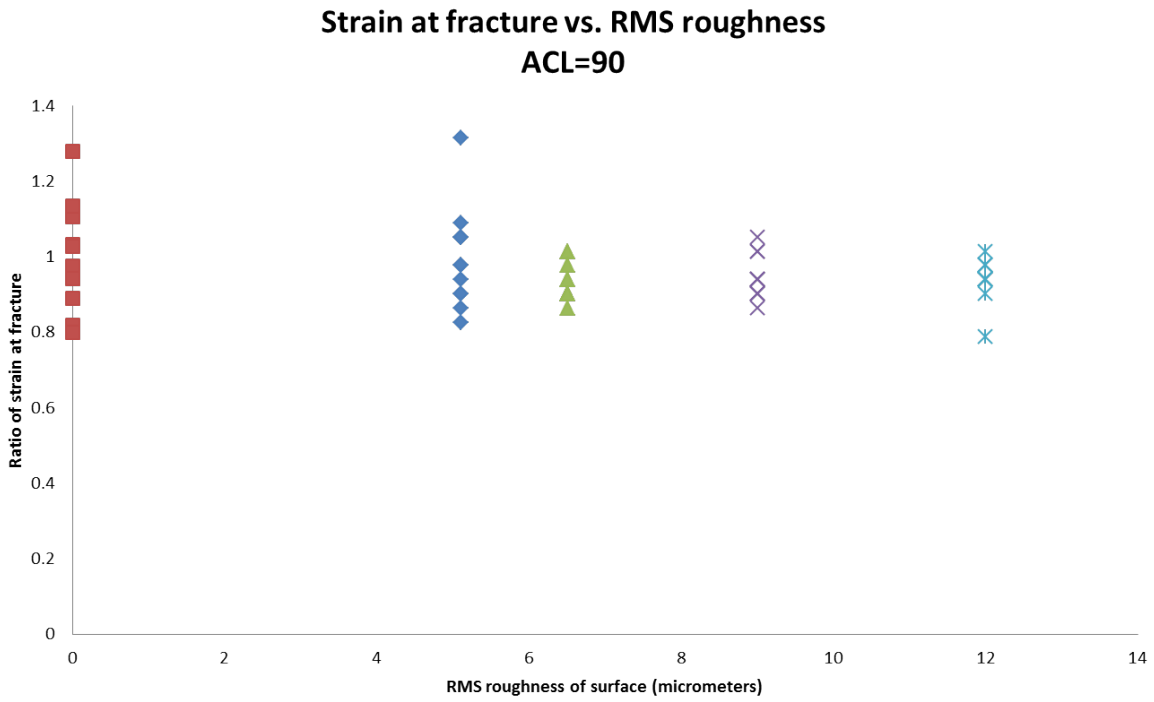

Fig. 50. Flexural strain at fracture versus RMS roughness of surface, starting with a flat surface. RMS = 0 means a flat surface. For each roughness included in this plot there correspond 14 replicates of the exact same surface. ACL = 90.

5.2.3 Energy at Fracture

Following are a set of of plots of energy at fracture versus RMS roughness of surface. The y-axes correspond to the ratio of energy at fracture of a roughened surface to that of a nominally flat one. The x-axes correspond to the RMS roughness in micrometers. The first plot, figure 51, covers the entire range starting from a nominally flat surface, passing through the stage of early degradation, and beyond that stage (about 35 micrometers of RMS roughness). Notice not only that the energy decreases, as expected, but that the process becomes less stochastic since the standard deviation decreases.

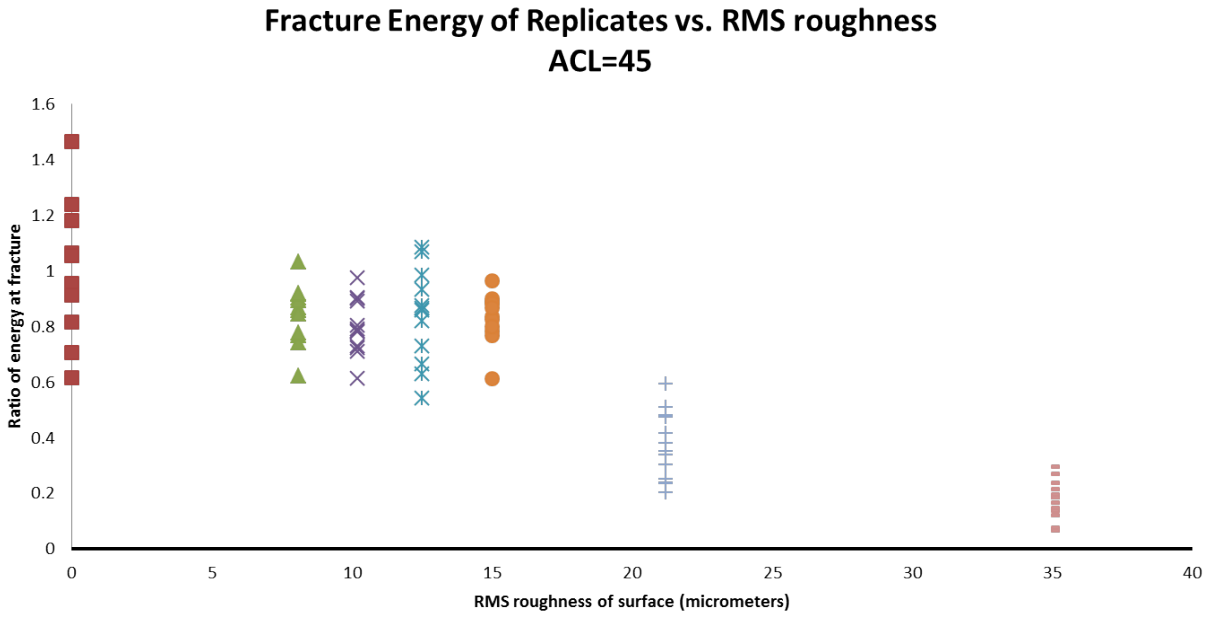

Fig. 51. Energy at fracture versus RMS roughness of surface, starting with a flat surface until a level of degradation well passed the early stage. As expected, energy decreases with degradation level. RMS = 0 means a flat surface. Notice the almost constant behavior of energy at the four points of degradation in the range of 8-15 micrometers. ACL = 45

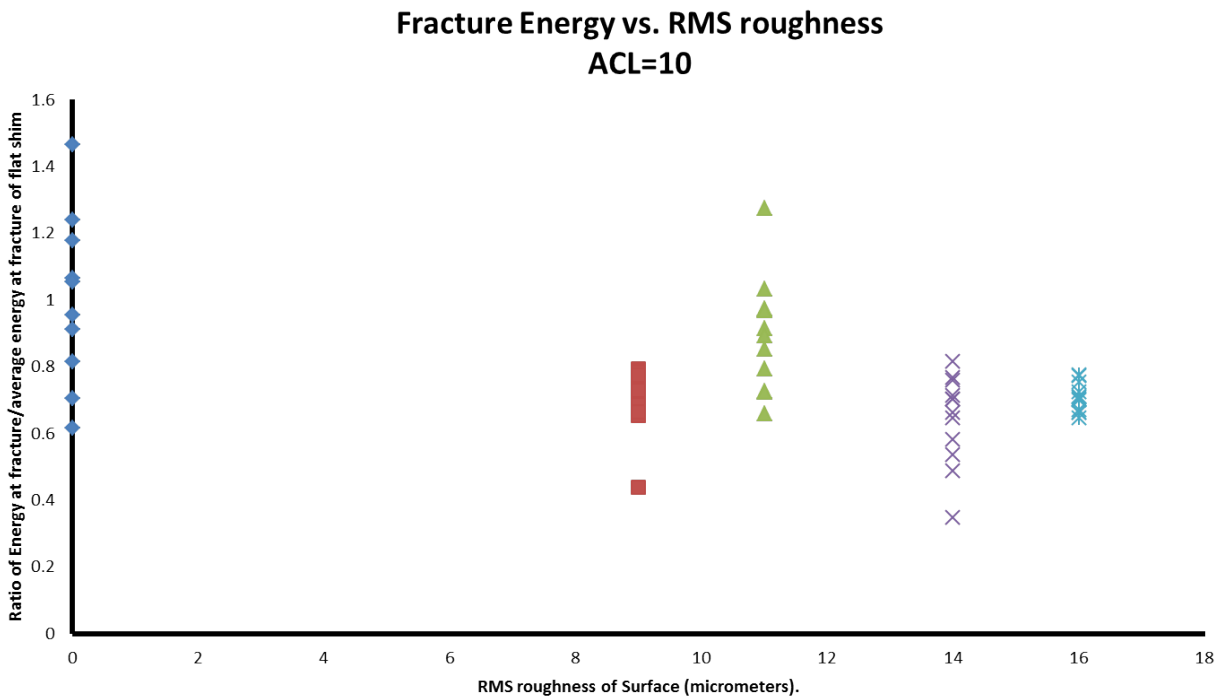

Fig. 52. Energy at fracture versus RMS roughness of surface, starting with a flat surface until the early stage of degradation, which is the focus of the present study. ACL = 10. RMS = 0 means a flat surface.

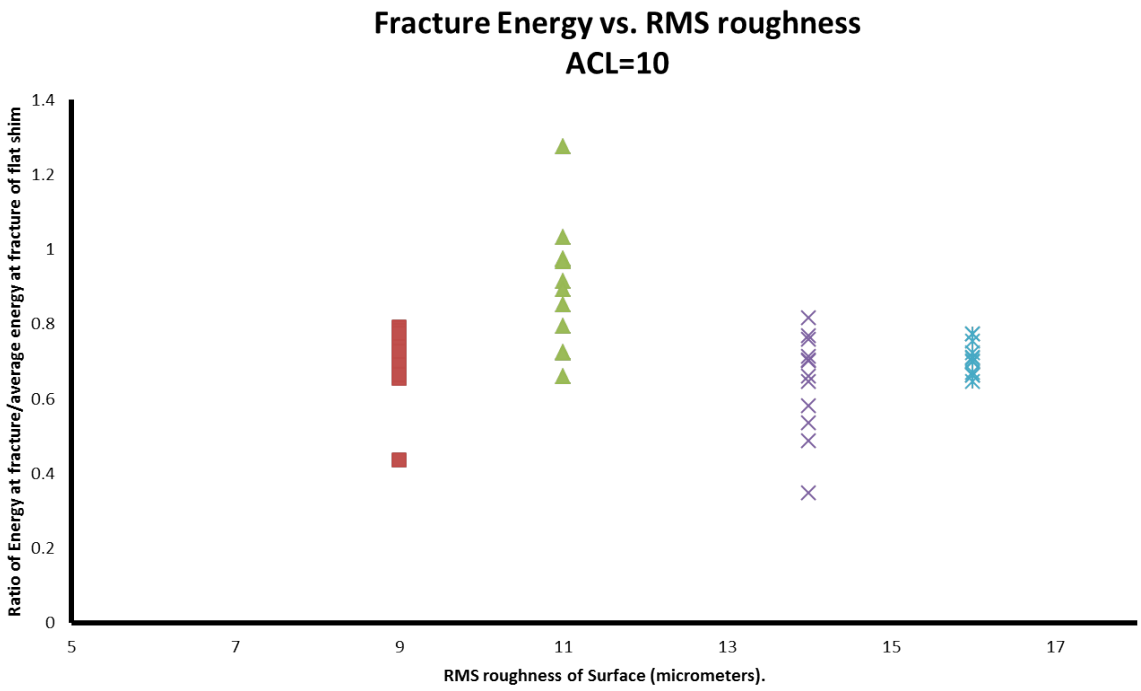

Fig. 53. Energy at fracture versus RMS roughness of surface, only for early stage of degradation considered in the present study. ACL = 10

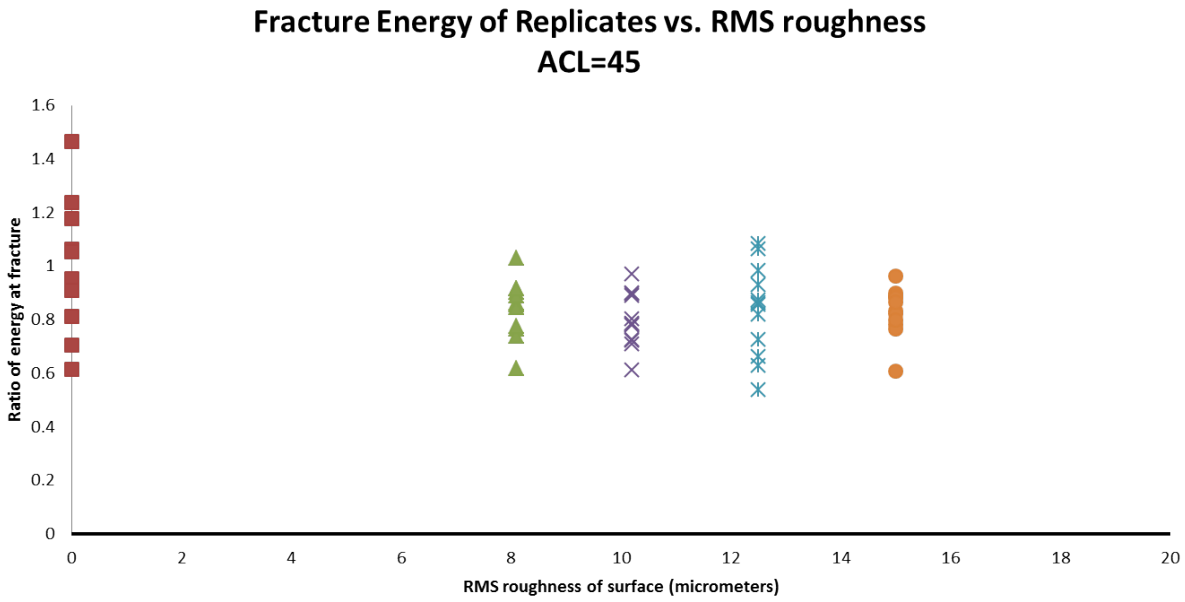

Fig. 54. Energy at fracture versus RMS roughness of surface, starting with a flat surface until the early stage of degradation. ACL = 45. RMS = 0 means a flat surface

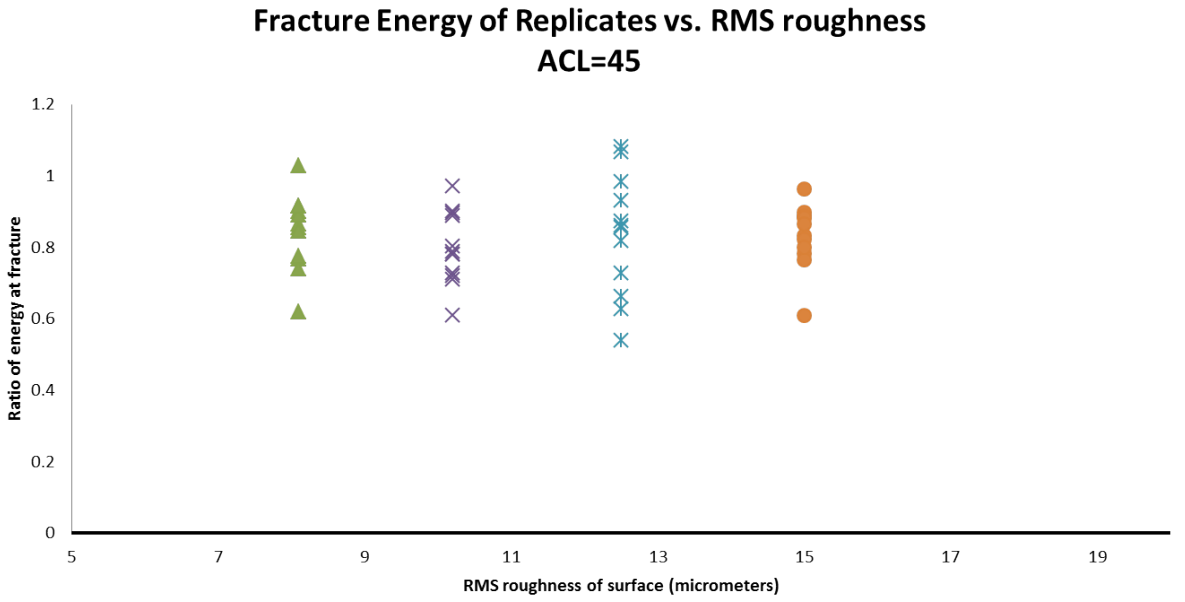

Fig. 55. Energy at fracture versus RMS roughness of surface, only for early stage of degradation considered in the present study. ACL = 45

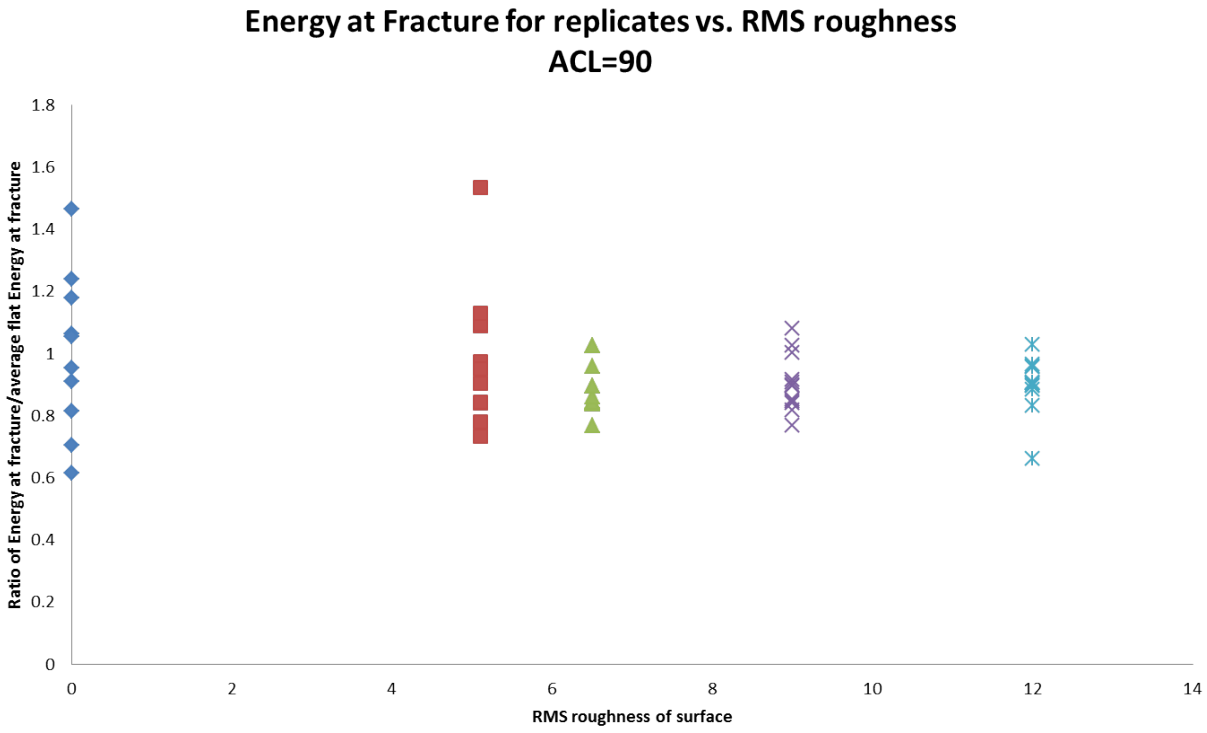

Fig. 56. Energy at fracture versus RMS roughness of surface, starting with a flat surface until the early stage of degradation. ACL = 45. RMS = 0 means a flat surface.

5.2.4 Discussion about Stress, Strain and Energy at Fracture Plots

There are several interesting observations that need to be addressed with regards to the behavior of stress, strain and energy at fracture versus RMS roughness. First of all, it is observed that the early degradation produced to the specimens is sufficient to reduce the stress, strain and consequently the energy a fracture for all kinds of surfaces (all ACL) when compared to a nominally flat specimen. Secondly, the different degradation levels can not significantly distinguish themselves from each other with regards to the stress, strain, or energy at fracture; however, when compared to an even deeper degradation level (for example, see figure 51), one can observed the expected energy reduction. Thirdly, there seems to be a relaxation point or region (RMS value or range) at which the stress, strain, and thus energy at fracture seems to increase. This is in accordance to traditional results of the SCF for multiple periodic notches, wherein it tends to decrease as number of notches increases; this state of affairs can be observed, for example, in figure 16 from chapter 3. Furthermore, this relaxation point or region is apparently dependent on both ACL and RMS of the surface, since one can observe that it takes place at a smaller RMS value for surfaces having ACL=90 than for those having ACL=10, for example. Finally, it is definitely observable that neither stress, strain, nor energy at fracture are distinguishing markers of failure at the various level of early degradation. This is remarkably important, since in traditional strength of materials these are the first parameters sought to assess or predict fracture for nominally flat surfaces; however, early stage of degradation being small often times is ignored. Of course, most metals are considerably less brittle than PMMA at room temperature and therefore early degradation can be ignored; but when service conditions involve an important decrease of temperature, then even metals become brittle and no longer early stage of degradation can be ignored.

5.3 Fracture Location Density (FLD)

Based on the previous results, it was concluded that stress, strain, or energy at fracture showed low to no correlation to the geometrical parameters considered, namely RMS roughness and autocorrelation length (ACL). Therefore, we pursued the study of fracture location as a means to predict failure of the damaged specimens. As explained in chapter 4, the rough area was divided into 20 sections, reserving two of those lines for the rough-to-flat interface. The RMS roughness of each line was computed using the original developed xyz-data. Figures 57 through 60 show a series of plots corresponding to surfaces with ACL=10 and RMS= 9 to 16 microns, respectively. For ACL=10 and RMS =9 microns (figure 57), fracture location was found to be highly scatter and therefore no correlation was found between the fracture location density (FLD) and the RMS of profiles. For the case of ACL=10 and RMS=11 microns, the corresponding FLD vs. RMS_{line} plot (figure 58) seems to be less scatter than that corresponding to RMS= 9 microns, shown in plot of figure 57. In figure 59 a surface with ACL=10 and RMS= 14 microns shows a much higher correlation of FLD with RMS_{line}than the previous two surfaces. Finally, the aforementioned trend is corroborated by a deeper ablation, as it is shown in the plot of figure 60, corresponding to ACL=10 and RMS=16 microns.

These plots show that FLD increases its positive correlation with RMS of the lines as the surface grows. This trend is in agreement with traditional results for more regular surfaces. If one reckons RMS-roughness as a depth dimension, then it would be expected that: (a) there is a critical depth (critical RMS of surface, in our case) beyond which the location of fracture becomes positively dependent on the depth (RMS-roughness of lines); and, (b) Below that critical RMS, fracture location is not predictable based on the RMS. An analogy in cracked members is that of the critical crack size, a_c, beyond which a crack would grow under the stress, $\sigma = K_{IC}/\sqrt{\pi a_c}$, crack having sizes smaller than a_c would not provoke

fracture, as explained in details in chapter 3.

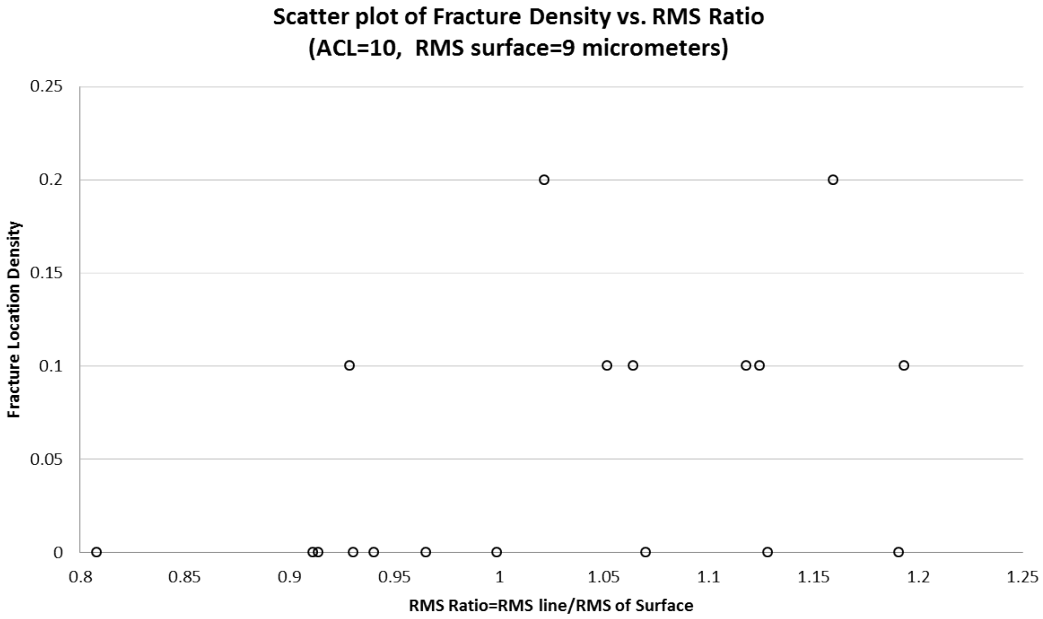

Fig. 57. Scatter plot of fracture location density(FLD) versus RMS roughness of profiles at discrete lines on the surface. Surface's RMS = 9 micrometers and ACL = 10. Notice the highly stochastic behavior. This plot was developed from 20 replicates.

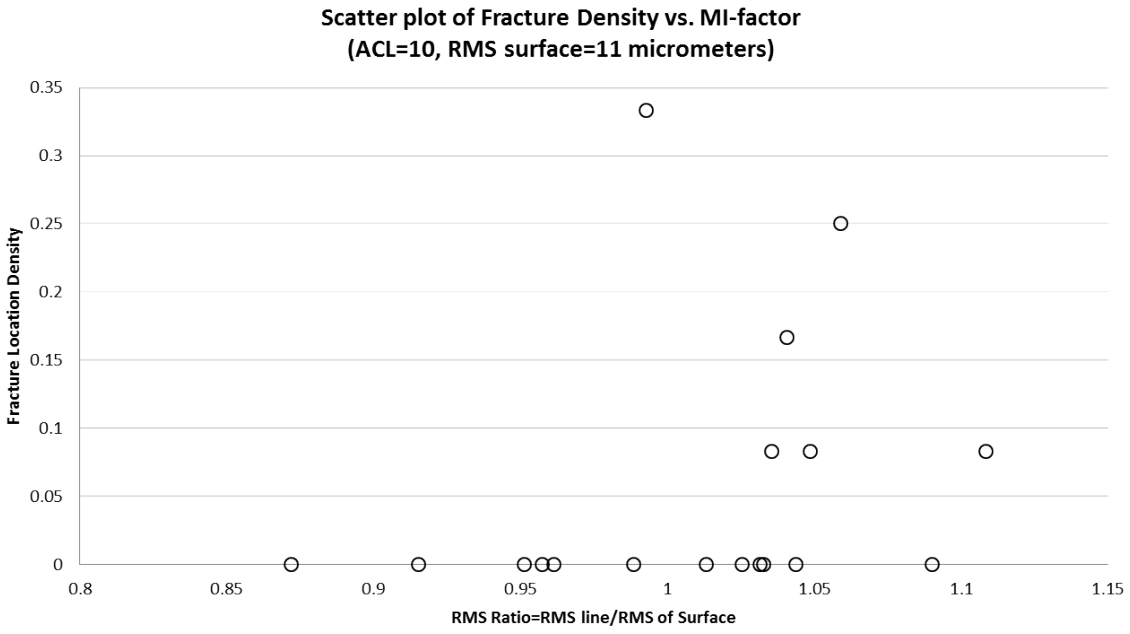

Fig. 58. Scatter plot of fracture location density(FLD) versus RMS roughness of profiles at discrete lines on the surface. Surface's RMS = 11 micrometers and ACL = 10. Notice even though behavior is still non-deterministic, yet it is less scatter than that of Fig. 57. This plot was developed from 24 replicates.

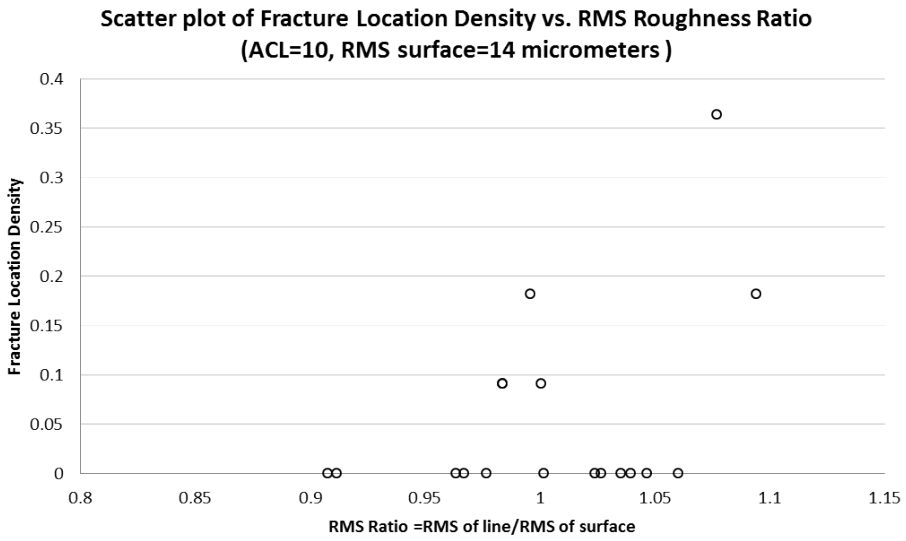

Fig. 59. Scatter plot of fracture location density(FLD) versus RMS roughness of profiles at discrete lines on the surface. Surface's RMS = 14 micrometers and ACL = 10. Notice the increasing trend of FLD that starts to appears as the profile roughness increases. This plot was developed from 22 replicates. Notice that there are two locations with the same roughness and FLD.

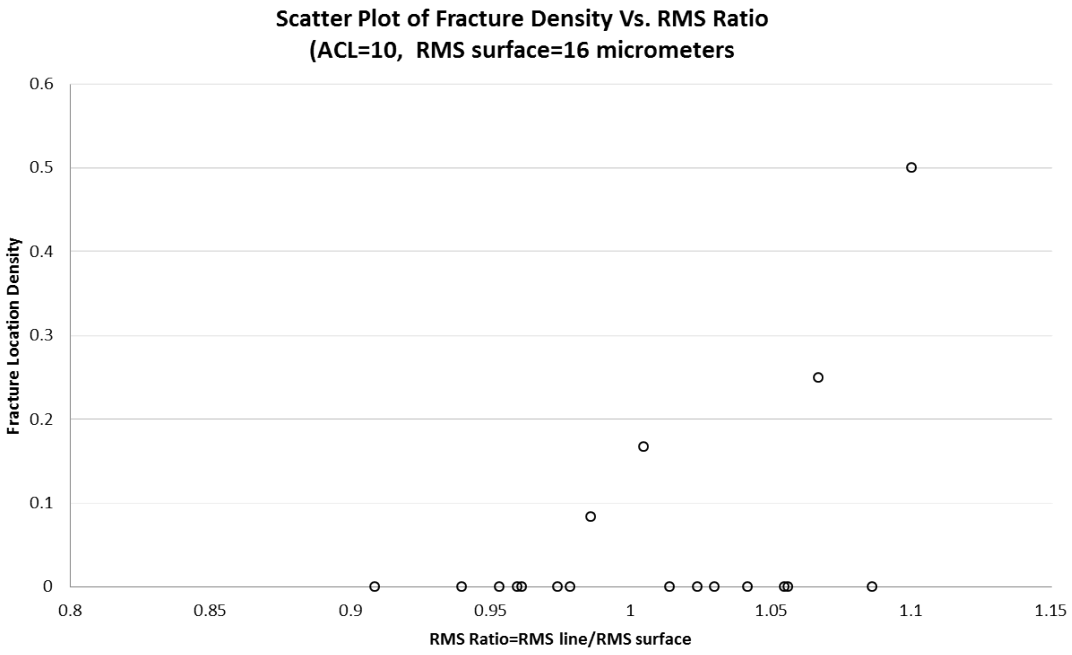

Fig. 60. Scatter plot of fracture location density(FLD) versus RMS roughness of profiles at discrete lines on the surface. Surface's RMS = 16 micrometers and ACL = 10. The positive correlation between FLD and profile RMS roughness is even more evident than that for RMS=16, plot of figure 59. This plot was developed from 24 replicates.

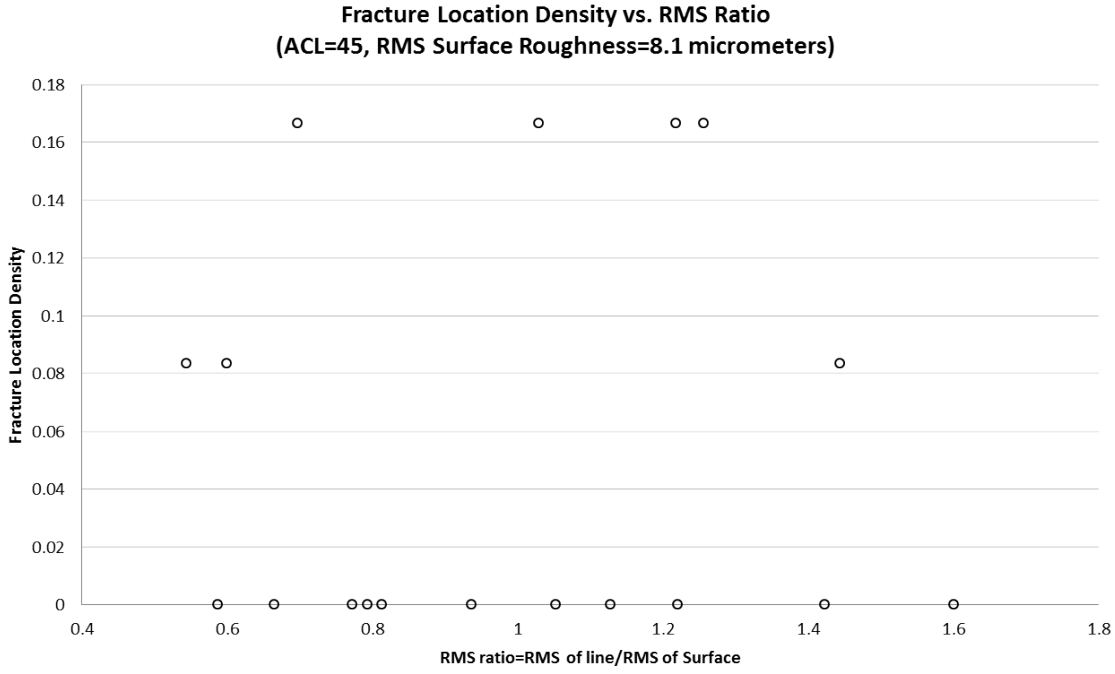

Fig. 61. Scatter plot of fracture location density(FLD) versus RMS roughness of profiles at discrete lines on the surface. Surface's RMS = 8.1 micrometers and ACL = 45. FLD is unpredictable with respect to RMS roughness, at this level of degradation. This plot was developed from 24 replicates. 2 specimens that broke at the rough–to-flat interface are included in the statistics.

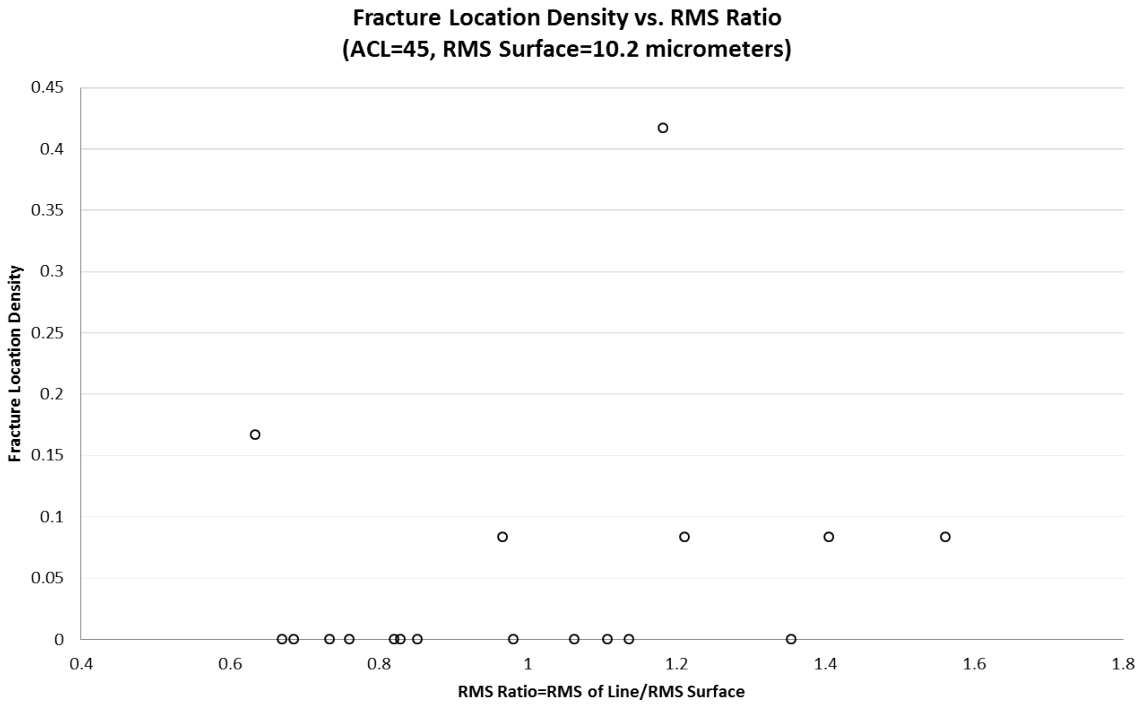

Fig. 62. Scatter plot of fracture location density(FLD) versus RMS roughness of profiles at discrete lines on the surface. Surface's RMS = 10.2 micrometers and ACL = 45. FLD is still unpredictable with respect to RMS roughness, at this level of degradation. This plot was developed from 24 replicates. 2 specimens that broke at the rough-to-flat interface are included in the statistics.

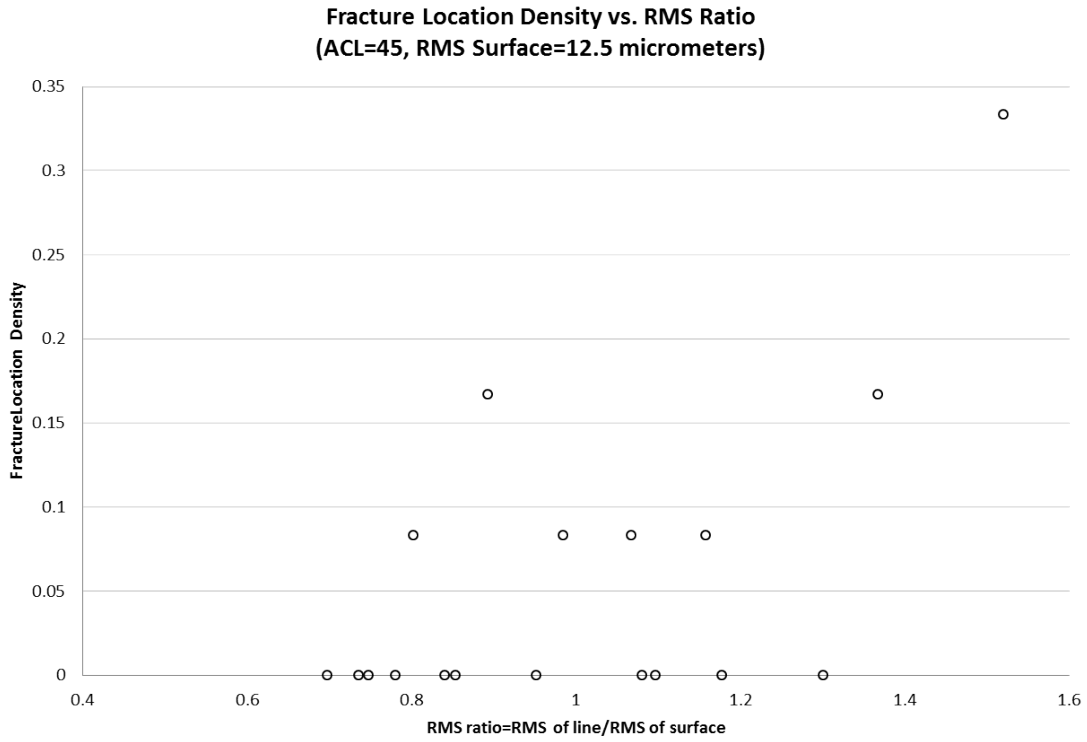

Fig. 63. Scatter plot of fracture location density(FLD) versus RMS roughness of profiles at discrete lines on the surface. Surface's RMS = 12.5 micrometers and ACL = 45. There appears to be a medium correlation between FLD and RMS roughness. This plot was developed from 24 replicates.

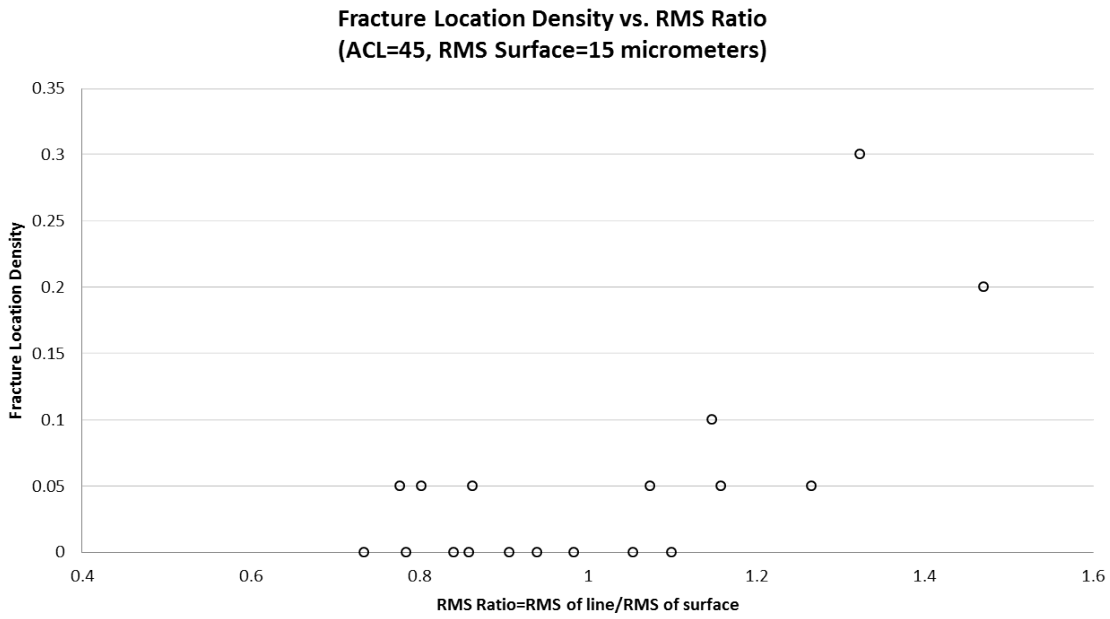

Fig. 64. Scatter plot of fracture location density(FLD) versus RMS roughness of profiles at discrete lines on the surface. Surface's RMS = 15 micrometers and ACL = 45. It is clear that there is a positive correlation between FLD and RMS roughness, after some threshold roughness. This plot was developed from 20 replicates. 2 specimens that broke at the rough-to-flat interface were included in the statistics.

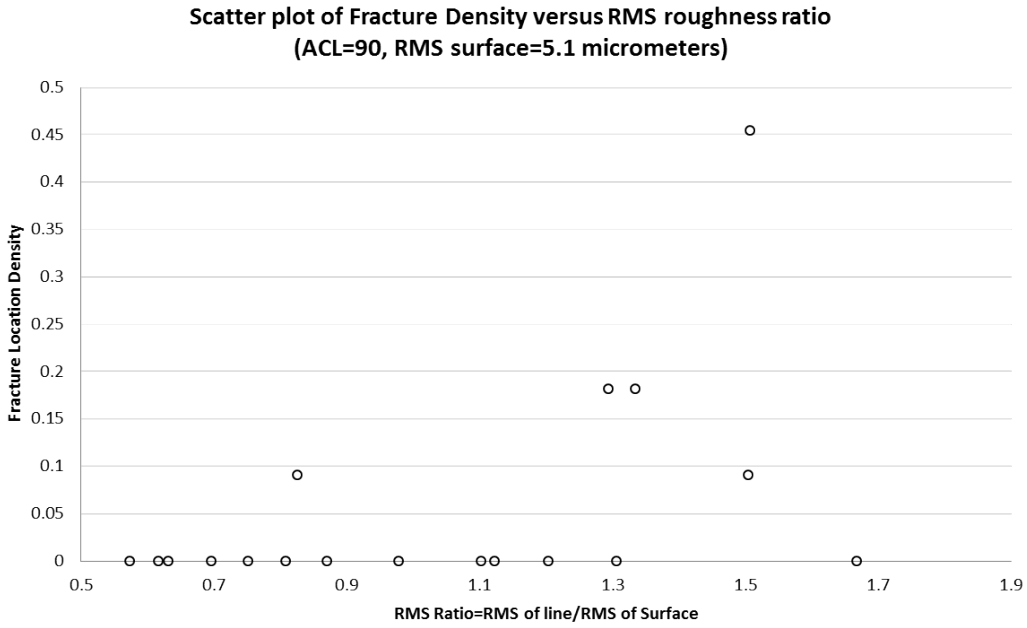

Fig. 65. Scatter plot of fracture location density(FLD) versus RMS roughness of profiles at discrete lines on the surface. Surface's RMS = 5.1 micrometers and ACL = 90. At this level of degradation there is no clear correlation. This plot was developed from 22 replicates.

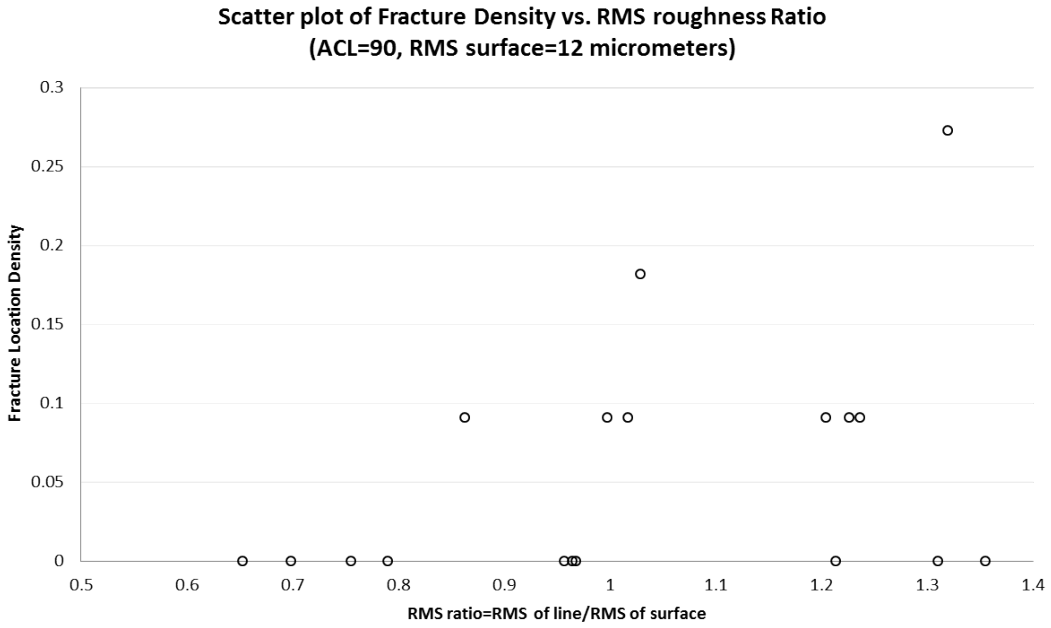

Fig. 66. Scatter plot of fracture location density(FLD) versus RMS roughness of profiles at discrete lines on the surface. Surface's RMS = 12 micrometers and ACL = 90. Even at this considerable roughness, the correlation is not as strong as that for other ACL. This plot was developed from 22 replicates.

5.3.1 Discussion on Correlation with RMS of Profiles

In all the scatter plots of the fracture location density (FLD) versus RMS roughness of lines (or profiles) shown there is a common observation: that the correlation between FLD and RMS-line increases as the surface becomes rougher. The dynamics of this growth seems to be dependent on the ACL of the surface. That the probability of fracture is higher at larger RMS should be expected since it behaves as an asymptotic approach to the traditional deterministic fracture mechanics solution to the critical flaw problem. The rougher the surface, the higher the likelihood of breaking at the most probable location (i.e., the roughest profile). This means that the process becomes less stochastic as the surface gets rougher.

For less rough surfaces, however, even at particular profiles that are about 50% rougher than the overall surface, the likelihood of fracture is still remarkably small.

5.3.2 Correlation with ACL

The graphs contained in figures 67, 68, 69, and 70 are scatter plots of fracture location density versus ACL ratio (ACL_r). The ACL_r is the ratio of the ACL of a line (or profile) to the ACL of the entire surface. The latter is simply prescribed during the design of the surfaces. The former is obtained by averaging the distances between correlated pit depths. As it has been stated before, the auto correlation length is the average distance between two local pit depths of a surface (or it can be any physical quantity depending on the system being studied) beyond which the depths of those pits are not longer correlated but are random. That distance was measured for each one of the 20 lines used to divide the surfaces. Then those ACL_{line} were divided by the general ACL of the entire surface.

That there is an increasing negative correlation between FLD and ACL_{line} as degradation increases is evident from plots of figures 67–70. Although for the two surfaces correspond-

ing to RMS=9 micrometers (figure 67) and RMS=11 micrometers, this trend might not appear too clear, yet for the following two degradation levels, namely, RMS=14 micrometers (figure 69) and RMS = 16 micrometers (figure 70) the high correlation is obvious. The Pearson's correlation coefficient of that latter plot is above 0.9—being this a negative value, of course.

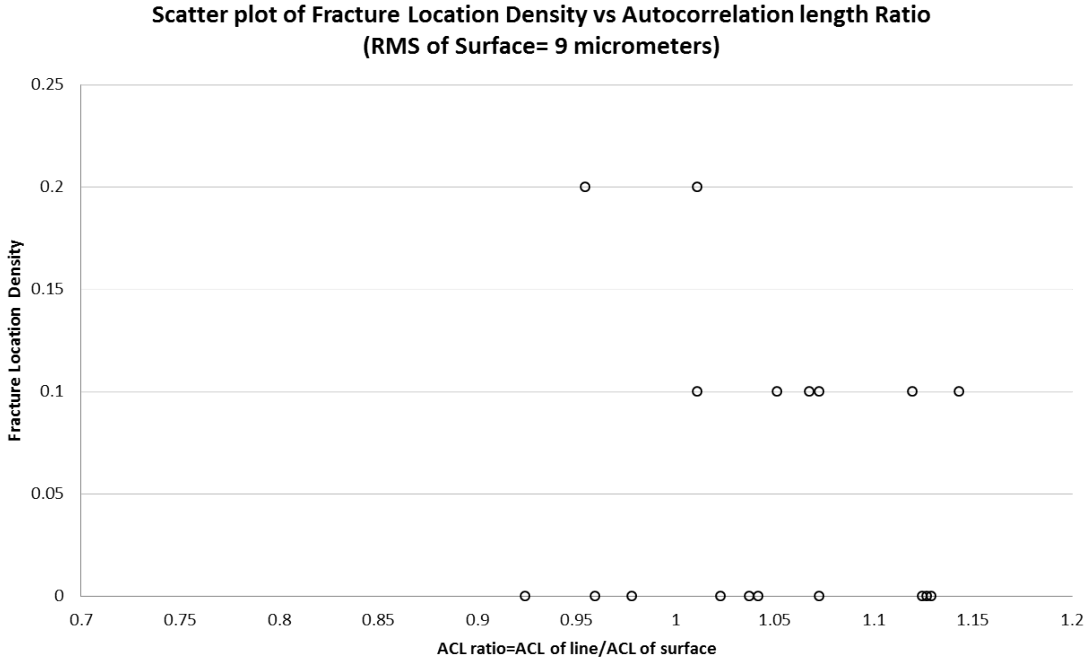

Fig. 67. Scatter plot of fracture location density(FLD) versus ACL of line, or profile, for a surface's RMS= 9 micrometers. There appears to be a negative correlation between FLD and ACL line, in this case weak but not negligible. This plot was developed from 20 replicates.

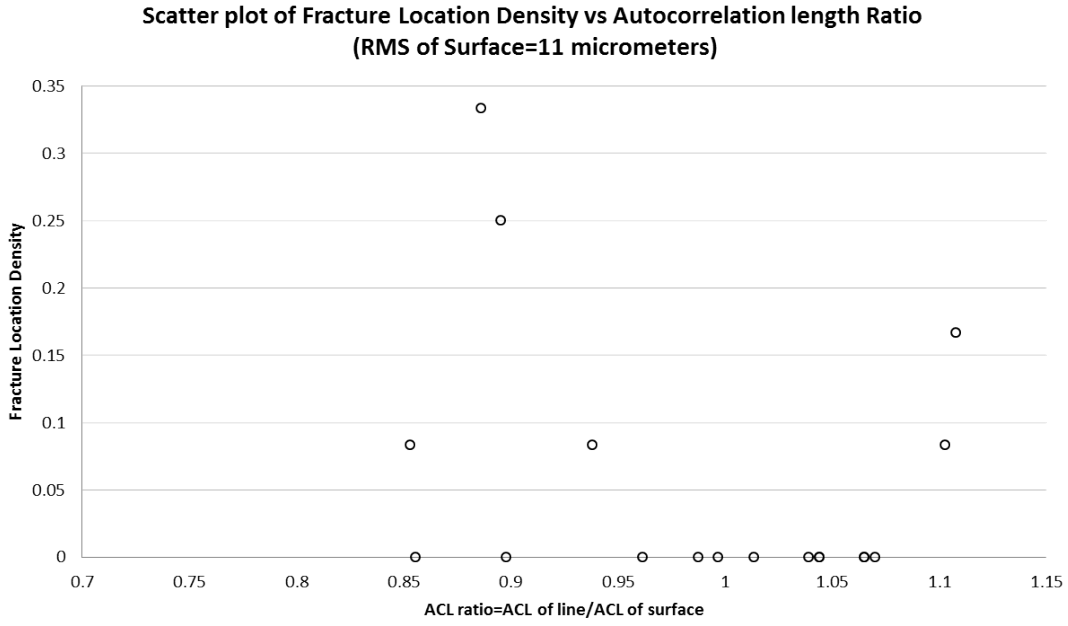

Fig. 68. Scatter plot of fracture location density(FLD) versus ACL of line, or profile, for a surface's RMS= 11 micrometers. There appears to be a negative correlation between FLD and ACL line, in this case weak but not negligible. This plot was developed from 24 replicates.

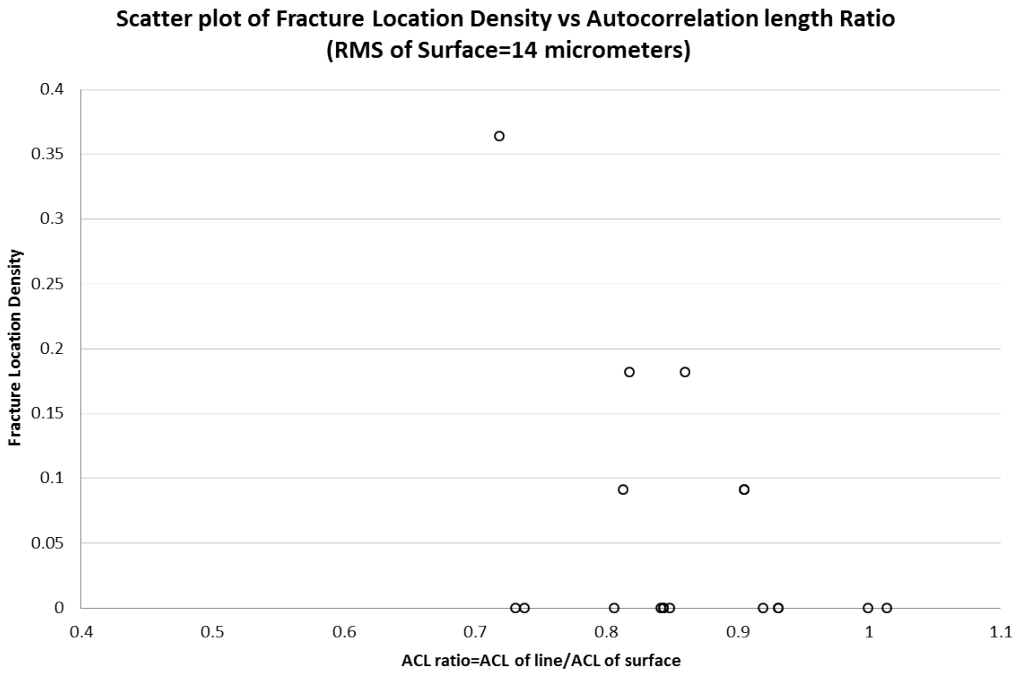

Fig. 69. Scatter plot of fracture location density(FLD) versus ACL of line, or profile, for a surface's RMS= 14 micrometers. The negative correlation is definitely stronger than those for plots in figures 67 and 68. This plot was developed from 22 replicates. Noticed that two locations have same FLD and ACL.

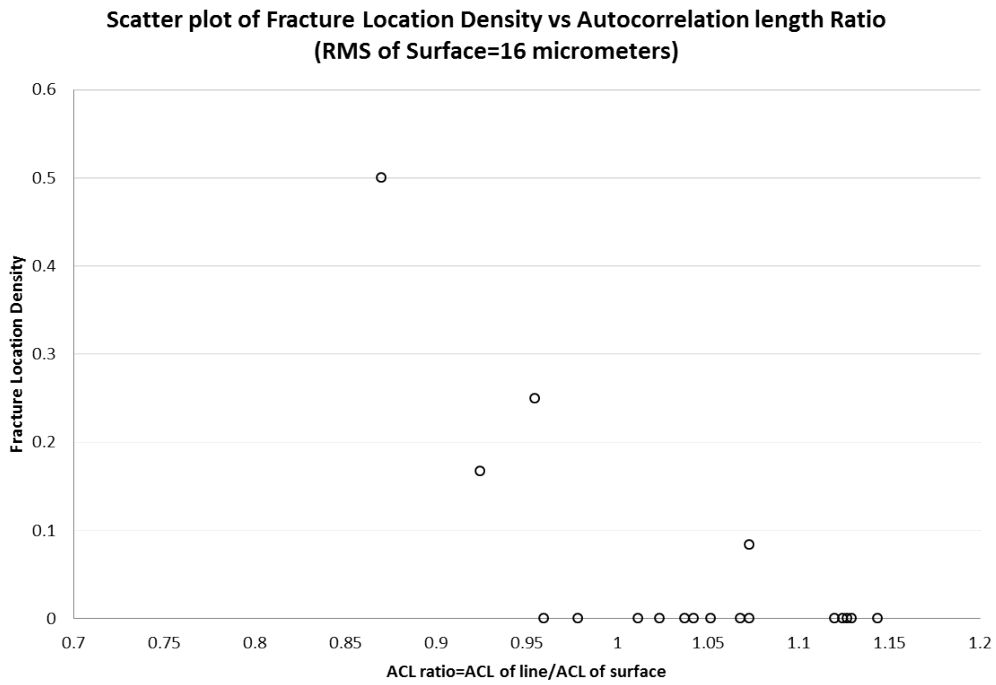

Fig. 70. Scatter plot of fracture location density(FLD) versus ACL of line, or profile, for a surface's RMS= 16 micrometers. At this level of degradation, a strong negative correlation between FLD and ACL line is evident. This plot was developed from 24 replicates.

5.3.3 Discussion on Correlation with ACL of Profiles

The scatter plots of FLD with ACL of profiles show the reciprocal correlation behavior seen previously versus RMS-line. As the surface becomes rougher, the probability of the specimen fracturing at profiles with smaller ACL increases. This observation is remarkably important. Traditional fracture mechanics have focused on the geometrical aspects of the notch(es), almost neglecting the geometry related to the tendons (islands) that connect them. The ACL length of a profile can be thought of as an average measure of the tendon width perpendicular to the loading axis (if the load can be thought of as tension being applied at the ends of a rough film). Therefore, at least for the conditions studied herein, we can conclude that the tendon width (perpendicular to load) is inversely proportional to stress concentration: the smaller the tendon the higher stress concentrates.

To further understand this, we observe the FEA's surface stress distributions shown in figure 71, corresponding to a beam with 3 grooves, subjected to bending load. When a thick tendon is located at the center of the middle groove the stress relaxes there which reduces the probability of fracture at that location. However, when a thin tendon is placed at the same location, the stress concentrates thus increasing the likelihood of failing there.

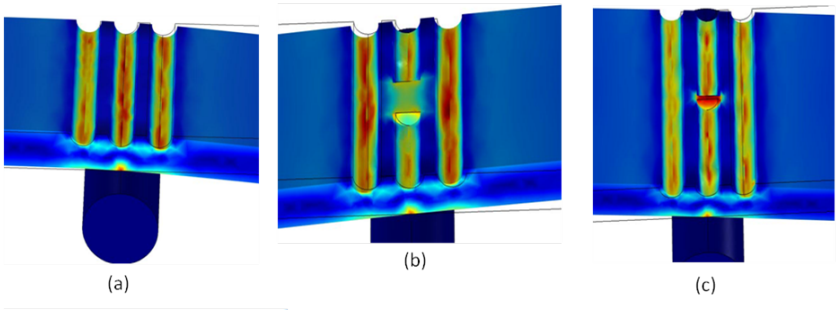

Fig. 71. Finite element simulation of beam under bending with 3 grooves and (a) no tendon, (b) a thick tendon, and (c) and thin tendon. Stress concentrates more due to the thin tendon than the thick one.

5.3.4 Discussion on Stress Concentration and RMS/ACL

Since the likelihood of fracture, for our quasi-brittle material has been shown to increase with increase of RMS roughness and with decrease of ACL, then our main conclusion is that the FLD, and more importantly the stress concentration factor must be a function of RMS/ACL, or:

$$FLD = Function(\frac{RMS}{ACL}) \tag{5.1a}$$

$$SCF = Function(\frac{RMS}{ACL}) \tag{5.1b}$$

This insight leads us to plot FLD versus the ratio RMS/ACL, which should be expected to show even higher correlation. Following there are four scatter plots shown in figures 72, 73, 74, and 75 to demonstrate this state of affairs.

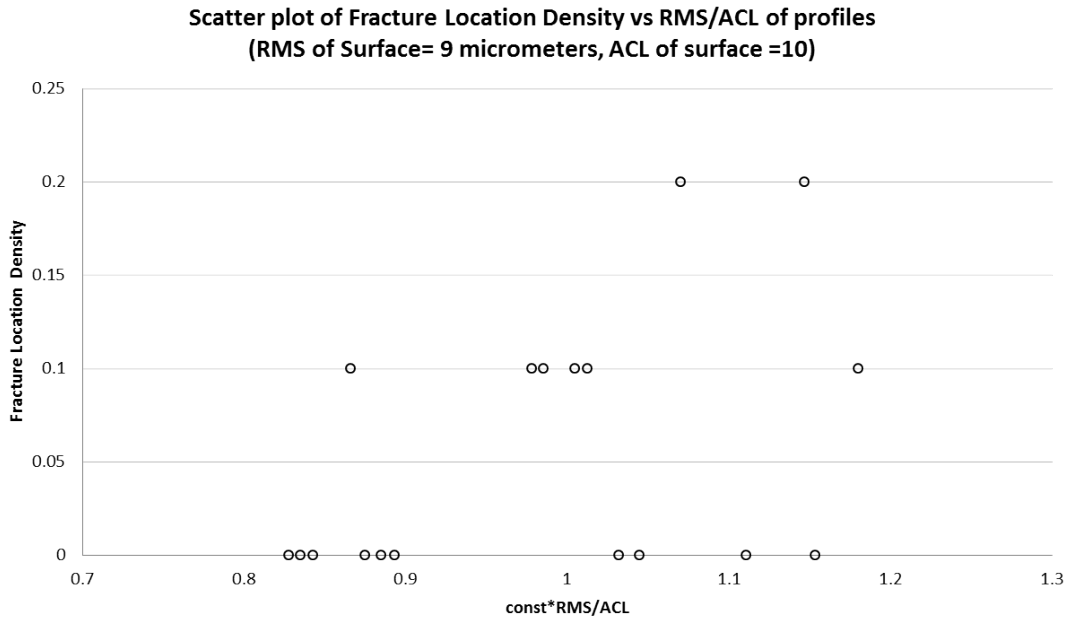

Fig. 72. Scatter plot of fracture location density(FLD) versus the ratio RMS/ACL (times a constant) of line, or profile, for a surface's RMS = 9 micrometers. This plot was developed from 20 replicates.

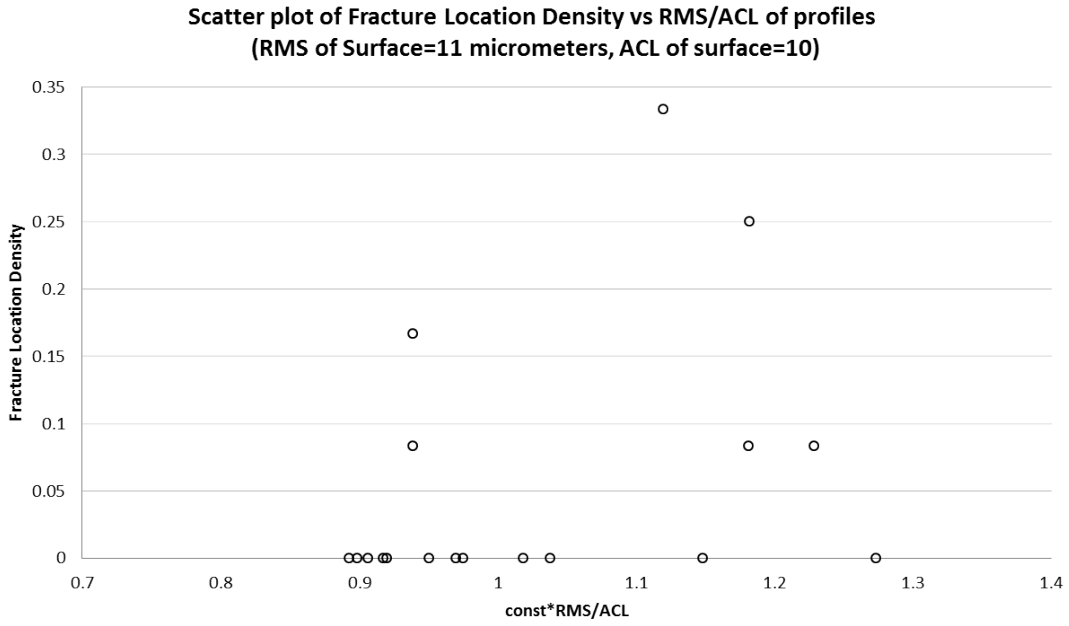

Fig. 73. Scatter plot of fracture location density(FLD) versus the ratio RMS/ACL (times a constant) of line, or profile, for a surface's RMS = 11 micrometers. This plot was developed from 24 replicates.

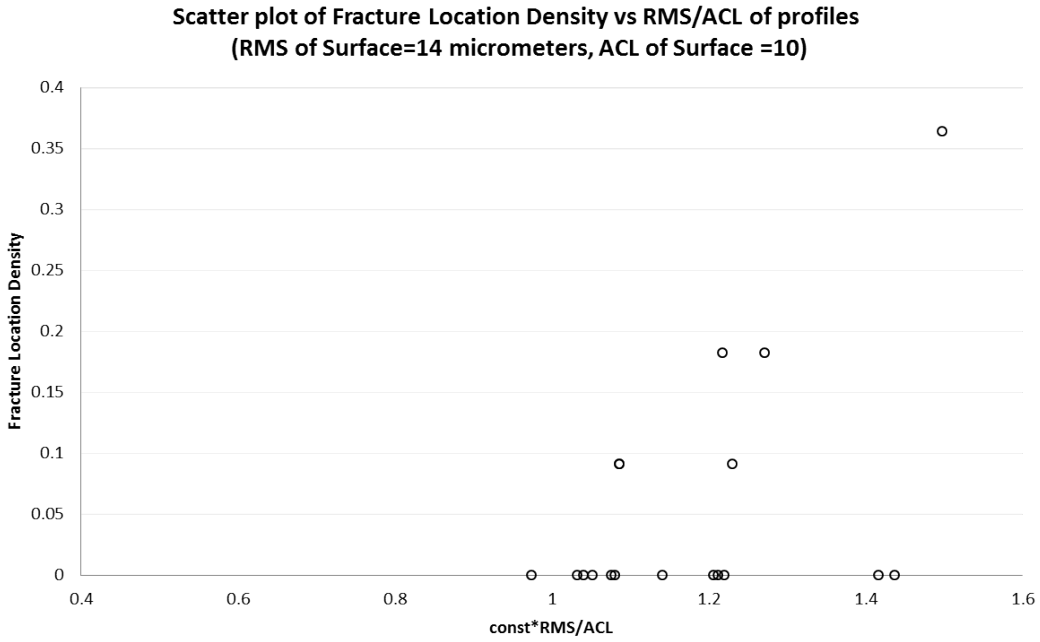

Fig. 74. Scatter plot of fracture location density(FLD) versus the ratio RMS/ACL (times a constant) of line, or profile, for a surface's RMS = 14 micrometers. This plot was developed from 22 replicates.

As expected, the FLD correlation with the ratio RMS/ACL is much evidently higher than with RMS or ACL individually. This empirical result could be refined by least-squared methods; but more importantly, one wonders if there is an analytical solution that can be pursued in order to corroborate this empirical result. In fact, this is carried out successfully and presented in chapter 6 of this document. Comparison of the experimental results and analytical predictions are also carried out and shown.

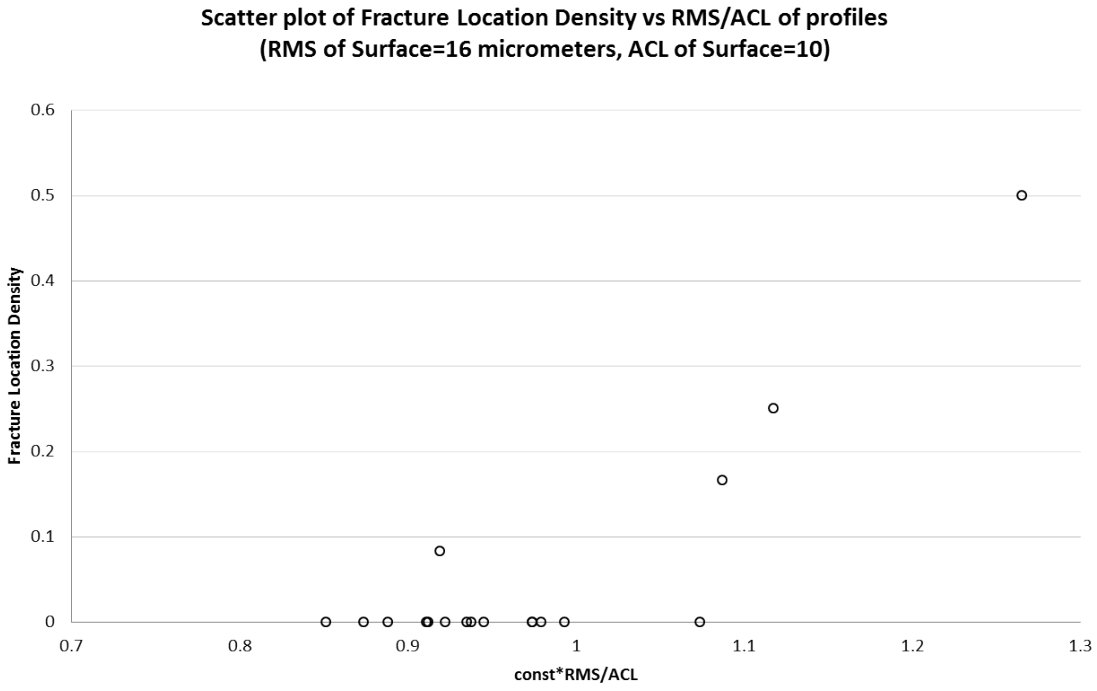

Fig. 75. Scatter plot of fracture location density(FLD) versus the ratio RMS/ACL (times a constant) of line, or profile, for a surface's RMS = 16 micrometers. This plot was developed from 24 replicates.

5.4 Variation of Brittleness and its Effect on Correlation

By varying the temperature inside an environment chamber, PMMA beams were tested to fracture using ASTM D790 standard procedure B. The results shown in this section correspond to temperatures at 10 °C, 23 °C (a.k.a. room temperature), 25 °C, 27 °C,

and 30 °C. Undamaged (nominally flat) specimens were used to correlate temperatures with mechanical properties of the material in order to describe the behavior of brittleness. Two mechanical properties were considered, namely, % of elongation (% EL) and Young's modulus of elasticity (E). %EL is described as the maximum percent of elongation that a specimen can experience before it breaks. Since three-point bending tests expose the outer fibers to tension, then it can be said that our %EL is the maximum strain attained by the rough surface before it gives in to fracture. It coincides with the strain at fracture only when the material fractures before yielding. Figure 76 shows a plot of %EL versus temperature for PMMA. As it would be expected, the higher the temperature the higher the strain the specimens can stretch before fracturing; nonetheless, this increase is not linear. Similarly, figure 77 shows a plot of E versus temperature. Again, as expected Young's modulus of elasticity decreases with temperature increase. Even though the same number of flat specimens were used to obtain the aforementioned data, it seems that E delivers a more precise way of characterizing changes in brittleness or ductility. Notwithstanding, we will use both E and %EL to characterize our thermally controlled test results. As an additional piece of information, we have included a plot of %EL versus E as shown in figure 78.

Our goal is to find the how correlation between FLD and RMS (or ACL) changes as brittleness is decreased (i.e., as E decreases or as %EL increases). In order to accomplish this, we selected among all the configurations tested, the ones that showed the highest correlation at room temperature. Then, that particular surface configuration was tested at the various values of E and %EL described before. The selected surface was ACL=45 with RMS=15 micrometers, for which the scatter plot at $E = 3.38 \pm .15 GPa$ was shown in figure 64. Scanned pictures of specimens tested at various E or %EL were produced.

It was found that even at a temperatures between 27 to 30 °C the correlation between FLD and RMS/ACL vanishes and all specimens fracture at the location of maximum load, that is, the center of the specimen. This means that when PMMA has an elastic modulus

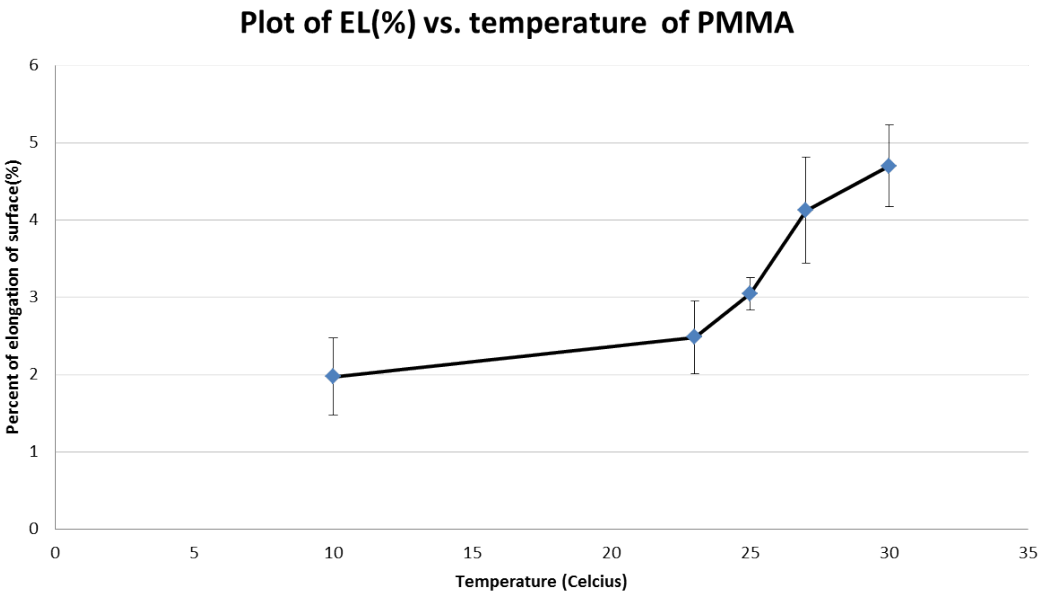

Fig. 76. Plot of percent of elongation (%EL) versus temperature of PMMA. Flat (non-rough)specimens were used to produce this plot.

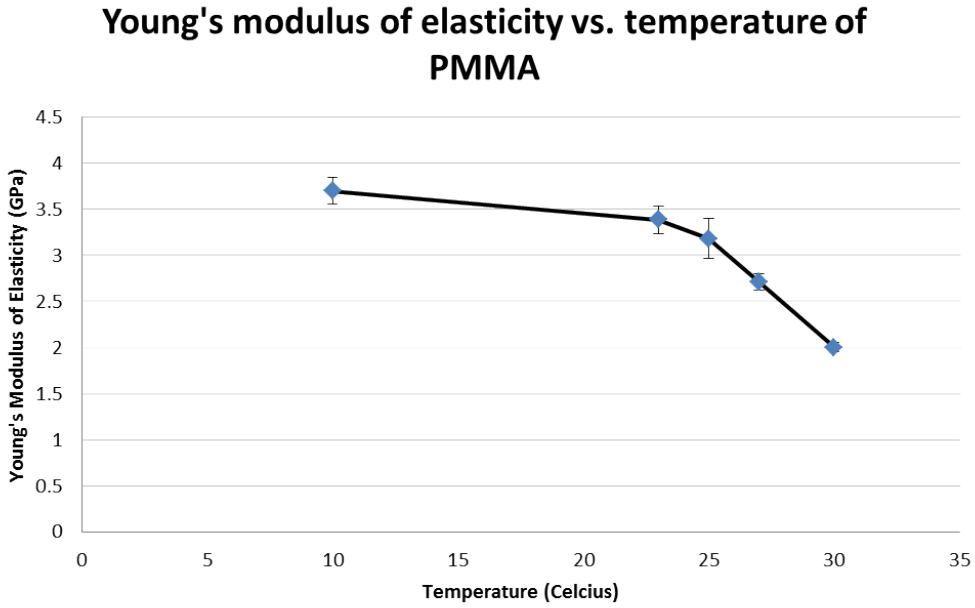

Fig. 77. Plot of Young's modulus of elasticity versus temperature of PMMA. Flat specimens were used to produce this plot.

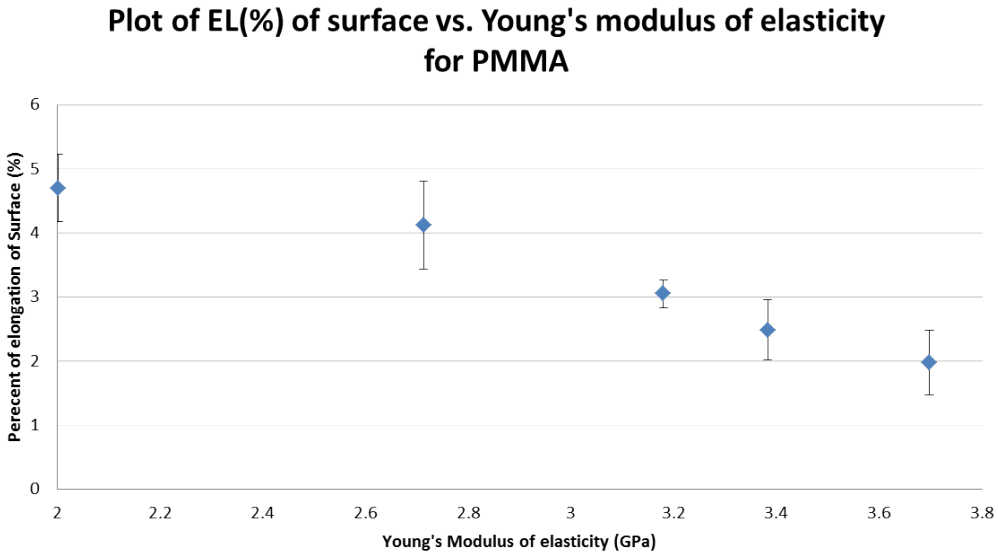

Fig. 78. Plot of percent of elongation (%EL) versus Young's modulus of elasticity. Flat specimens were used to produce this plot.

of about 2-2.7 GPa—or similarly, a % EL of about 4-5 %—early degradation, as described before, does not induce significant concentration of stress due to the rough surface.

5.5 General Discussion and Conclusions of Experimental Work

We have carried out three-point flexural tests on D790 replicated specimens of PMMA according to procedure B of the ASTM's respective standard. The specimens possessed random rough surfaces on a half-inch span at the central location. These rough surfaces were characterized by their root-mean-square (RMS) roughness and auto correlation length (ACL). Mainly the experimental work was carried out at room temperature, but degree of brittleness was varied via temperature change. The sole purpose of the latter was to assess the level of ductility of PMMA at which correlation between FLD with RMS/ACL vanishes at early stage of degradation.

i. At the early stage of degradation studied, prediction of fracture location is stochastic yet predictable in the probabilistic sense.

ii. The slight degradation produced to the specimens was sufficient to reduce the stress, strain and consequently the energy a fracture for all kinds of surfaces (all ACL) when compared to a nominally flat specimen.

iii. There seems to be a relaxation point or region (RMS value or range) at which the stress, strain, and thus energy at fracture seem to increase. This is in accordance to traditional results of the SCF for multiple periodic notches, where it tends to decrease as number of notches increases.

iv. Neither stress, strain, nor energy at fracture are distinguishing markers of failure at the various level of early degradation. This is remarkably important, since in traditional strength of materials these are the first parameters sought to assess or predict fracture for nominally flat surfaces; however, early stage of degradation being small often times is ignored. Of course, most metals are considerably less brittle than PMMA at room temperature and therefore early degradation can be ignored; but when service condi-

tions involve an important decrease of temperature, then even metals become brittle and no longer early stage of degradation can be ignored.

v. For quasi-brittle PMMA surfaces, prediction of failure location can be carried out even under random degradation at early stages, and it is partially dependent of the characteristic parameters of the surface, namely RMS roughness and ACL.

vi. There was found correlation between FLD and RMS roughness. This dependence of the location of fracture on RMS roughness indicates that the rougher the surface, the higher the likelihood of breaking at the roughest profile. This means that the process becomes less stochastic as the surface gets rougher. For less rough surfaces, however, even at particular profiles that are about 50% rougher than the overall surface, the likelihood of fracture is remarkably small.

vii. An increasing reciprocal correlation behavior between FLD and ACL was found, as RMS increases. As the surface becomes rougher, the probability of the specimen fracturing at profiles with smaller ACL increases. This observation is remarkably important. Traditional fracture mechanics have focused on the geometrical aspects of the notch(es), almost neglecting the geometry related to the tendons (islands) that connect them. The ACL length of a profile can be thought of as an average measure of the tendon width perpendicular to the loading axis (of the load can be taken as tension being applied at the ends of a rough film). Therefore, at least for the conditions studied herein, we can conclude that the tendon width (perpendicular to load) is inversely proportional to stress concentration: the smaller the tendon the higher stress concentrates.

viii. It is concluded that the stress concentration factor must be a function of the ratio RMS/ACL.

ix. Additionally, as degradation penetrates randomly and roughness (height) becomes nor-

mally distributed, according to the CLT, the multi-pit problem can be very well approximated using a single average pit.

x. When the value of Young's modulus is about 2-2.7 GPa—or similarly, a % EL of about 4-5 %—early degradation, as described before, does not induce sufficient concentration of stress due to the rough surface at an early stage of degradation, and therefore the correlation described above vanishes.

xi. In order to extend this knowledge obtained from the experimental work, an analytical solution of the problem is pursued in chapter 6.

CHAPTER 6

ANALYTICAL SOLUTION

6.1 Problem Description

It is widely accepted that the first[1] quantitative result for stress concentrations factor (k_t) was developed by Inglis [2, 36], who studied elliptical holes in flat plates. Since then, k_t values have been developed for a smorgasbord of configurations [3]. Although periodic-discontinuity arrangements have been well studied, rarely continuous-irregularity cases have been considered. Two exceptions are studies of k_t at slightly perturbed periodic surfaces for a homogeneous elastic material[16, 77] and for a film-substrate system [17]. In a pioneering work, Gao[16] employed some elastic *Greens functions* for a surface considered perfectly flat and treated the sinusoidal surface as being perturbed from that referential plane, to develop first-order solutions of the stress concentration factor. Later and as a continuation to Gao's work, Grekov and Makarov reported an algorithm that provides any-order approximation for the single-wave condition[114]. However, to the best of our knowledge, no theoretical studied has been carried out to formulate k_t for a surface with random roughness. Therefore, combining the aforementioned first-order perturbation approach with the Hilbert Transform and the Parseval's theorem, in this chapter, we develop an analytical solution of k_t for the case of a randomly slightly rough surface. The motivation of this work is as follows.

For instance, solar panels are exposed to a large number of low-impact-random events which by the central limit theorem lead to a Gaussian distribution of pit size [24, 82]. The

[1] Actually Neuber[34] affirms that in a Russian published document, Kolosov had arrived to a similar result four years earlier[35]

damage level might be small, yet when laminates of semiconductor layers with different crystal configurations are brought together, lattice mismatch causes strain at the interface thus leading to residual stresses. Reckoning either surfaces as nominally flat or discontinuities as well-defined could be misleading, mostly when the approximation of a given roughness does not accurately fit a well-defined configuration or when the scale of the damage is within certain regime. At best, overestimations of stress concentrations, although safe, lead to unnecessary increase of costs. Therefore, it is of interest to understand more accurately the mechanical effects that random roughness on surfaces poses on the load-capacity performance of volumes.

In chapter 5 , we suggested a first-order empirical approximation for k_t based on experimental results, which are now available in the literature[82]. In that study, replicates of rough, slightly damage surfaces were designed and realized on a large number of brittle acrylic specimens using a reported technique [79] which was presented in chapter 4. In that model, the surfaces grow linearly from an engineering surface to one whose heights are normally distributed, and which is autocorrelated with auto correlation length, ACL. In the aforementioned study, ACL was varied in order to portray different sizes of damage features. The experimental results showed that k_t–on discrete profiles perpendicular to the load—was a function of the RMS-to-ACL ratio, where RMS is the root-mean-square roughness of the profile at each discrete line (see chapter 5 and reference [82]). Herein, we develop an analytical solution which to a first-order approximation agrees with the aforementioned experimental results.

6.2 Normally distributed surface damage

In this section, we present our motivation of using surfaces having normal height distribution. Materials are incessantly experiencing transformation, both at molecular and macroscopic levels. The third law of thermodynamics elucidates—among other basic

concepts—that, unless at absolute zero temperature, atomic structures are intrinsically unstable and therefore prone to change to a more stable state; nevertheless, for many materials this rate is a rather unhurried process. Both molecular and macroscopic changes can occur as a result of energy input to the material system, introduced through the surface, or boundary, or developed within the volume of the material. Assuming only through-boundary interactions, it is generally the case that surfaces are more susceptible to these morphological alterations than the interior part of the material. Almost any known natural phenomenon can cause materials degradation: heat, light, short-wavelength electromagnetic radiation, radioactive emissions, chemicals, mechanical stress and interactions with bacteria, fungi or other life forms. Despite the need for understanding the fundamental mechanisms of each particular physical, chemical, biological, etc., degrading phenomenon, the fact is that they seldom act individually. Instead, they seize the structural integrity of surfaces by the accumulation of a large number of small destructive events. Granted, most of these small attacks are usually of low probability, although the magnitude of the impact would depend on the size of the surface; (Consider, for example, the comparison of a corrosive attack on a bridge versus the same attack on a MEMS metallic device). But the build-up effect of these low-probability events lead to morphological changes on the surfaces that can be modeled mathematically using the Central Limit Theorem. Let X_1, $X_2 ... X_n$, be a series of variables representing the size (depth, volume, etc.) of material removed or displaced as a consequence of respective degrading events, E_1, $E_2 ... E_n$, acting on a surface like the one shown in Fig. 79. In the same manner, let $X_1^{'}$, $X_2^{'} ... X_m^{'}$, be a set corresponding to synergistic events, $E_1^{'}$, $E_2^{'} ... E_n^{'}$, that are obtained from the possible combining attacks of two or more X_i. For example, $X_1^{'} = SC(X_1, X_2)$, where the function SC maps individual events effect into their combined effects. Now, let us further assume that all X_i's are random independent variables. This is a very reasonable assumption; since one expects that these environmental, damaging attacks often act independently one from the other. (Even though there are

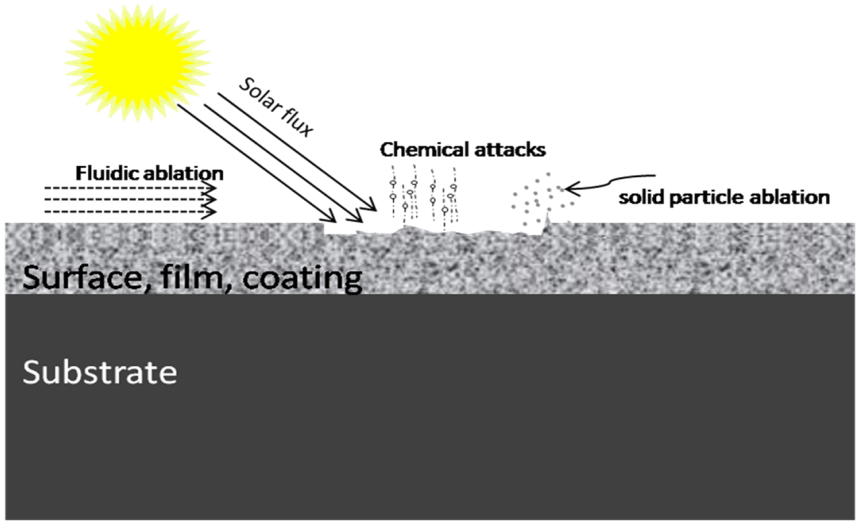

Fig. 79. Cartoon depicting some of the different sources of small destructive events from environment on surfaces. Based on the Central Limit Theorem these lead to Gaussian-distributed heights (or depths).

some events that could be associated with others, yet when the number of independent E_i is considerably large then this assumption holds reasonably well). Then, $X_i^{'}$, are also random variables since the sum and multiplication of two or more random variables is indeed another random variable. Now we can apply the Central Limit Theorem to simulate random degradation, assuming a large number of degrading events. The Central Limit Theorem (CLT) explains the behavior of the sum of random variables. Let $Z_1 ... Z_n$ be random variables such that $Z_i = X_i + X_i^{'}$, with sum,$S = \sum_{k=1}^{N} Z_k$,then CLT predicts that S will have a Gaussian distribution provided that:

a. Each summand that is not negligible compared to the dispersion of the entire sum has a distribution close to Gaussian.

b. The maximum of the absolute value of the negligible summands is itself negligible compared to the dispersion of the sum.

6.3 First-Order Perturbation for Slightly Damaged Surfaces

Consider an originally elastic flat surface with conditions as shown in Fig. 80(a). Then, consider that small amounts of material are added to or taken from that elastic surface in a random manner so that it becomes as that shown in Fig. 80(b), whose height is a continuous random variable having a Gaussian distribution, with autocorrelation length, *ACL*. (We can say that the 2-D surface shown in Fig. 80(b) can represent the profiles of the discrete lines of the surface as explained in chapters 3 and 4).

After the flat surface has been perturbed, we can define the stress and displacements for the

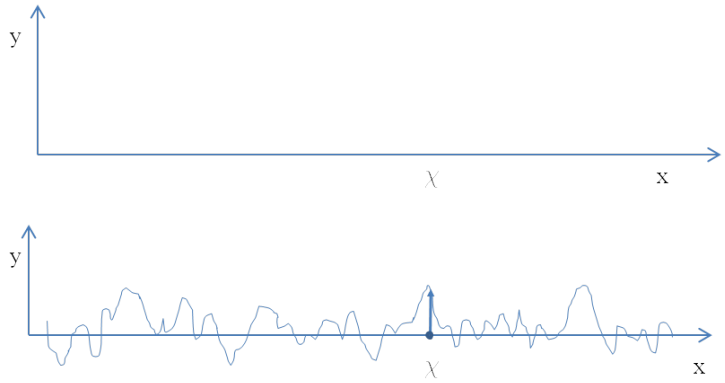

Fig. 80. (Top): An original flat surface; (Bottom):A random perturbation of the originally flat surface.

rough surface(T_{ij} and u_i) in terms of the reference state values (T^r_{ij} and u^r_i) and the perturbed elements (δT_{ij} and δu_i), as:

$$\begin{aligned} T_{ij} &= T^r_{ij} + \delta T_{ij} \\ u_i &= u^r_i + \delta u_i \end{aligned} \tag{6.1}$$

In order to solve Eqn. (6.1), we need suitable expressions for the perturbed elements, δT_{ij} and δu_i. Actually, since our interest is to find k_t then the stress is our main objective.

We formulate our problem by considering that the surface in Fig.80 is loaded with tensile stress σ_t, just as it was carried out in the experiments, see chapter 5 and reference [82].

For the remainder of this section, we employ the first-order perturbation method developed by Gao [77]. In the next section, we will apply these results to derive our particular configuration of interest. Following Gao [77] we also consider a concentrated point force **F** acting at an arbitrary location (x,y). The purpose of using a point force is only to utilize the well-known solution for the surface stress Green's function, and the magnitude of **F** will be shown to be irrelevant. Since we are considering only linear elastic materials, the strain energy density (w) is given in terms of the stress (T_{ij}) and strain (ϵ_{ij}) tensors, and the compliance tensor, C_{ijkl}, as :

$$w = \frac{1}{2} T_{ij} \epsilon_{ij} \tag{6.2}$$

$$w = \frac{1}{2} C_{ijkl} T_{ij} T_{kl} \tag{6.3}$$

Along the surface, where the traction vanishes, w becomes:

$$w = \begin{cases} \frac{1}{2E} T_{xx}^2, & \text{for plane stress} \\ \frac{1-\nu^2}{2E} T_{xx}^2, & \text{for plane strain} \end{cases} \tag{6.4}$$

Where E and ν are the modulus of elasticity and Poisson's ratio, respectively. Let's define E' as:

$$E' = \begin{cases} E, & \text{for plane stress} \\ \frac{E}{1-\nu^2}, & \text{for plane strain} \end{cases} \tag{6.5}$$

We then differentiate (6.4) with respect to the point force **F** and obtain:

$$\frac{\partial w}{\partial F_i} = \frac{T_{xx}}{E'} \frac{\partial T_{xx}}{\partial F_i} = T_{xx} \frac{G_{xx}^i}{E'} \tag{6.6}$$

By noticing that,

$$G_{xx}^i(\chi; x, y) = \frac{\partial T_{xx}}{\partial F_i} \tag{6.7}$$

is identified as the surface stress at χ due to a concentrated point force located at (x,y) and acting in the i direction.

Referring again to Fig.80, the change in total energy ($\delta\Pi$) has been defined [77] as:

$$\delta\Pi = F_i \delta u_i(x, y) + \int_{-\infty}^{\infty} w \delta p(\chi) d\chi \tag{6.8}$$

The first term in the right hand side represents the *i*th component of virtual work, performed by the *i*th component of the point Force, F_i, through a small displacement δu_i, in that same direction. The second term represents the total strain energy due to the addition or removal of material at each location χ, that is due to the perturbed quantity $\delta p(\chi)$ at each χ. Since Π is a state variable, then

$$F_i \delta u_i(x, y) = -\int_{-\infty}^{\infty} w \delta p(\chi) d\chi \tag{6.9}$$

Which after some straightforward manipulation [2] can be transformed into:

$$\delta u_i(x, y) = -\int_{-\infty}^{\infty} \frac{\partial w}{\partial F_i} \delta p(\chi) d\chi \tag{6.10}$$

We now substitute Eq. (6.6) into Eq. (6.10):

$$\delta u_i(x, y) = -\int_{-\infty}^{\infty} T_{xx} \frac{G^i_{xx}}{E'} \delta p(\chi) d\chi \tag{6.11}$$

For the particular case when there is no concentrated force, the material is only exposed to the bulk stress, and $T^{F=0}_{xx} = T^r_{xx} = \sigma$, so (6.11) becomes:

$$\delta u_i(x, y) = -\frac{\sigma}{E'} \int_{-\infty}^{\infty} G^i_{xx} \delta p(\chi) d\chi \tag{6.12}$$

The form for the stress variation due to the perturbed material is obtained by using (6.12) put into the constitutive equation for an isotropic linear elastic material (for details see [16,

[2] Legendre's transformation and Maxwell's reciprocal

77]):

$$\delta T_{ij}(x,y) = -\sigma \int_{-\infty}^{\infty} \hat{G}_{ij}\delta p(\chi)d\chi \tag{6.13}$$

Notice that in (6.13) $\hat{G}_{ij}$ is a tensor representing a kernel function which can be derived from the Green's function, G^i_{xx}, in the following manner:

$$\hat{G}_{ij} = \frac{1}{E'}[\mu(\frac{\partial G^i_{xx}}{\partial x_j} + \frac{\partial G^j_{xx}}{\partial x_i}) + \frac{2\mu\nu\delta_{ij}}{1-2\nu}\frac{\partial G^k_{kk}}{\partial x_k}] \tag{6.14}$$

Where, in this case, δ_{ij} is the Kronecker delta, and μ is the shear modulus.

Therefore, the Green's function above can be used to find the kernel of Eq. (6.14), which in turned can be used to find the contribution of the stress due to the perturbation. Finally, this perturbation part of stress can be used to find the stress increased from the bulk stress, according to part (a) of Eq. (6.1).

Extracting the *Green's functions* G^i_{ij} from the point force solutions for a half-plane from [78], Gao derived the kernel in (6.14), which after is substituted into (6.13), gives:

$$\delta T_{xx}(x,y) = \sigma \int_{-\infty}^{\infty} \frac{2}{\pi(\chi - x)^2}\delta p(\chi)d\chi \tag{6.15}$$

and (6.15) can be substituted into (6.1) with $T^r_{ij} = \sigma$, to yield the following expression which is applicable to a first-order accuracy:

$$T_{xx} = T_{ij} = \sigma[1 + \frac{2}{\pi}\int_{-\infty}^{\infty} \frac{\delta p(\chi)d\chi}{(\chi - x)^2}] \tag{6.16}$$

using The Cauchy's Principal Value and our definition of $\delta p(\chi) = p(\chi) - p(x)$, the tangential stress component of (6.16) can be expressed as:

$$T_{xx} = \sigma[1 + \frac{2}{\pi}PV\int_{-\infty}^{\infty} \frac{(\frac{dp(\chi)}{d\chi})d\chi}{(\chi - x)}] \tag{6.17}$$

We will use (6.17) in the next section in order to derive an analytical solution for the stress

concentration factor at slightly randomly roughened surfaces for the 2-D case.

6.4 Solution to the Stress Concentration at Slightly Randomly Roughened Surfaces

The ratio of the tangential stress concentration distribution to the bulk stress—from which the desired stress concentration factor will be obtained—can be expressed, from (6.17), as:

$$k_t = \frac{T_{xx}}{\sigma} = [1 + \frac{2}{\pi} PV \int_{-\infty}^{\infty} \frac{(\frac{dp(\chi)}{d\chi})d\chi}{(\chi - x)}] \tag{6.18}$$

Furthermore, and for convenience, let $k_m = k_t - 1$, which is the ratio of stress increased locally to bulk stress, then:

$$k_m = \frac{T_{xx} - \sigma}{\sigma} = \frac{2}{\pi} PV \int_{-\infty}^{\infty} \frac{(\frac{dp(\chi)}{d\chi})d\chi}{(\chi - x)} \tag{6.19}$$

We now apply the *Hilbert transform*(HT) to (6.19). The HT is defined as follows [115]:

$$\mathfrak{H} f(t) = \hat{f(t)} = -\frac{1}{\pi} PV \int_{-\infty}^{\infty} \frac{f(\eta)d\eta}{\eta - t} = \frac{1}{\pi} PV \int_{-\infty}^{\infty} \frac{f(\eta)d\eta}{t - \eta} \tag{6.20}$$

Which is a linear operator that, contrary to *Fourier transform*, does not change the domain of the independent variable. At its core, the HT of a function f is a convolution of f with the distribution $d(t) = \frac{1}{\pi t}$, or:

$$\hat{f(t)} = (f * d)t = \int_{-\infty}^{\infty} f(\tau)d(t - \tau)d\tau \tag{6.21}$$

Applying (6.20) to (6.19), one obtains:

$$k_m = 2\mathfrak{H}(-\frac{dp(\chi)}{d\chi}) = 2\mathfrak{H}[-p^{'}(\chi)] \tag{6.22}$$

Where again, p represents a continuous, real-valued, random height having a having a

Gaussian distribution with mean zero, by definition. We then make use of the following property which indicates that the double application of HT leads to the negative of the original function:

$$\mathfrak{H}\mathfrak{H}f = -f \tag{6.23}$$

Applying HT on both sides of (6.22), and using (6.23), yields:

$$\mathfrak{H}k_m = 2[p^{'}(\chi)] \tag{6.24}$$

Obviously equation (6.24) implies that, as expected, the stress concentration factor possesses a distribution related in some manner with the distribution of the slope of the perturbed height. We will pursue the RMS value of k_m. In order to do so, let's square both sides of (6.24) and integrate with proper limits:

$$\lim_{X\to\infty}\frac{1}{X}\int_{-\frac{X}{2}}^{\frac{X}{2}}(\mathfrak{H}k_m)^2 d\chi = \lim_{X\to\infty}\frac{1}{X}\int_{-\frac{X}{2}}^{\frac{X}{2}}(2[p^{'}(\chi)])^2 = 4\lim_{X\to\infty}\frac{1}{X}\int_{-\frac{X}{2}}^{\frac{X}{2}}([p^{'}(\chi)])^2 d\chi \tag{6.25}$$

Solving equation (6.25) follows next. We will first focus our development on the right hand side of (6.25), and then explore the left hand side.

It was previously stated that our surfaces were assumed to be Gaussian, meaning that heights are normally distributed. Thus, following [116] a relationship between the root-mean-square slope, the ACL, and the root-mean-square roughness can be established.The development that follows immediately is applicable to a 3-D surface, although afterwards it will be applied to our particular 2-D case. This will be done using an exponential autocorrelation function of the form:

$$f(x,y) = s^2 e^{-\frac{x^2+y^2}{ACL^2}} \tag{6.26}$$

Where s is the standard deviation. Equation (6.26) has the same form of the Gaussian filter used for the generation of the random rough surfaces for the experimental part (see chapter 5 and references [79, 82]) against which the theoretical results obtained here are to be compared.

Let z be the surface height as a function of position along the surface. Furthermore, assume that the surface maintains its properties infinitely. Then the root-mean-square slope, m^2, is defined as:

$$m^2 = \lim_{X,Y\to\infty} \frac{1}{X}\frac{1}{Y} \int_{-\frac{X}{2}}^{\frac{X}{2}} \int_{-\frac{Y}{2}}^{\frac{Y}{2}} (\frac{\partial z}{\partial x})^2 dxdy \tag{6.27}$$

In (6.27), it has been assumed that both z^2 and $(\frac{\partial z}{\partial x})^2$ are non-infinite everywhere on the surface. Following [116] we convert (6.27) to a proper form for the application of the Parseval relation, in order to derive the desired relationship for m^2 in terms of RMS and ACL, which involves the Fourier transform of (6.26).

We initiate our conversion by a change of variables as:

$$z^* = z(x, y) \times g(x) \times h(y) \tag{6.28}$$

Where $g(x)$ and $h(y)$ control the behavior of z^* outside the regions $x \in (-X/2, X/2)$ and $y \in (-Y/2, Y/2)$.

Now, consider an expression involving the new variable z^* such that:

$$L = \lim_{X,Y\to\infty} \frac{1}{X}\frac{1}{Y} \int_{-\infty}^{\infty} \int_{-\infty}^{\infty} (\frac{\partial z^*}{\partial x})^2 dxdy \tag{6.29}$$

Where L is simply a dummy variable. (Notice the remarkable difference between (6.27) and (6.29))

Applying the change of variable (6.28) to expression (6.29):

$$L = \lim_{X,Y\to\infty} \frac{1}{X}\frac{1}{Y}\int_{-\infty}^{\infty}\int_{-\infty}^{\infty} h^2(y)[(\frac{\partial z}{\partial x})^2 g^2(x) + 2z(\frac{\partial z}{\partial x})g(x)\frac{dg(x)}{dx} + z^2(\frac{dg(x)}{dx})^2]dxdy \tag{6.30}$$

Next, we define $g(x)$ and $h(y)$ in terms of an arbitrary small constant ϵ, X, and Y, such that:

$$g(x) = \begin{cases} (\frac{X}{X+\epsilon})[(\frac{x}{\epsilon}) + (\frac{X}{2\epsilon}) + 1], & \text{for } -(X/2) - \epsilon < x < -X/2 \\ (\frac{X}{X+\epsilon}), & \text{for } |x| < X/2 \\ (\frac{X}{X+\epsilon})[-(\frac{x}{\epsilon}) + (\frac{X}{2\epsilon}) + 1], & \text{for } (X/2) < x < X/2 + \epsilon \\ 0, & \text{elsewhere} \end{cases} \tag{6.31}$$

and,

$$h(y) = \begin{cases} 1, & \text{for } |y| < Y/2 \\ 0, & \text{for } |y| > Y/2 \end{cases} \tag{6.32}$$

It can be verified that using (6.31) and (6.32) in (6.30), L becomes identical to (6.27), or:

$$m^2 = \lim_{X,Y\to\infty} \frac{1}{X}\frac{1}{Y}\int_{-\infty}^{\infty}\int_{-\infty}^{\infty} (\frac{\partial z^*}{\partial x})^2 dxdy \tag{6.33}$$

Which by Parseval's theorem becomes:

$$m^2 = \lim_{X,Y\to\infty} \frac{1}{X}\frac{1}{Y}\int_{-\infty}^{\infty}\int_{-\infty}^{\infty} [\mathfrak{F}(\frac{\partial z^*}{\partial x})(v,w)]^2 dvdw \tag{6.34}$$

Where $\mathfrak{F}$ indicates the *Fourier transform*. Additionally, by expanding $z^* = \mathfrak{F}^{-1}[\mathfrak{F}(z^*)]$, it can be extracted that:

$$\mathfrak{F}[(\frac{\partial z^*}{\partial x})(v,w)] = 2\pi i v \mathfrak{F}(z^*)(v,w) \tag{6.35}$$

Substituting (6.35) into (6.34)

$$m^2 = \lim_{X,Y\to\infty} \frac{1}{X}\frac{1}{Y}(4\pi^2) \int_{-\infty}^{\infty}\int_{-\infty}^{\infty} v^2[\mathfrak{F}(z^*)(v,w)]^2 dvdw \tag{6.36}$$

Let's analyze the integrand of (6.36). The term v^2 yields both the second moment with respect to v and the zeroth moment with respect to w. Additionally, the term $[\mathfrak{F}(z^*)(v,w)]^2$ yields the *Fourier transform* of correlation of the modified random function z^* with itself; or, better said, the FT of the autocorrelation function of z^*—$\mathfrak{F}[ACF(z^*)]$. Thus, if we call M_v^2, the second moment with respect to v, and M_w^0, the zeroth moment with respect to w, then m^2 can be expressed in terms of the $\mathfrak{F}[ACF(z^*)]$, as:

$$m^2 = (4\pi^2) M_v^2 M_w^0 \mathfrak{F}[ACF(z^*)] \tag{6.37}$$

Using the ACF given in (6.26), and substituting it in (6.37), it yields:

$$m^2 = (4\pi^2) \int_{-\infty}^{\infty}\int_{-\infty}^{\infty} v^2[s^2\pi(ACL)^2 e^{-\pi^2(ACL)^2(v^2+w^2)}]dvdw \tag{6.38}$$

Which after integration yields:

$$m^2 = 2(\frac{s}{ACL})^2 \tag{6.39}$$

The root-mean-square slope obtained in (6.39) is used in equation (6.25). By using the RMS-roughness of the surface, instead of the standard deviation in (6.39), we get the following expression:

$$\lim_{X\to\infty} \frac{1}{X} \int_{-\frac{X}{2}}^{\frac{X}{2}} (\mathfrak{H}k_m)^2 d\chi = 8(\frac{RMS}{ACL})^2 \tag{6.40}$$

Now we focus on the left hand side of equation (6.40). The following property that relates the HT with FT is used:

$$(\mathfrak{F}\mathfrak{H}f)(\omega) = -isgn(\omega)(\mathfrak{F}f)(\omega) \tag{6.41}$$

Which we apply to the left hand side of (6.40) and get:

$$\lim_{X\to\infty}\frac{1}{X}\int_{-\frac{X}{2}}^{\frac{X}{2}}(\Im k_m)^2 d\chi = \lim_{X\to\infty}\frac{1}{X}\int_{-\frac{X}{2}}^{\frac{X}{2}}(\Im^{-1}(-iS\,gn(\omega)(\Im k_m)(\omega)))^2 d\chi \tag{6.42}$$

Where $S\,gn(\omega)$ is the signum function:

$$S\,gn(\omega) = \begin{cases} 1, & \text{for } \omega > 0 \\ 0, & \text{for } \omega = 0 \\ -1, & \text{for } \omega < 0 \end{cases} \tag{6.43}$$

And $\Im^{-1}$ stands for the *Inverse Fourier Transform*. In order to apply energy conservation principles to (6.42) integration must be modified to the interval $(-\infty, \infty)$. Here we make two reasonable assumptions: that the roughened area (RA) $-X/2, X/2$ is finite, and that the integrand in (6.42) vanishes everywhere outside RA. With that said, we now notice that (6.41) implies that there is a shift change of -90 deg to every positive frequency, and a shift of 90 deg to every negative frequency. The total effects of those shifts raised to the power of two in the interval $(-\infty, \infty)$ cancels out. This also agrees with the Titchmarsh formulas of the Parseval type [117]. Therefore, (6.42) can be expressed as:

$$\lim_{X\to\infty}\frac{1}{X}\int_{-\frac{X}{2}}^{\frac{X}{2}}(\Im^{-1}(-iS\,gn(\omega)(\Im k_m)(\omega)))^2 d\chi = \lim_{X\to\infty}\frac{1}{X}\int_{-\frac{X}{2}}^{\frac{X}{2}}(k_m)^2 d\chi \tag{6.44}$$

And noticing that the left hand side of (6.44) is simply the definition of the squared of the RMS value, we get:

$$\lim_{X\to\infty}\frac{1}{X}\int_{-\frac{X}{2}}^{\frac{X}{2}}(k_m)^2 d\chi = (k_m^{RMS})^2 \tag{6.45}$$

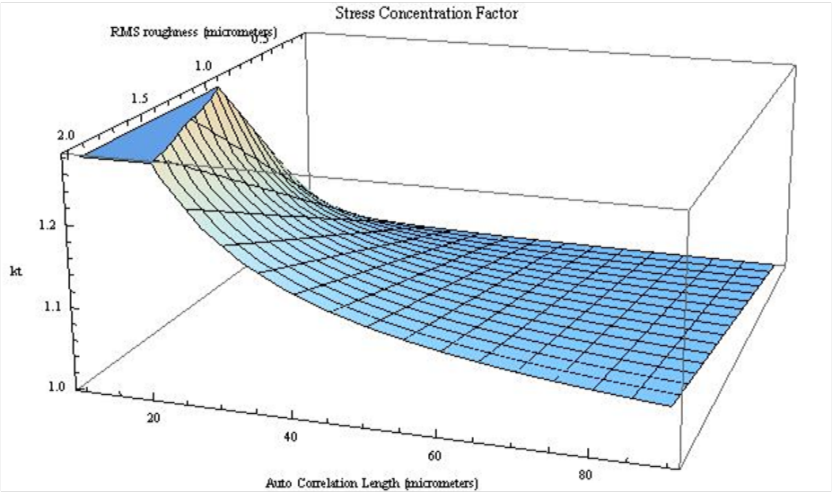

Fig. 81. Three-dimensional plot of stress concentration factor, RMS and ACL based on the derived equation (6.46)

Now, we can couple this result with the left hand side of equation (6.40) and get:

$$k_t^{RMS} = 1 + 2\sqrt{2}\frac{RMS}{ACL} \tag{6.46}$$

Recalling that $k_m + 1 = k_t$. This completes our derivation.

6.5 Comparison with experimental results

The RMS stress concentration factor equation (6.46) shows some interesting results which explain the experimental results presented in chapter 5 as well as those reported in [82], which will be discussed in this section. Since equation (6.46) was derived for conditions such that $RMS/ACL \ll 1$, then k_t^{RMS} is expected to be relatively low. For example, $RMS/ACL = 0.2$ would signify a $k_t^{RMS} = 1.57$; while for $RMS/ACL = 0.1$, $k_t^{RMS} = 1.28$. In chapter 5 it was presented that profile's RMS-roughness values were produced in the range of about $5 - 16\ \mu$ meters, and the autocorrelation length was varied from $10 - 90\ \mu$ meters. Figure 81 shows a 3-dimensional plot based on the formula of (6.46). As it is shown, k_t does not change significantly which means that the stress at fracture of a slightly

roughened surface—with the previously prescribed conditions—would not significantly differ from that of a nominally flat specimen. Figure 82 shows a plot, from experimental tests, of stress at fracture ratio (ratio of stress at fracture of a roughened surface to that of a nominally flat one) versus strain at fracture ratio. As it can be observed, the stress at fracture does not vary significantly which corroborates what is predicted by equation (6.46).

Additionally, $k_t - 1$ shows an inverse proportionality to ACL. Figure 83 shows plots of the Pearson's correlation between the fracture location probability—the probability that fracture will occur at certain profile perpendicular to the load—and the factor k_t^{RMS} as the system goes from an engineering surface (characterized by having no peaks) to a surface whose heights are normally distributed (a.k.a., Gaussian surface). Note in Figure 83 the two values of $ACL = 10, 90$. As predicted by equation (6.46), it takes much more roughness to weaken the profile that possesses larger ACL values. This is evident by noticing that despite both conditions ($ACL = 10$ and 90) reaching Gaussian distribution as the level of degradation (D) increases[82], yet, in the case of $ACL = 90$, k_t is too small—as predicted by (6.46)—to weaken the material at the profiles, thus keeping the process somewhat stochastic still.

Additionally, comparing to Gao's result for periodic sinusoidal slight surfaces[16], it is observed that for random rough profiles—having heights normally distributed—tend to relax much more than the former. For example, a sinusoidal profile with amplitude-to-wavelength ratio equal to the ratio RMS/ACL will result in a much higher stress concentration than for the random profile case. If $RMS/ACL = A/\lambda = 0.1$, for instance, then $k_t^{RMS} = 2.26$, for the periodic case, but only $k_t^{RMS} = 1.28$, for the random situation.

6.6 Modified Inglis Formula: Generalization of Inglis' result

Equation (6.46) is similar in form to Inglis' formula (IF) of the stress concentration factor. The same can be noticed for, at least, the various geometrical configurations re-

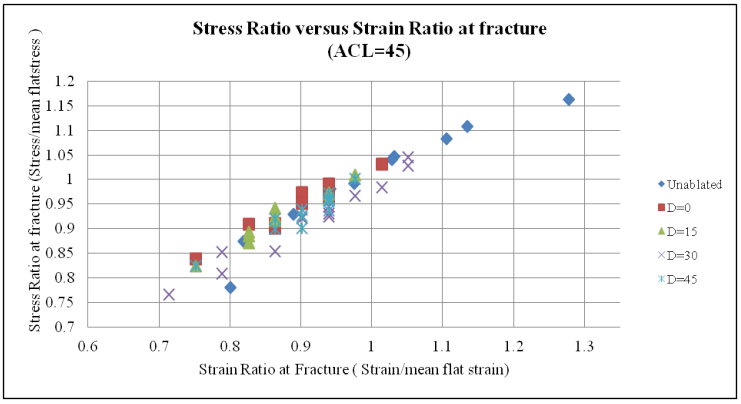

Fig. 82. Plot of flexural stress ratio vs. flexural strain ratio. It shows that stress does not decrease considerably in between the different levels of early degradation studied. The legend on the left hand side is to be read as: ”Unablated” means a flat surface; ”D = 0” means RMS =8.1 micrometers; ”D = 15” means RMS = 10.2; ”D = 30” means RMS = 12.5 micrometers; and, ”D = 45” means RMS = 15 micrometers.

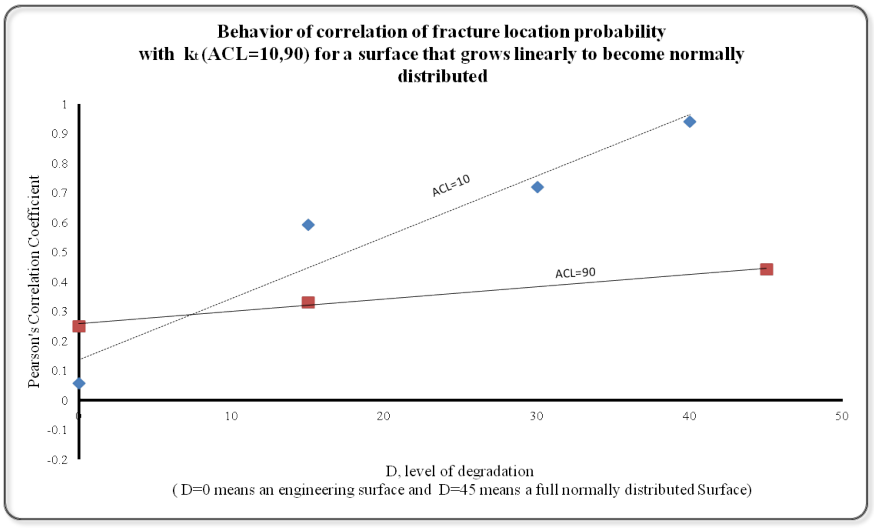

Fig. 83. Plot of Pearson’s correlation factor of fracture density versus roughness, as the surface progresses to Gaussian. ACL = 10 and 90

viewed in chapter 2. This leads us to a generalization of the IF into a proposed Modified Inglis Formula (MIF) as a unified way of estimating the stress concentration factor (SCF_n) for a variety of notch configurations. The MIF can be written as:

$$SCF_n = 1 + G\frac{A}{B} \tag{6.47}$$

Where G is a function of the geometry in question. Table 3 shows the value of G for different configurations that range from a single-notch to periodic notches, sinusoidal surfaces, and even random rough surfaces—with normally distributed heights and isotropically autocorrelated.

Table 3. Values of G from the modified Inglis Formula, for different Loading and geometrical configurations. T=Tensile, B=Bending, S=Shear.

Case	G	Geometrical and Loading Config.
I	2	U-notch (T & B)
		Elliptical-notch (T & B)
		semi-circular notch (T & B)
		Very shallow single-notch (T & B)
II	$\frac{\lambda}{\pi a}\tanh(\frac{2\pi a}{\lambda})$	Discrete,Periodic-notch (T)
III	$\frac{2\lambda}{3\pi a}\tanh(\frac{3\pi a}{\lambda})$	Discrete, periodic-notch (S)
III	4π	2-D Sinusoidal surface (T)
IV	$2\sqrt{2}(1+\nu)\pi$	3-D Sinusoidal surface (T)
V	$2\sqrt{2}$	Random Gaussian surface (T)

Table 4. Values of A and B from the modified Inglis Formula, for different geometrical configurations

Case	A	B
I	notch depth	notch width
II	any notch depth	any notch width
III	any notch depth	any notch width
III	wave amplitude	wavelength
IV	wave amplitude	wavelength
V	RMS roughness	Auto-correlation length

6.7 Discussion

Equation (6.47) in combination with Tables 3 and 4 can be used to either exactly or approximately find the respective SCF. Note that for the case of a sinusoidal surface, the MIF provides the maximum SCF located at the troughs of the wave. For the case of the random Gaussian surface, the formula gives the root-mean-squared SCF. The latter provides a "feeling" of how the stress is distributed along the surface—or profile. An actual distribution density of the SCF is currently under study by the author.

The MIF, although simple in form, shows some remarkable facts: the form of Inglis's result can be used to:

1. Predict the SCF due to a single half-elliptical or semi-circular notch, for shallow notches.

2. Approximate accurately the SCF due to a single U-notch, or most shallow notches.

3. Approximate the maximum SCF at the troughs of a sinusoidal surface.

4. Provide the root-mean-square SCF at the slightly roughened surfaces, provided that the heights of the surface are normally distributed and that the surface is isotropically auto-correlated.

However, the MIF have several limitations in terms of geometrical and loading configurations. For example, it has not been proved to apply to V-notch situations for which the opening angle is obtuse, or where the depth of the notch is not shallow. Additionally, the loading conditions are limited to mostly tensile or bending.

Another aspect worth mentioning is that, based on the values from Table 3, the geometrical function G apparently can be a constant, a function of geometry or of material properties. For finite-thickness or plane-strain conditions, one would expect G to be always a function of both geometry and material properties. Finally, further studies are recommended to strengthen confidence in the use of the MIF.

CHAPTER 7

FINITE ELEMENT SIMULATIONS

This chapter covers finite element analysis of some of the experimental work, mostly that part that coincides with the analytical study presented in chapter 6. The idea is to compare the three results whenever possible.

7.1 Building Model

In order to build up a geometrical model, we use the surfaces produced with the technique described in chapter 4. For clarity, we rewrite below the surface-producing array:

$$F_{surface} = \frac{2}{\sqrt{\pi} \cdot N \cdot ACL} L \cdot \frac{1}{N} \sum_{k=0}^{N-1} [DFT(z) \cdot DFT(g)] e^{\frac{i2\pi kn}{N}} \tag{7.1}$$

where:

N = number of grids along each axis;

ACL = auto correlation length;

L = (in this application) same as N;

DFT = Discrete Fourier Transforms, such that in equation (7.1), the two respective expressions can be written as:

$$DFT(z) = \sum_{k=0}^{N} z(n) \cdot e^{-\frac{i2\pi kn}{N}} \tag{7.2}$$

and similarly,

$$DFT(g) = \sum_{k=0}^{N} g(n) \cdot e^{-\frac{i2\pi kn}{N}} \tag{7.3}$$

Thus, surfaces produced by (7.1) were converted into xyz-format files and imported into commercially available finite element code COMSOL®. Since arrays produced by (7.1)

had constant dimensions of 600×600, then the xyz-files contained three columns of $360,000$ depth (z)values. Importation of those files was carried out using an interpolation function, which takes discrete points and interpolates as many points as necessary in order to create a smooth surface. Due to the very highly dense imported data points, linear interpolation was sufficient. Figure 84 shows four different perspectives of the same surface after importation and interpolation was carried out. Note that there is an extra edge added on two sides of the surfaces for reasons which will be later explained. Not including that extra edge, all surfaces are $12.7mm \times 12.7mm$ in the xy-dimensions; This is meant to model the real surfaces on PMMA with identical dimensions. After interpolation, surfaces

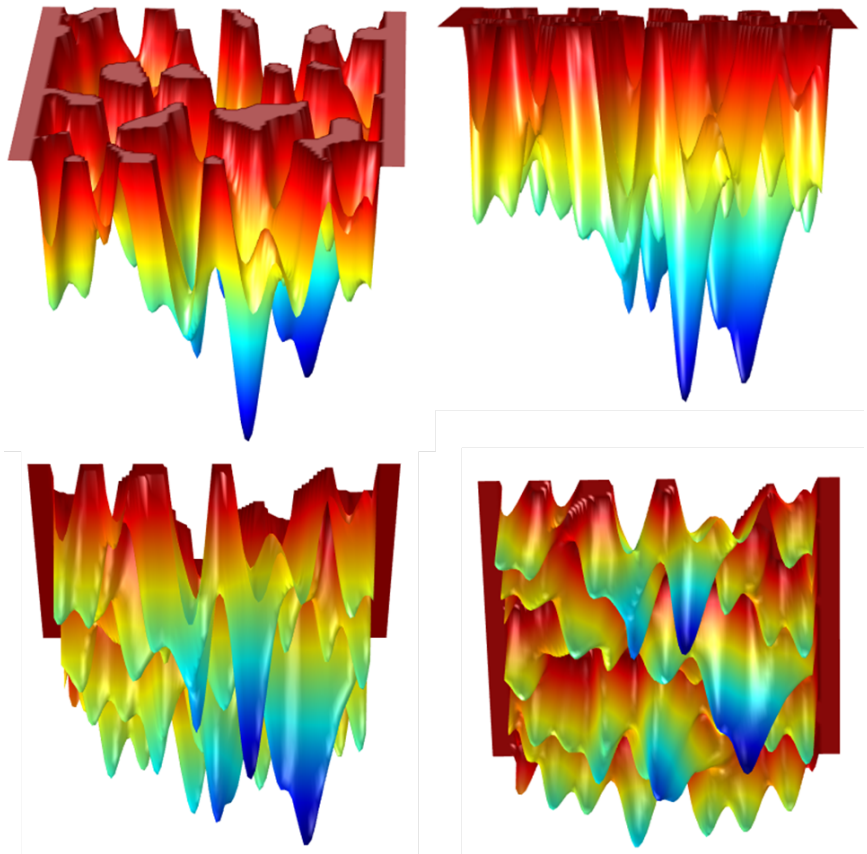

Fig. 84. Four perspective views of a surface imported into and plotted in COMSOL

were parametrized. A parametric surface is a surface in 3D where two parameters (s_1, s_2)

only are used to define the coordinates of the surface. In our case, $x = s_1$, $y = s_2$ and $z = interpolation(s_1, s_2)$. Afterwards, a solid block was created such that the bottom part of it was sufficiently below the deepest pit of the surface (at least 50μm below it). That state of affairs is shown in figure 85. Notice that the surface, although difficult to distinguish, coincides with the internal curve observed on the block. After this, the whole material was converted to a solid using the *convert to solid* feature.

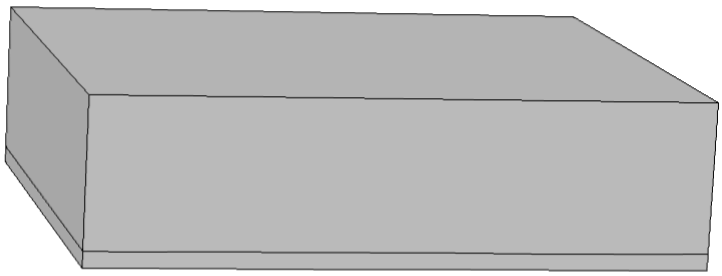

Fig. 85. Solid block that includes the parametrized surface. Note that the surface is near the bottom of the block.

Using a boolean operator (*delete entities*), the upper part of the block was subtracted from the entire solid, thus leaving a surface with a substrate underneath it. Finally, *form union* was used to convert remainder into a single entity.

7.2 Material Selection

Experimental work was carried out using PMMA with properties as given in table 5. This same properties were incorporated in our finite element model. Our material is

assumed to be elastic, isotropic and homogenous; therefore, besides density, ρ, our model is completely defined material-wise with only two properties, namely, modulus of elasticity (E) and Poisson's ratio (ν). From the materials library in COMSOL, we selected *acrylic* and put in the properties shown in table 5.

Table 5. Properties of PMMA used in the present study

Property	Value	Units
Density	1160	Kg/m^3
Modulus of elasticity	3.0	GPa
Poisson's ratio	0.38	dimensionless

7.3 Physics and Meshing

Under the *Structural Mechanics* branch and the *Solid Mechanics* interface, *linear elastic material model* was chosen. This is actually corroborated by the experimental work (recall linear elastic behavior shown in figure 13 in chapter 3). Therefore, the governing equations of generalized linear elasticity apply.

Our end goal here is to corroborate our experimental and analytical knowledge on the stress concentration due to random rough surfaces. To accomplish this, we apply a tensile load on thin films containing such surfaces. How much does this compare to the experiments? In the experimental part of this work, flexural tests were carried out. The goal of these types of tests is to reveal the impact that the surface has on the entire structure. In a flexural test, the upper outer fibers of the specimen are under compression, while the lower outer fibers are under tension. Now, let us imagine that one removes a central section of the flexural specimen at the lower outer side, as depicted in figure 86 . This piece can be thought of as

a small film with a rough surface being subjected to a tensional load, T. The magnitude of this T is irrelevant since we are mostly concern about finding the stress concentration on the surface. Thus, our model can be very well approximated using a thin film possessing

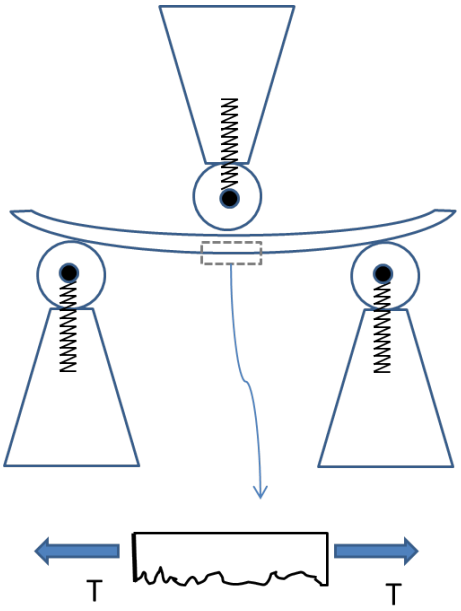

Fig. 86. In a three-point flexural test, the lower outer rough surface can be viewed as a film under tension

a random rough surface on one of its two sides and being subjected to a constant tensional load, as shown in figure 87

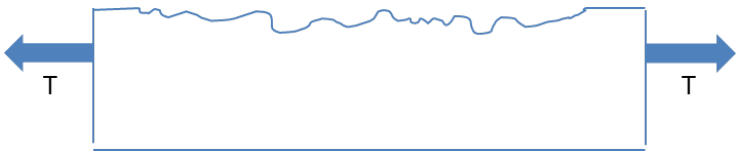

Fig. 87. A film with a rough surface subjected to a tensile load

So, boundary loads were applied to both lateral sides of the film. A free-track condition was applied on the rough side. Perhaps, the most challenging part of this model is how to agree on the boundary condition right below the film of figure 87. After trial an error

runs, the closest approximation found was that of a roller. Therefore, our final model is that shown in figure 88.

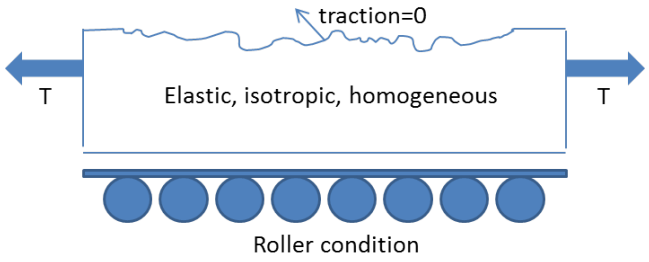

Fig. 88. Model of our surfaces, loading and boundary conditions for finite element analysis. The roller condition implies no motion in the direction normal to the plane of material. The free-traction condition is implied to be normal to the random surface.

The main justification of using the model depicted in figure 88 as opposed to the complete D790 specimen has to do with mesh limitations. Since the level of degradation is very small in comparison to the overall dimensions of the specimen, even very fine mesh does not deliver acceptable results. However, model of figure 88 offers reasonable outputs even at fine mesh level. Nonetheless, because of the random variation of surface features, a physics-controlled mesh (PCM) was selected. When PCM is selected, COMSOL examines the physics and automatically calculates size attributes and sequences operations needed to create a mesh adapted to the situation [118]. Across all models, there was an estimated average of $75,000$ mesh elements. This number is justified based on convergence plots which are shown in a later section. The elements were tetrahedral Lagrangian.

7.4 Depth Surface Plots

Surface plots were produced in COMSOL for several ACL and levels of roughness. A set of four plots corresponding to $ACL = 45$ and RMS=8.1, 10.2, 12.5 and 15 micrometers, are shown in figures 89 through 92, respectively. Notice that because of linear growth, it is assumed that all pits grow at the same rate. In the surface of figure 89, for example, it can

be observed that the maximum pit depth is around 36 micrometers, while in the one shown in figure 92 it is around 46 micrometers. Either of these maximum pits on the surface of an elastic, homogeneous material, possessing the mechanical properties of PMMA—as shown in table 5—would be enough to cause fracture at that location in a deterministic manner, in a single-pit configuration, under plane-stress conditions.

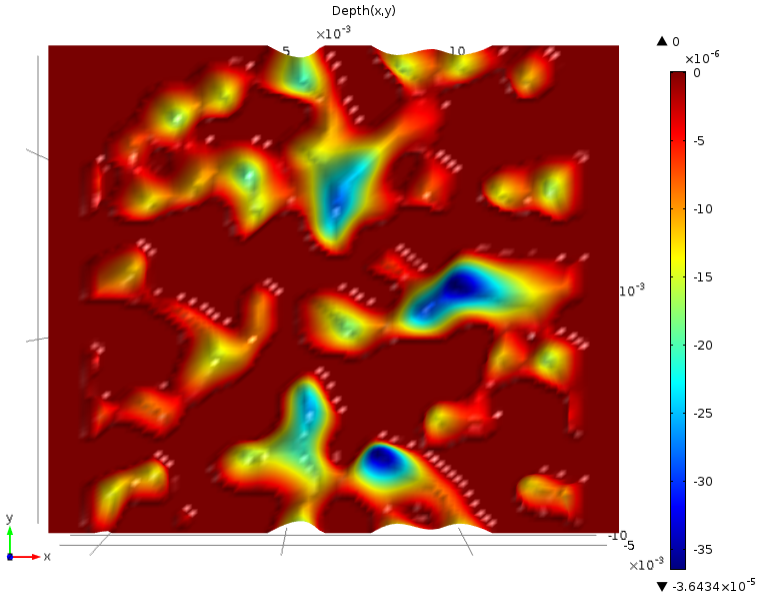

Fig. 89. FEA's surface plot for ACL = 45 and RMS = 8.1 micrometers. The maximum pit depth was around 36.4 micrometers.

7.5 Stress Concentration Surface Plots

The boundary conditions, boundary loads, and constraints described in the previous sections were applied to the model shown in figure 88. Surface plots for local stress concentration factor(LSCF) distribution were obtained. Calculation of LSCF were based on the von Mises stress criterion. Based on knowledge learned from the experimental work, it is assumed that the material is linear elastic. The LSCF are obtained as follows:

$$LSCF = \frac{\sigma^{vm}_{local}}{\sigma_{remote}} \tag{7.4}$$

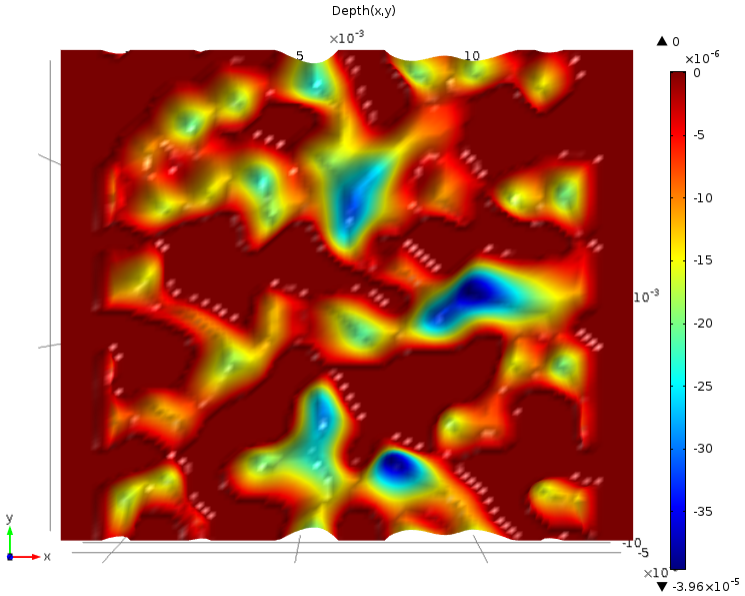

Fig. 90. FEA's surface plot for ACL = 45 and RMS = 10.2 micrometers. The maximum pit depth was around 39.6 micrometers.

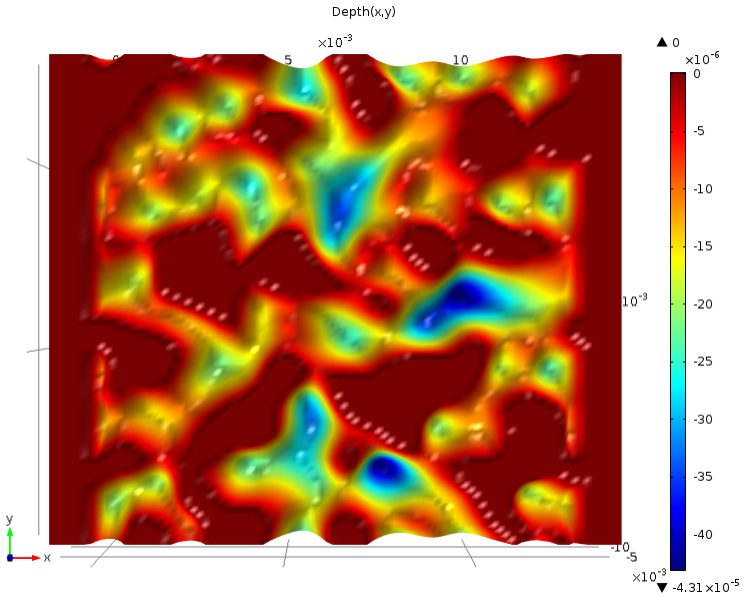

Fig. 91. FEA's surface plot for ACL = 45 and RMS = 12.5 micrometers. The maximum pit depth was around 43.1 micrometers.

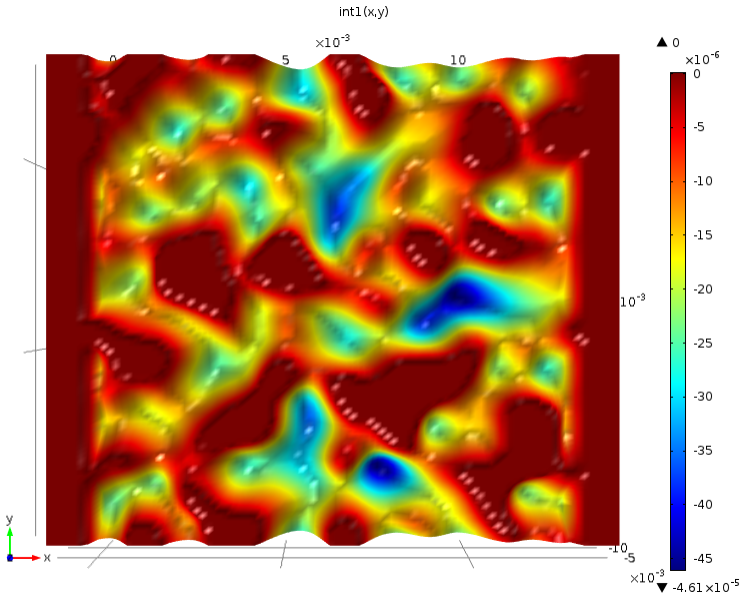

Fig. 92. FEA's surface plot for ACL = 45 and RMS = 15 micrometers. The maximum pit depth was around 46.1 micrometers.

where: σ^{vm}_{local} = Local stress based on Von Mises, and;

σ_{remote} = Stress applied at a remote location

It is well known that σ^{vm}_{local} is one the most widely accepted stress criteria for ductile materials and can be obtained from the principal stresses as:

$$\sigma^{vm}_{local} = \frac{1}{\sqrt{2}}\sqrt{(\sigma_1 - \sigma_2)^2 + (\sigma_2 - \sigma_3)^2 + (\sigma_3 - \sigma_1)^2} \tag{7.5}$$

where σ_1, σ_2, and σ_3 are the principal stresses at each local parcel on the surface. Granted, Von Mises stresses given by equation (7.5) traditionally are applied to yielding of ductile materials, but it can be applied to fracture of brittle materials when the state of stress is such that the second and third principal stresses are negligible. In our case, the latter applies. Values of the maximum principal stresses were found to be considerably much higher than the other two. For example, figures 93 and 94 contain one contour plot each for the same

surface roughness and ACL. For both simulations, the remote applied load was 1000 Pa. In the first, figure 93, the stresses were obtained based on the maximum principal stress; for the other contour plot (figure 94), the stresses were found using Von Mises (equation (7.5)). It was found that the difference at any location does not exceed 1.5%. In any case, the interest here is to find the distribution of the local stress concentration factors on the surface, thus as long as consistency is maintained, any of the two routes leads to our goal, and we have selected the Von Mises approach.

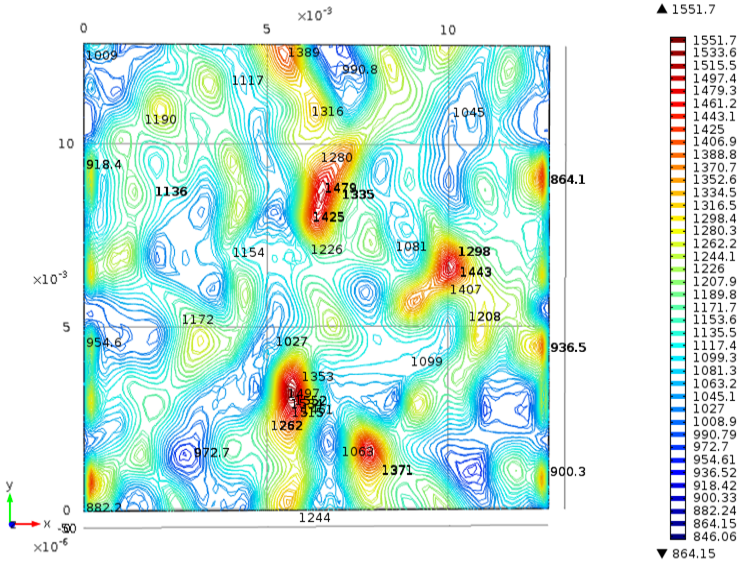

Fig. 93. Contour plot of stress distribution on the surface having ACL = 45 and RMS = 15 micrometers, using the maximum principal stress. Values are in Pa. The boundary load applied was 1,000 Pa

Figures 95, 96, 97, and 98 show contour plots of LSCF versus depth of pit for ACL=45 and various values of RMS. Note that the maximum stress concentration(k_t^{max}) for each plot. For RMS= 8.1 micrometers, k_t^{max} was found to be around 1.28 and for RMS=15 micrometers, k_t^{max} =1.53. This range of values are in the neighborhood of those observed experimentally.

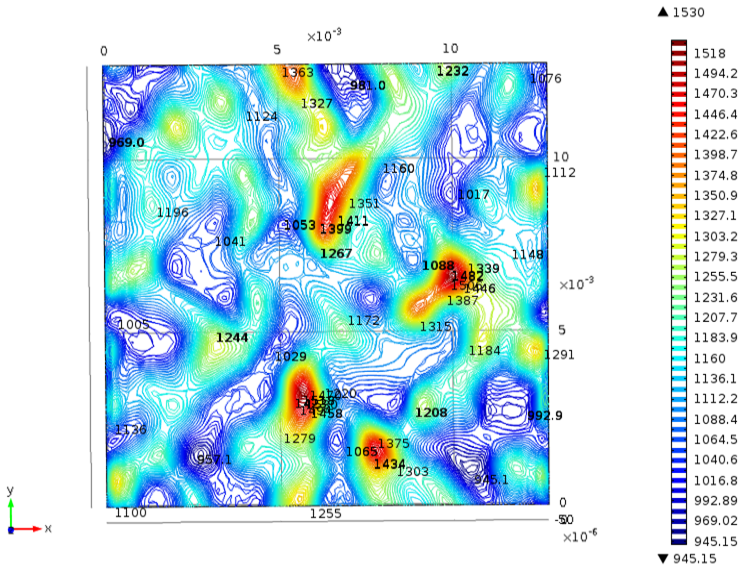

Fig. 94. Contour plot of stress distribution on the surface having ACL = 45 and RMS = 15 micrometers, using Von Mises stress. Values are in Pa. The boundary load applied was 1,000 Pa

7.6 Stress Concentration 2-D Plots

Using the data from surface plots, 2-D graphs were also produced in order to visualize the general trend of the LSCF on the surface. These plots were obtained as follows. From finite element analysis stress distribution based on Von Mises were obtained and the local stress concentration was computed using equation (7.4)). Data were exported using the *export plot* feature in COMSOL to text files. These files were then processed and plots obtained. Figures 99–102 show plots of LSCF versus depth of pit for ACL=45 at various RMS. A few observations can be concluded from these plots. First of all, as traditionally known, local stress concentration factor increases quasi-linearly with pit depth. However, a rather unexpected phenomenon is observed for the plot corresponding to RMS=15 microns, figure 102. Beyond pits of around 35 micrometers of depth, there is dual behavior of the stress concentration factor for the same value of pit depth. This implies that for after some critical degradation level, a surface can contain deep pits with low stress concentration as

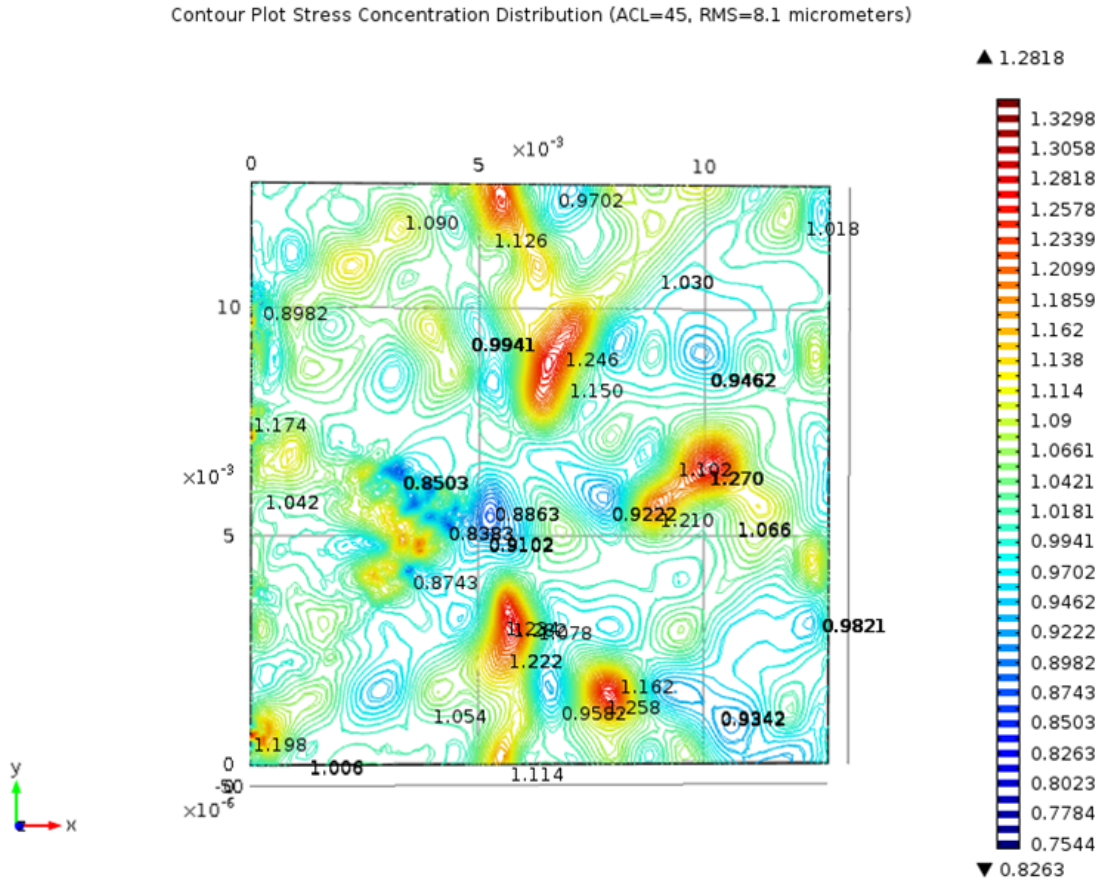

Fig. 95. FEA's contour plot of the stress concentration on a surface having ACL = 45 and RMS = 8.1 micrometers. Stress is based on Von Mises. Boundary load applied in tension was 1 KPa.

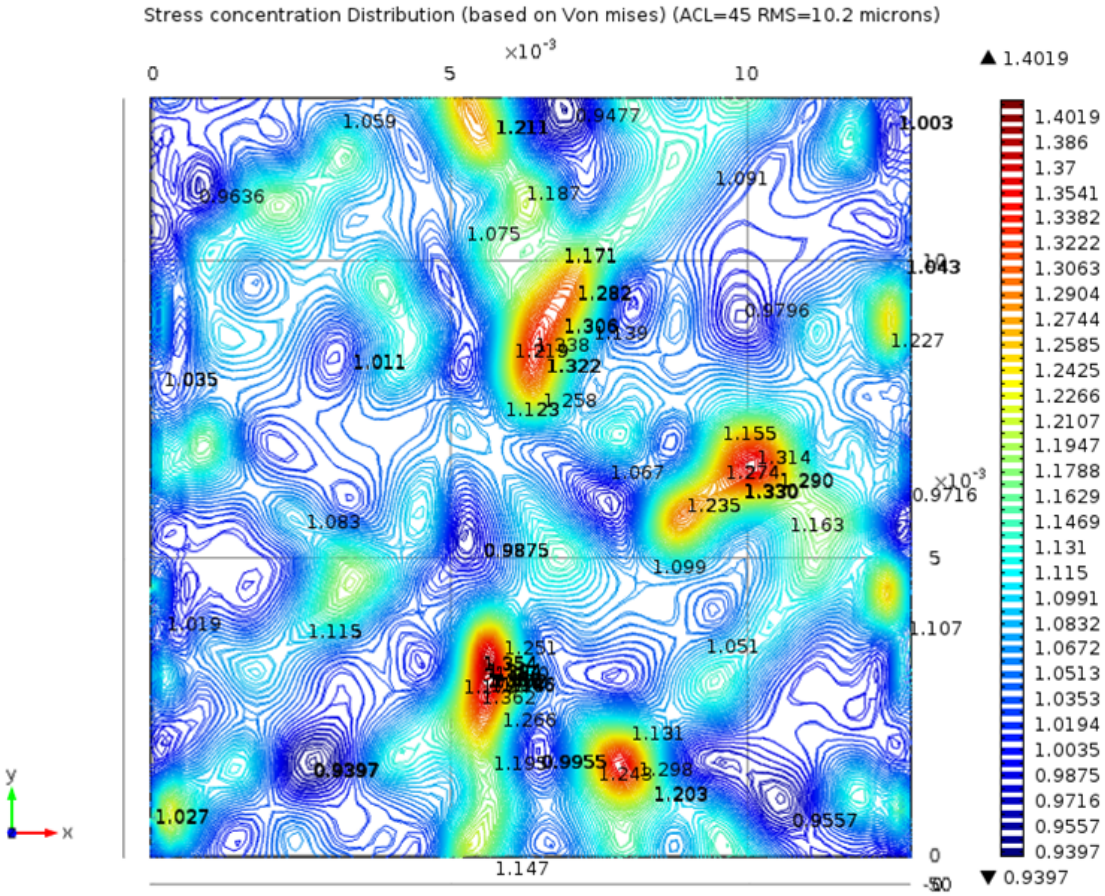

Fig. 96. FEA's contour plot of the stress concentration on a surface having ACL = 45 and RMS = 10.2 micrometers. Stress is based on Von Mises. Boundary load applied in tension was 1 KPa.

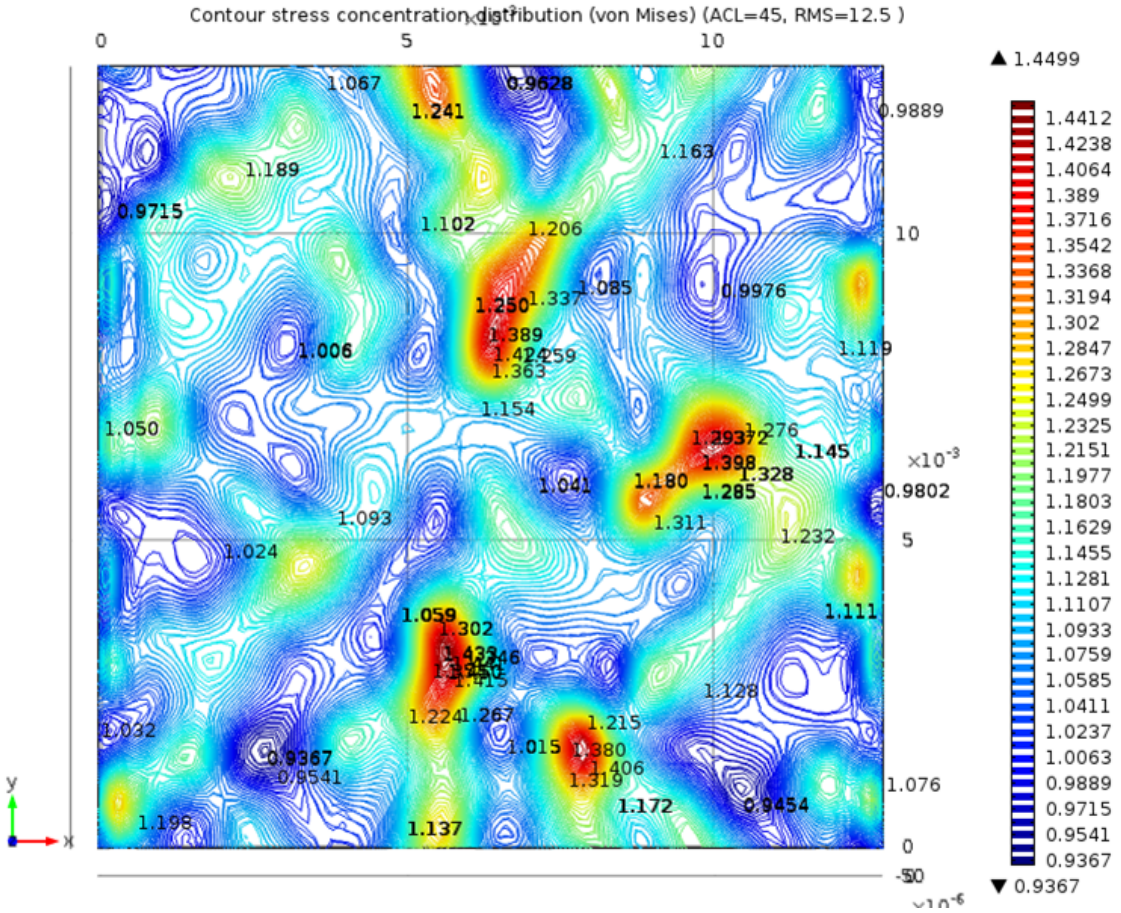

Fig. 97. FEA's contour plot of the stress concentration on a surface having ACL = 45 and RMS = 12.5 micrometers. Stress is based on Von Mises. Boundary load applied in tension was 1 KPa.

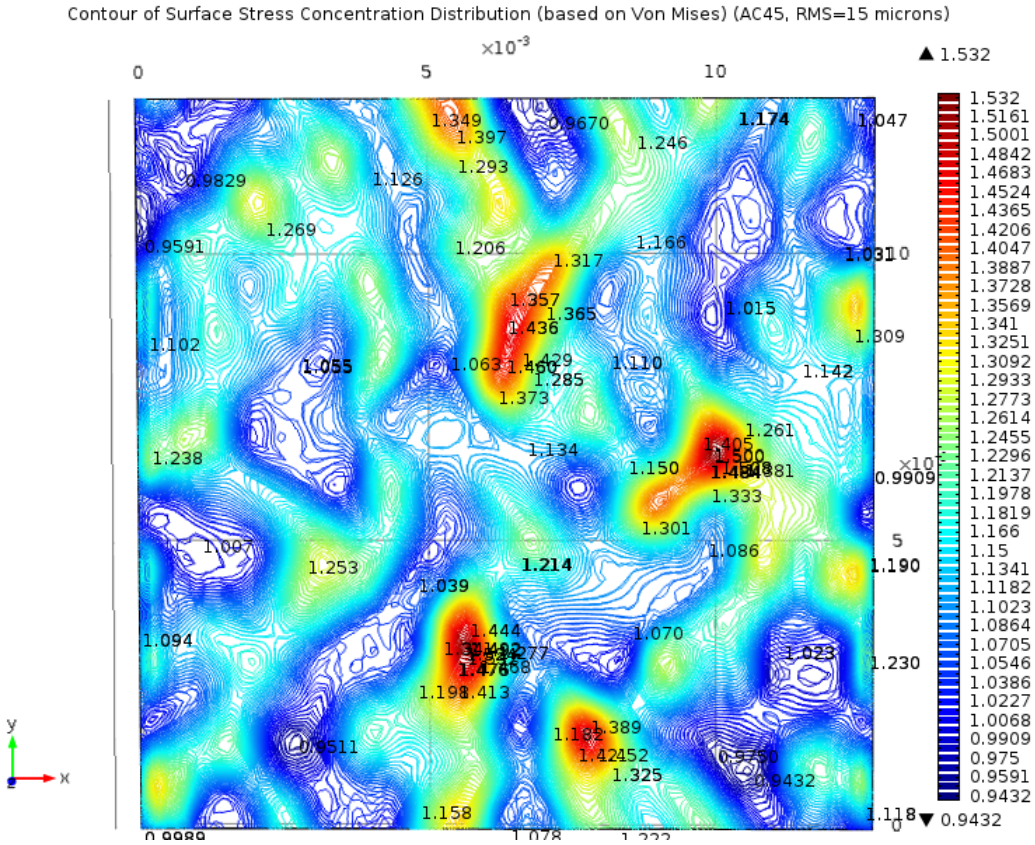

Fig. 98. FEA's contour plot of the stress concentration on a surface having ACL = 45 and RMS = 15 micrometers. Stress is based on Von Mises. Boundary load applied in tension was 1 KPa.

well as with high stress concentration. In other words, not all deep pits concentrate stress as much. In fact, there seems to be similar values of the stress concentration for deep and shallow pits for the particular case of the surface having ACL=45 and RMS=15, as shown in figure 102.

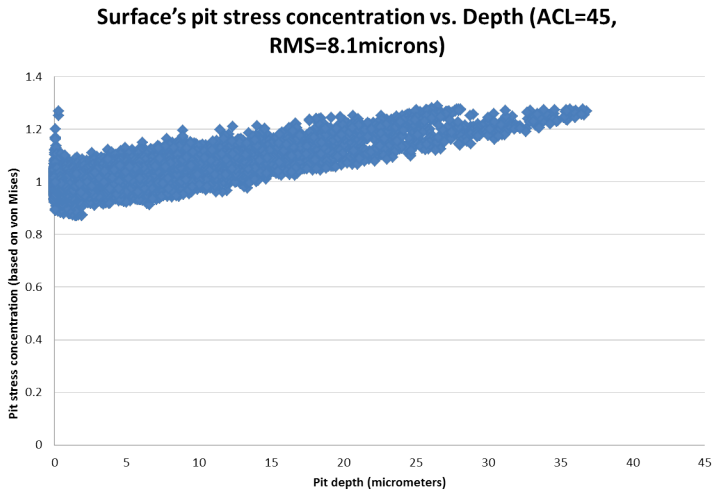

Fig. 99. Plot of local stress concentration factor on a surface vs. local depth. ACL = 45, RMS = 8.1 micrometers.

7.7 Convergence Plots

Convergence of solutions was sought using the so called H-method. This method uses simple shape functions while varying the number of mesh elements. Based on a reference (previously expected) value of a given parameter, the number of elements is increased from run to run until there is a clear convergence towards the reference value; that is, until there is very little change in the value from a run to another.

Using the aforementioned method and the maximum stress concentration factor as the reference parameter, convergence was achieved in our FEA. This state of affairs is shown in the plot of figure 103.

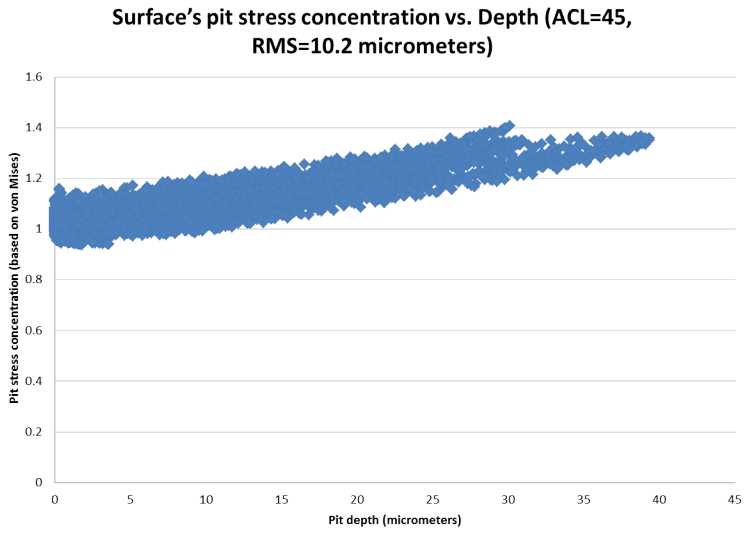

Fig. 100. Plot of local stress concentration factor on a surface vs. local depth. ACL = 45, RMS = 10.2 micrometers.

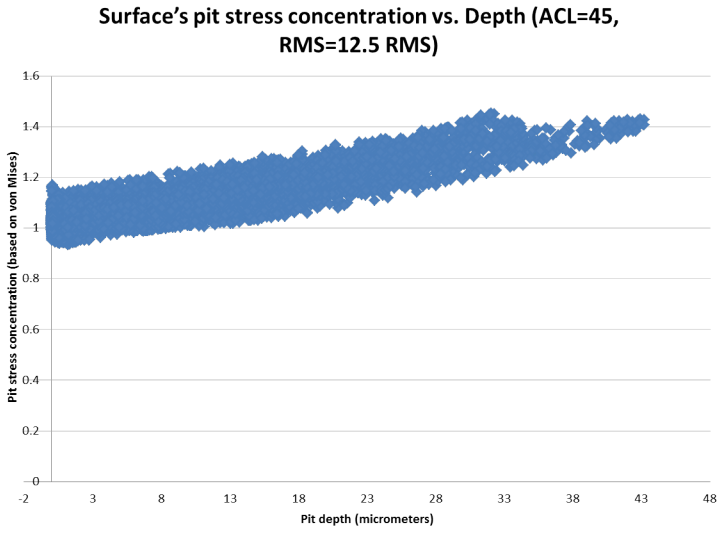

Fig. 101. Plot of local stress concentration factor on a surface vs. local depth. ACL = 45, RMS = 12.5 micrometers.

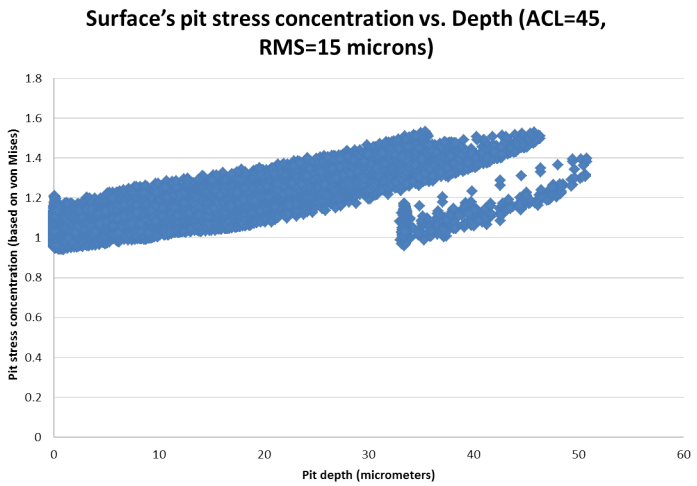

Fig. 102. Plot of local stress concentration factor on a surface vs. local depth. ACL = 45, RMS = 15 micrometers. Note the double trend at pits deeper than about 35 micrometers

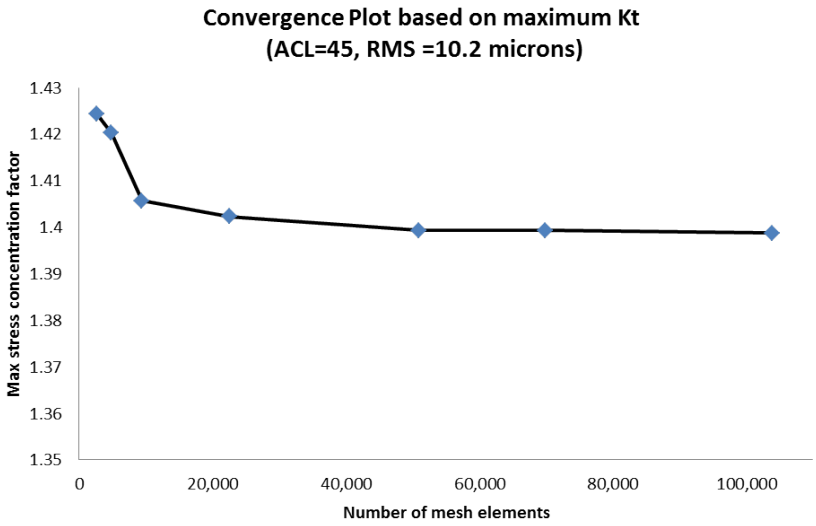

Fig. 103. Convergence plot using the stress concentration factor as the reference parameter. As it can be observed after 50,000 tetrahedral elements the maximum stress concentration factor clearly converges to around 1.4, for a particular surface.

7.8 Comparison with Experimental and Analytical Results

A logical step to take is to compare the present results for the SCF found via FEA against the values obtained from both experimental and analytical means. Figure 104 shows a comparison of the stress at fracture based on experimental versus FEA results. As one can verily notice the results agree very well. The values of the stress at fracture for FEA, σ_{FEA} were calculated using the following relationship:

$$\sigma_{FEA} = \frac{\sigma_{flat}}{k_{FEA}^{MAX}} \tag{7.6}$$

where σ_{flat} = stress at fracture for a nominally flat specimen, and k_{FEA}^{MAX} is the maximum stress concentration based on Von Mises from FEA.

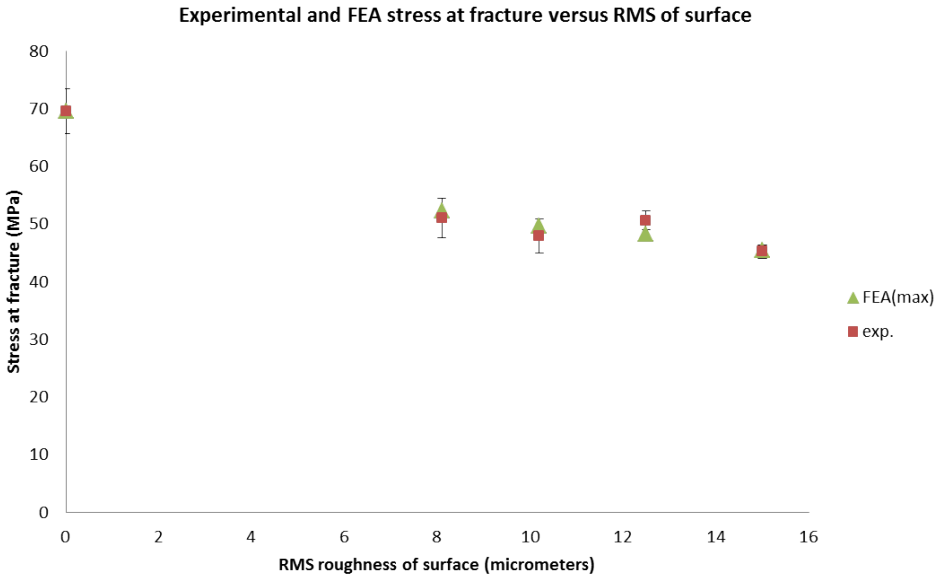

Fig. 104. Plot showing a comparison of some experimental values against Finite Element Analysis

Additionally, figure 105 shows a comparative plot similar to that figure 104 but including values obtained from the analytical solution derived in chapter 6. The theoretical

stress at fracture was calculated via the following relationship that counts on the theoretical stress concentration factor derived before:

$$\sigma_{theory} = \frac{\sigma_{flat}}{k_{theory}} = \frac{\sigma_{flat}}{1 + 2\sqrt{2}\frac{RMS}{ACL}} \tag{7.7}$$

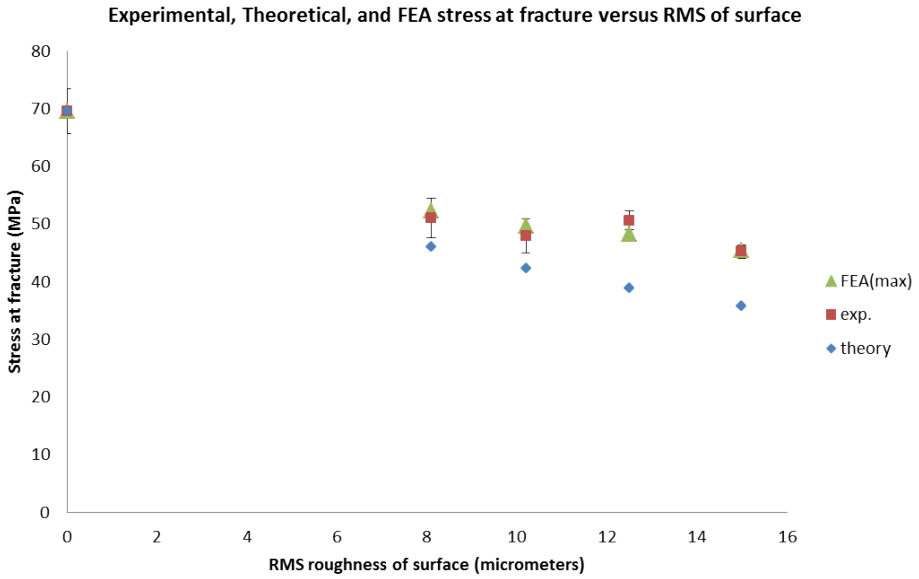

Fig. 105. Plot showing a comparison of some experimental values against Finite Element Analysis

7.9 Discussion and Conclusion of FEA

Finite element analysis has been carried out in order to bring in other means of understanding and corroborating our experimental and analytical work. The model considered assumes that a small strip is taken off from the outer fibers in tension from a three-point flexural test. Under the strip a roller condition was applied and the rough surface was considered free of tractions. Isotropic, elastic, homogeneous conditions were assumed.

- Contour plots of distribution of local stress concentration factors based on Von Mises stress were developed for several surfaces.

- The values of the maximum stress concentration factor was found to be very similar to that found from the experimental work.
- Comparison of stress at fracture for experimental work against FEA results show strong agreement.
- Comparison of FEA stress at fracture against its theoretical counterpart, show initially some agreement for small RMS but deviation was observed for higher values of RMS.
- Convergence was obtained via the H-method and using the maximum stress concentration factor (or similarly the maximum Von Mises from the stress distribution).

Appendix A

LIST OF PUBLICATIONS

Journal Papers

- Medina, H. and Hinderliter, B., The Stress Concentration Factor for Slightly Roughened Random Surfaces: Analytical Solution. International Journal of Solids and Structures (2014), Vol. 51, pp. 2012-2018.

- Medina, H., Pidaparti, R., Hinderliter, B., Celebrating the 100th Anniversary of Inglis Result: from Single Notch to Rough Surface Stress Concentration Solutions. Applied Mechanics Reviews. Accepted May 2014.

- Medina, H., and Hinderliter, B., Use of Poly Methyl (Methacrylate) in the Study of Fracture of Randomly Damaged Surfaces: I. Experimental Approach. Polymer (2012), Vol. 53, pp. 4525-4532.

- Medina, Hector, and Hinderliter Brian, Method for Generating and Realizing Replicates of Randomly Roughened Surfaces, Tested on Poly Methyl (Methacrylate), Experimental Techniques (2013), Wiley.

- Medina, H. and Hinderliter, B., Stress, Strain, and Energy at Fracture of Degraded Surfaces: Study of Replicates of Rough Surfaces . J. Eng. Gas Turbines Power (2013).

- Medina, Hector, and Hinderliter, Brian, Where do Random Rough Surfaces Fail? Part I: Fracture Loci Safety Envelopes at Early Stages of Degradation. Journal of Energy and Power Engineering 7 (2013) pp. 907-916.

Peer-Reviewed Proceedings Papers

- Medina, H., and Hinderliter, B., Generation and Mechanical Analysis of Repeatable Random Rough Surfaces, Proceedings of the ASMEs ICONE20POWER 2012 International Conference, held in Anaheim, CA.

- Medina, H., and Hinderliter, B., Stress, Strain and Energy at Fracture of Degraded Surfaces. Proceedings of ASMEs ICONE21 International Conference 2013, held in Chengdu, China.

- Medina, H., and Hinderliter, B., The Experience of Being Educated in a New Nuclear Program. Proceedings of ASMEs ICONE21 International Conference 2013, held in Chengdu, China.

Appendix B

PSEUDO CODE USED TO DEVELOP DIGITAL SURFACES

Declare: All variables

$x = linspace(-rL/2, rL/2, N);$

$y = linspace(-rL/2, rL/2, N);$

$[X, Y] = meshgrid(x, y);$

$Z = h. * randn(N, N);$

$F = exp(-((X.^2 + Y.^2)/(clx^2/2)));$

fBergstrom = 2/ $\sqrt{(\pi)}$*rL/N/clx*ifft2(fft2(Z).*fft2(F));

Arraymain=fBergstrom;

Begin loop A for j=0 to number of surfaces, increased by 1

$fBergstrom(j) = fBergstrom + j * steps;$

End loop A

Begin loop B for i=0 to 45, increasing i by steps

$Array1 = (fBergstrom > 0). * fBergstrom;$

$Arrayi = ((fBergstrom + i) > 0). * (fBergstrom + 1);$

End loop B

Appendix C

ON THE HILBERT TRANSFORM

This appendix contains a definition, properties and some well known solutions of the Hilbert Transform (HT). For more details one could refereed to specialized literature such as [115, 119].

C.1 Definition

In its most elementary form, the HT of a function, $f(\eta)$, is defined as the convolution between f and the distribution $1/t$, or:

$$\mathfrak{H}f(t) = \hat{f(t)} = -PV \int_{-\infty}^{\infty} \frac{f(\eta)d\eta}{\eta - t} = PV \int_{-\infty}^{\infty} \frac{f(\eta)d\eta}{t - \eta} \tag{C.1}$$

Which is a linear operator that, contrary to *Fourier transform*, does not change the domain of the independent variable. Traditionally for convenience a factor of $1/\pi$ is prefixed, and thus equation (C.1) can be rewritten as:

$$\mathfrak{H}f(t) = \hat{f(t)} = -\frac{1}{\pi} PV \int_{-\infty}^{\infty} \frac{f(\eta)d\eta}{\eta - t} = \frac{1}{\pi} PV \int_{-\infty}^{\infty} \frac{f(\eta)d\eta}{t - \eta} \tag{C.2}$$

In both (C.1) and (C.2) *PV* stands for *Cauchy's Principal Value* and therefore the integral is to be evaluated in such a sense.

C.2 Properties

C.2.1 Inverse

The inverse HT of a function g, $\mathfrak{H}^{-1}$, is defined as:

$$\mathfrak{H}^{-1}g = -\mathfrak{H}\mathfrak{H}g \tag{C.3}$$

So the inverse HT, or the negative of the double application of the HT returns the original function.

C.2.2 Complex Conjugation Property

The HT operator commutes with complex conjugation:

$$(\mathfrak{H}f^*) = (\mathfrak{H}f)^* \tag{C.4}$$

where * denotes the complex conjugate operation

C.2.3 Linearity

The HT operator is linear. For constants γ and κ which are allowed to be complex, and functions f and g, linearity implies that:

$$\mathfrak{H}f[\gamma f(x) + \kappa g(x)] = \gamma\mathfrak{H}f(x) + \kappa\mathfrak{H}g(x) \tag{C.5}$$

C.2.4 Hilbert Transform of Derivative

The HT of the derivative of a function is the derivative of the HT of the function, or:

$$\mathfrak{H}[\frac{d^n f(x)}{x^n}] = \frac{d^n}{x^n}\mathfrak{H}(f(x)) \tag{C.6}$$

C.2.5 Hilbert Transform and Fourier Transform Connection

The HT and the Fourier Transform (FT) are related through the following formula:

$$\mathfrak{F}\mathfrak{H}f(x) = -iSgnx\mathfrak{F}f(x) \tag{C.7}$$

where $\mathfrak{F}$ denotes the FT;

$i = \sqrt{(-1)}$, that is, the imaginary i;

Sgn is the Signum function such that:

$$Sgn(x) = \begin{cases} 1, & \text{for } x > 0 \\ 0, & \text{for } x = 0 \\ -1, & \text{for } x < 0 \end{cases} \tag{C.8}$$

C.3 Selected Functions and their Hilbert Transforms

Table 6. Selected pair of functions and their respective HT

Function	HT
$\sin(\pi x)$	$-\cos(\pi x)$
$\cos(\pi x)$	$\sin(\pi x)$
$\sin^2(\pi x)$	$-\frac{1}{2}\sin(2\pi x)$
$\frac{x+a}{(x+a)^2+b^2}, b > 0$	$-\frac{b}{(x+a)^2+b^2}$
e^{iax}	$-iSign(a)e^{iax}$

Bibliography

[1] Norman E Dowling. *Mechanical behavior of materials: engineering methods for deformation, fracture, and fatigue*. prentice Hall, 1993.

[2] Ted L Anderson. *Fracture mechanics: fundamentals and applications*. CRC press, 2005.

[3] WD Piley. *Petersons stress concentration factors*. 1997.

[4] Smith J.H. Christ B.W. Reed R.P. *Economic effects of fracture in the United States. Part1. A synopsis of the September 30,1982 report to NBS by Battelle Columbus Laboratories*. Tech. rep. NTIS.

[5] J.J. Duga and Battelle Columbus Laboratories. *The Economic Effects of Fracture in the United States: A report to NBS by Battelle Columbus Laboratories*. National Bureau of Standards special publication pt. 2. National Bureau of Standards, 1983.

[6] Faria L. *The economic effect of fracture in Europe. Final report of European Atomic Energy Community*. Tech. rep. European Atomic Energy Community.

[7] Sun L. Dubouski S. Durand J. Heripre E. *Crack propagation, Wear and Rough Surfaces: Contact Mechanics II. Solid Mechanics Laboratory*. Ecole Polytechnique ParisTech.

[8] H. Jiang, P. Bowen, and J.F. Knott. "Fatigue performance of a cast aluminium alloy Al-7Si-Mg with surface defects". English. In: *Journal of Materials Science* 34.4 (1999), pp. 719–725. ISSN: 0022-2461.

[9] Ted M. Zobeck and C.A. Onstad. "Tillage and rainfall effects on random roughness: A review". In: *Soil and Tillage Research* 9.1 (1987), pp. 1 –20. ISSN: 0167-1987.

[10] J.B.P. Williamson. “The shape of Surfaces”. In: *CRC Handbook of Lubrication, volume II*. Ed. by R.B. Bruce. Boca Raton, Florida: CRC Press, 1983.

[11] BNJ Persson and S Gorb. “The effect of surface roughness on the adhesion of elastic plates with application to biological systems”. In: *The Journal of chemical physics* 119.21 (2003), pp. 11437–11444.

[12] Guang Lin, C-H Su, and George Em Karniadakis. “Stochastic modeling of random roughness in shock scattering problems: theory and simulations”. In: *Computer Methods in Applied Mechanics and Engineering* 197.43 (2008), pp. 3420–3434.

[13] Prasanta Sahoo. *Engineering tribology*. PHI Learning Pvt. Ltd., 2005.

[14] Andrew W Batchelor, Loh Nee Lam, and Margam Chandrasekaran. *Materials degradation and its control by surface engineering*. Vol. 119. World Scientific, 2002.

[15] IAEA. *ReportsIntegrity of Reactor Pressure Vessels in Nuclear Power Plants: Assessment of Irradiation Embrittlement Effects in Reactor Pressure Vessel Steels*. Tech. rep. International Atomic Energy Agency.

[16] Huajian Gao. “Stress concentration at slightly undulating surfaces”. In: *Journal of the Mechanics and Physics of Solids* 39.4 (1991), pp. 443–458.

[17] Yu I Vikulina, MA Grekov, and SA Kostyrko. “Model of film coating with weakly curved surface”. In: *Mechanics of Solids* 45.6 (2010), pp. 778–788.

[18] Hector E Medina and Brian Hinderliter. “Where do Random Rough Surfaces Fail? Part I: Fracture Loci Safety Envelopes at Early Stages of Degradation”. In: *Journal of Energy and Power Engineering* 7 (2013), pp. 907–916.

[19] Jorge Alberto Arismendi et al. “Machined versus rough surface implants, a clinical study: 36-month follow-up”. In: *Revista Facultad de Odontologia Universidad de Antioquia* 21.2 (2010), pp. 159–169.

[20] Roberson MJ. Prats LM. “Preventing fractures in implant pported removable dentures”. In: *Dent Today* 29.12 (2010), pp. 100–102.

[21] O Ergincan, G Palasantzas, and BJ Kooi. “Influence of random roughness on cantilever curvature sensitivity”. In: *Applied physics letters* 96.4 (2010), pp. 041912–041912.

[22] O Ergincan and G Palasantzas. “Influence of random roughness on cantilever resonance frequency”. In: *Physical Review B* 82.15 (2010), p. 155438.

[23] Jorg Weissmuller and Huiling Duan. “Cantilever bending with rough surfaces”. In: *Physical review letters* 101.14 (2008), p. 146102.

[24] Brian Hinderliter and Stuart Croll. “Predicting Coating Failure using the Central Limit Theorem and Physical Modeling”. In: *ECS Transactions* 24.1 (2010), pp. 1–26.

[25] J Graystone. “Mathematical Implications of Service Life Prediction in the Coatings Industry”. In: *Service Life Prediction, Federation of Societies for Coatings Technology* (2005).

[26] KT Gillen, MC Celina, and R Bernstein. “Methods for predicting lifetimes and remaining lifetimes of polymers”. In: *Service Life Prediction, Federation of Societies for Coatings Technology* (2005).

[27] V Rasouli and JP Harrison. “Assessment of rock fracture surface roughness using Riemannian statistics of linear profiles”. In: *International Journal of Rock Mechanics and Mining Sciences* 47.6 (2010), pp. 940–948.

[28] TH Huang, CS Chang, and CY Chao. “Experimental and mathematical modeling for fracture of rock joint with regular asperities”. In: *Engineering Fracture Mechanics* 69.17 (2002), pp. 1977–1996.

[29] Zongfu Yu, Aaswath Raman, and Shanhui Fan. “Fundamental limit of nanophotonic light trapping in solar cells”. In: *Proceedings of the National Academy of Sciences* 107.41 (2010), pp. 17491–17496.

[30] MM Shalabi et al. “Implant surface roughness and bone healing: a systematic review”. In: *Journal of dental research* 85.6 (2006), pp. 496–500.

[31] JW Martin, T Nguyen, and KA Wood. “Unresolved Issues Related to Predicting the Service Life of Polymeric Materials”. In: *Service Life Prediction: Challenging the Status Quo* (2005), p. 13.

[32] Mehdi Tofighi Naeem et al. “Failure analysis of gas turbine blades”. In: *proceedings of the 2008 IAJC-IJME international conference. ISBN*. 2008, pp. 978–1.

[33] Jonathan W Martin, Rose A Ryntz, and Ray A Dickie. “Service life prediction: challenging the status quo”. In: (2005).

[34] H Neuber and HG Hahn. “Stress concentration in scientific research and engineering”. In: *Appl. Mech. Rev* 19.3 (1966), pp. 187–199.

[35] GV Kolosov. “On an application of complex function theory to a plane problem of the mathematical theory of elasticity”. In: *Yuriev, Russia* (1909).

[36] Charles Edward Inglis. “Stresses in a plate due to the presence of cracks and sharp corners”. In: *Transactions of the Institute of Naval Architects* 55 (1913), pp. 219–241.

[37] B Hopkinson. “Collected scientific papers”. In: *University Press, Cambridge* 2 (1921), pp. 555–560.

[38] AA Griffith. “VI. The Phenomena of Rupture and F low in Solids.” In: *Phil. Trans. Roy. Soc.(Lon.) A* 221 (1920), pp. 163–198.

[39] M de Saint-Venant. *Mémoire sur la torsion des prismes: avec des considérations sur leur flexion ainsi que sur l'équilibre intérieur des solides élastiques en général: et des formules pratiques pour le calcul de leur résistance à divers efforts s' exerçant simultanément*. Imprimerie nationale, 1856.

[40] George R Irwin. “Analysis of stresses and strains near the end of a crack traversing a plate”. In: *J. appl. Mech.* (1957).

[41] SJ Hardy and NH Malik. “A survey of post-Peterson stress concentration factor data”. In: *International journal of fatigue* 14.3 (1992), pp. 147–153.

[42] NA Noda and Y Takase. “Stress concentration factor formulas useful for all notch shapes in a flat test specimen under tension and bending”. In: *Journal of testing and evaluation* 30.5 (2002), pp. 369–381.

[43] Nao-Aki Noda and Yasushi Takase. “Stress concentration formula useful for all notch shape in a round bar (comparison between torsion, tension and bending)”. In: *International journal of fatigue* 28.2 (2006), pp. 151–163.

[44] Zheng Yang et al. “The concentration of stress and strain in finite thickness elastic plate containing a circular hole”. In: *International Journal of Solids and Structures* 45.3 (2008), pp. 713–731.

[45] Xueping Li et al. “Measurement for fracture toughness of single crystal silicon film with tensile test”. In: *Sensors and Actuators A: Physical* 119.1 (2005), pp. 229–235.

[46] RJ Grant, M Lorenzo, and J Smart. “The effect of Poisson’s ratio on stress concentrations”. In: *The Journal of Strain Analysis for Engineering Design* 42.2 (2007), pp. 95–104.

[47] Stephen P Timoshenko and James M Gere. *Theory of elastic stability*. Courier Dover Publications, 2012.

[48] J Dundurs. “Dependence of stress on Poisson’s ratio in plane elasticity”. In: *International Journal of Solids and Structures* 3.6 (1967), pp. 1013–1021.

[49] Engineering Scientific Data Unit. *Elastic stress concentration factors, geometric discontinuities in rods and tubes of isotropic materials*. Tech. rep. ESDU.

[50] L Morris et al. “Experimental assessment of stress patterns in abdominal aortic aneurysms using the photoelastic method”. In: *Strain* 40.4 (2004), pp. 165–172.

[51] Warren Clarence Young and Richard Gordon Budynas. *Roark’s formulas for stress and strain*. Vol. 7. McGraw-Hill New York, 2002.

[52] H Neuber. “Kerbspannungslehre, 1958”. In: *Berlin/Heidelberg, Gottingen* (1950).

[53] B Atzori, P Lazzarin, and G Meneghetti. “Fracture mechanics and notch sensitivity”. In: *Fatigue & Fracture of Engineering Materials & Structures* 26.3 (2003), pp. 257–267.

[54] AH Cottrell. “The 1963 Tewkesbury Lecture”. In: *University of Melbourne, Australia* ().

[55] JW Hutchinson. “Singular behaviour at the end of a tensile crack in a hardening material”. In: *Journal of the Mechanics and Physics of Solids* 16.1 (1968), pp. 13–31.

[56] MF Ashby. “Work hardening of dispersion-hardened crystals”. In: *Philosophical Magazine* 14.132 (1966), pp. 1157–1178.

[57] Lin Xia and C Fong Shih. “Ductile crack growth-I. A numerical study using computational cells with microstructurally-based length scales”. In: *Journal of the Mechanics and Physics of Solids* 43.2 (1995), pp. 233–259.

[58] K Sieradzki and RC Newman. “Brittle behavior of ductile metals during stress-corrosion cracking”. In: *Philosophical Magazine A* 51.1 (1985), pp. 95–132.

[59] Z. Suo, S. Ho, and X. Gong. “Notch ductile-to-brittle transition due to localized inelastic band”. In: *Journal of engineering materials and technology* 115.3 (1993), pp. 319–326.

[60] Alexander S Balankin et al. “Stress concentration and size effect in fracture of notched heterogeneous material”. In: *Physical Review E* 83.1 (2011), p. 015101.

[61] John M Hedgepeth. *Stress concentrations in filamentary structures*. Tech. rep. DTIC Document, 1961.

[62] John M Hedgepeth and Peter Van Dyke. “Local stress concentrations in imperfect filamentary composite materials”. In: *Journal of composite materials* 1.3 (1967), pp. 294–309.

[63] WB Fichter. *Stress Concentrations in Filament-Stiffened Sheets of Finite Length.* Tech. rep. DTIC Document, 1970.

[64] Harold G Franklin. “Hole stress concentrations in filamentary structures”. In: *Fibre Science and Technology* 2.3 (1970), pp. 241–249.

[65] Jerzy T Pindera. “Actual three-dimensional stresses in notches, crack tips and lamination planes”. In: *Composites Part B: Engineering* 30.2 (1999), pp. 189–203.

[66] Carl Zweben. “An approximate method of analysis for notched unidirectional composites”. In: *Engineering Fracture Mechanics* 6.1 (1974), pp. 1–10.

[67] Fu-Kuo Chang and Kuo-Yen Chang. “A progressive damage model for laminated composites containing stress concentrations”. In: *Journal of Composite Materials* 21.9 (1987), pp. 834–855.

[68] Peter Van Dyke and John M Hedgepeth. “Stress concentrations from single-filament failures in composite materials”. In: *Textile Research Journal* 39.7 (1969), pp. 618–626.

[69] Hiroshi Fukuda and Kozo Kawata. “On the stress concentration factor in fibrous composites”. In: *Fibre Science and Technology* 9.3 (1976), pp. 189–203.

[70] MP Savruk and A Kazberuk. “Stresses in an elastic plane with periodic system of closely located holes”. In: *Materials Science* 45.6 (2009), pp. 831–844.

[71] Hironobu NISITANI. “Method of approximate calculation for interference of notch effects and its application”. In: *Bulletin of JSME* 11.47 (1968), pp. 725–738.

[72] GN Savin. “Distribution of Stresses Near Holes”. In: *Naukova Dumka, Kiev* (1968).

[73] N. Mironenko. “Periodic and doubly periodic plane problems of the theory of elasticity for domains with curvilinear holes”. In: *Prikl. Mekh.* 24.6 (1988), pp. 91–97.

[74] Roland Bryon Heywood. *Designing by photoelasticity*. Chapman & Hall, 1952.

[75] D Castagnetti and E Dragoni. “Stress concentrations in periodic notches: a critical investigation of Neuber’s method”. In: *Materialwissenschaft und Werkstofftechnik* 44.5 (2013), pp. 364–371.

[76] C. Belotserkovskii and I. Lifanov. “Numerical Methods in Singular Integral Equations [in Russian]”. In: *Moscow Izdatel’stvo Nauka* (1985), 256 p.

[77] Huajian Gao. “A boundary perturbation analysis for elastic inclusions and interfaces”. In: *International Journal of Solids and Structures* 28.6 (1991), pp. 703–725.

[78] AE Green and W Zerna. *Theoretical elasticity, 1954*.

[79] H Medina and B Hinderliter. "Method for Generating and Realizing Replicates of Randomly Roughened Surfaces, Tested on Poly Methyl (Methacrylate)". In: *Experimental Techniques* (2013).

[80] Walter D Wilkinson, William F Murphy, and Warren J MacGonnagle. *Nuclear reactor metallurgy*. van Nostrand, 1958.

[81] William D Callister and David G Rethwisch. *Fundamentals of materials science and engineering*. Vol. 471660817. Wiley, 2013.

[82] Hector Medina and Brian Hinderliter. "Use of poly (methyl methacrylate) in the study of fracture of randomly damaged surfaces: I. Experimental approach". In: *Polymer* 53.20 (2012), pp. 4525–4532.

[83] Jozef Bicerano. *Prediction of polymer properties*. CRC Press, 2002.

[84] IRG Ogilvie et al. "Reduction of surface roughness for optical quality microfluidic devices in PMMA and COC". In: *Journal of Micromechanics and Microengineering* 20.6 (2010), p. 065016.

[85] Chen-Kuei Chung, YC Lin, and GR Huang. "Bulge formation and improvement of the polymer in CO2 laser micromachining". In: *Journal of Micromechanics and Microengineering* 15.10 (2005), p. 1878.

[86] IA Choudhury and S Shirley. "Laser cutting of polymeric materials: an experimental investigation". In: *Optics & Laser Technology* 42.3 (2010), pp. 503–508.

[87] Lawrence E Malvern. *Introduction to the Mechanics of a Continuous Medium*. Monograph. 1969.

[88] ASTM Standard. “D790,Standard Test Methods for Flexural Properties of Unreinforced and Reinforced Plastics and Electrical Insulating Materials”. In: *West Conshohocken (PA): ASTM International* (2010).

[89] ASTM Standard. “D790-07: Standard Test Method for Flexural Properties of Unreinforced and Reinforced Plastics and Electrical Insulation Materials”. In: *American Society for Testing and Materials*. 1997.

[90] ASTM Standard. “D790-86”. In: *Standard test methods for flexural properties of unreiniforced and reinforced plastics and electrical insulating materials. Philadelphia, PA: American Society for Testing and Materials* (1986).

[91] John E Connett. “Repeatability and Reproducibility”. In: *Wiley Encyclopedia of Clinical Trials* ().

[92] D. Kockott. “The shape of Surfaces”. In: *Handbook of Polymer Testing*. Ed. by D. Brown. New York: Marcel Dekker, 1999.

[93] George Wypych. *Handbook of material weathering*. Hyperion, 2003.

[94] K Hardcastle and N Searle. “Weathering Test Methods”. In: *Plastics and Coatings-Durability, Stabilisation, Testing, Rose A. Ryntz, Hanser, Munchen* (2001), p. 189.

[95] Mark E Nichols. “Anticipating paint cracking: the application of fracture mechanics to the study of paint weathering”. In: *Journal of Coatings Technology* 74.924 (2002), pp. 39–46.

[96] Richard Siderits et al. “Three-Dimensional Laser Scanning of” Crime Scene Gum” as a Forensic Method Demonstrating the Creation of Virtual Tooth Surface Contour and Web-Based Rapid Model Fabrication.” In: *Forensic Science Communications* (2011).

[97] Rama Krishna Alla et al. “Surface Roughness of Implants: A Review.” In: *Trends in Biomaterials & Artificial Organs* 25.3 (2011).

[98] Cc Larsson et al. “Bone response to surface modified titanium implants: studies on electropolished implants with different oxide thicknesses and morphology”. In: *Biomaterials* 15.13 (1994), pp. 1062–1074.

[99] Barbara D Boyan et al. “Role of material surfaces in regulating bone and cartilage cell response”. In: *Biomaterials* 17.2 (1996), pp. 137–146.

[100] I. Degasne et al. “Effects of roughness, fibronectin and vitronectin on attachment, spreading, and proliferation of human osteoblast-like cells (Saos-2) on titanium surfaces”. In: *Calcified tissue international* 64.6 (1999), pp. 499–507.

[101] Stuart Croll and Brian Hinderliter. “A framework for predicting the service lifetime of composite polymeric coatings”. In: *Journal of materials science* 43.20 (2008), pp. 6630–6641.

[102] Valeria Cannillo and W Craig Carter. “A stochastic model of damage accumulation in complex microstructures”. In: *Journal of materials science* 40.15 (2005), pp. 3993–4004.

[103] Brian Hinderliter and Stuart Croll. “Monte Carlo approach to estimating the photodegradation of polymer coatings”. In: *Journal of Coatings Technology and Research* 2.6 (2005), pp. 483–491.

[104] Carmen Castillo et al. “Stochastic Model for Damage Accumulation in Rubble-Mound Breakwaters Based on Compatibility Conditions and the Central Limit Theorem”. In: *Journal of Waterway, Port, Coastal, and Ocean Engineering* 138.6 (2012), pp. 451–463.

[105] Ken Mela and John N Louie. “Correlation length and fractal dimension interpretation from seismic data using variograms and power spectra”. In: *Geophysics* 66.5 (2001), pp. 1372–1378.

[106] Harald Bergstrom. *Limit theorems for convolutions*. Almqvist & Wiksell Stockholm, 1963.

[107] Martin F Jensen et al. “Microstructure fabrication with a CO2 laser system: characterization and fabrication of cavities produced by raster scanning of the laser beam”. In: *Lab on a Chip* 3.4 (2003), pp. 302–307.

[108] Yongguang Huang et al. “Surface roughness analysis and improvement of PMMA-based microfluidic chip chambers by CO¡ sub¿ 2¡/sub¿ laser cutting”. In: *Applied Surface Science* 256.6 (2010), pp. 1675–1678.

[109] Karl Pearson. “Mathematical Contributions to the Theory of Evolution.–On a Form of Spurious Correlation Which May Arise When Indices Are Used in the Measurement of Organs”. In: *Proceedings of the Royal Society of London* 60.359-367 (1896), pp. 489–498.

[110] American Society of Mechanical Engineers. *Surface Texture: (surface Roughness, Waviness, and Lay) : ANSI/ASME B46.1-1985 : an American National Standard*. American society of mechanical engineers, 1986.

[111] American Society of Mechanical Engineers. “ASME Y14.36M-1996(R2008): Surface Texture Symbols - Metric version”. In: (2008).

[112] International Organization for Standardization. Technical Committee ISO/TC 57. *ISO 4287. Geometrical Product Specifications (GPS). Surface Texture: Profile Method. Terms, Definitions and Surface Texture Parameters*. International Organization for Standardization, 1997.

[113] P Ranganath Nayak. “Random process model of rough surfaces”. In: *Journal of Lubrication Technology* 93.3 (1971), pp. 398–407.

[114] MA Grekov and SN Makarov. “Stress concentration near a slightly curved part of an elastic body surface”. In: *Mechanics of solids* 39.6 (2004), pp. 40–46.

[115] Stefan L Hahn. “Hilbert transforms”. In: *The transforms and applications handbook* (1996), pp. 463–629.

[116] HEJ Bennett and JO Porteus. “Relation between surface roughness and specular reflectance at normal incidence”. In: *JOSA* 51.2 (1961), pp. 123–129.

[117] Edward Charles Titchmarsh. *Introduction to the theory of Fourier integrals*. Clarendon Press Oxford, 1948.

[118] COMSOL Inc. “COMSOL multiphysics Version 3.5 a”. In: *COMSOL Inc, Burlington, MA* (2008).

[119] Frederick W King. *Hilbert transforms*. Vol. 2. Cambridge University Press Cambridge, UK, 2009.

VITA

Hector Eduardo Medina was born in Cocollar, a very small town in the south side of Sucre state, in the northeastern side of Venezuela. When Hector was in third grade he worked at the public market place carrying customer's shopping bags using a wheelbarrow in order to purchase shoes to attend school. Due to his high scholastic achievements he was awarded with the most prestigious fellowship that the Venezuelan Government can offer and was sent to attend the Colorado School of Mines. There, Hector obtained his Bachelors degree in Engineering, Magna Cum Laude, and with Outstanding International Award and Highest Scholastic Honors. Immediately before his graduation he was offered by the Head of the Department of Engineering to start a PhD in a joint program of CSM and NASA. Even though, he rejected the offered due to personal reasons, Hector always questioned his decision.

After returning to Venezuela, Hector worked for the oil industry as field engineer, in Aruba as a high school teacher and deputy director, and around the world as radio station studio installer. In 2011, he returned to the US to enroll graduate school and pursue his dream of teaching in higher education. He completed his M.S.at the Virginia Commonwealth University in May 2012 in Mechanical and Nuclear Engineering under the supervision of Dr. Brian Hinderliter. Along his doctoral work, Hector has been a full time single father of two beautiful girls: Nazareth (15) and Sarah (12). Hector is thankful of God to have received another opportunity. Hector's professional goals are to become a full time faculty, lead a research group and write.